

AD-A072 098

AERONAUTICAL RESEARCH INST OF SWEDEN STOCKHOLM
INVESTIGATION OF THE BOUNDARY CONDITION AT A WIND TUNNEL TEST S--ETC(U)

F/G 1/3

MAY 79 S NYBERG, S G HEDMAN, A RIZZI

AFOSR-77-3282

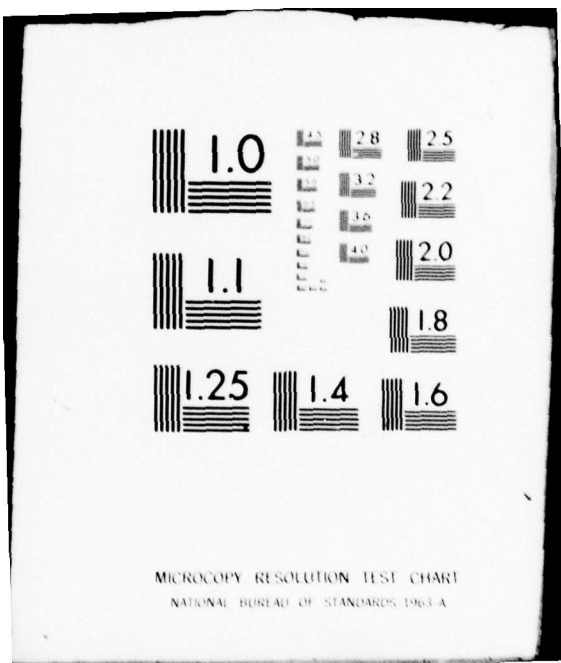
NL

UNCLASSIFIED

AFOSR-TR-79-0868

1 OF 2
AD
A072 098





ADA072098

(18) AFOSR TR-79-0868

(19) Grant No. AFOSR-77-3282 -

A052541

LEVEL

5

(6) INVESTIGATION OF THE BOUNDARY CONDITION AT A WIND TUNNEL TEST SECTION WALL FOR A LIFTING WING-BODY MODEL AT LOW SUPERSONIC SPEED.

(10) Sven-Erik Nyberg, Sven G. Hedman, Arthur Rizzi, Hans Sörensen

FFA, The Aeronautical Research Institute of Sweden
Stockholm, Sweden

(11) May 1979

(12) 97P.

D D C
PARAWID
JUL 31 1979
RECEIVED
C

(9) Final Scientific Report, 1 April 1977 — 31 March 1979

Approved for public release; distribution unlimited

(16) 23P7 (17) A1

Prepared for

AIR FORCE OFFICE OF SCIENTIFIC RESEARCH (AFSC)
Bolling AFB, USA

and

EUROPEAN OFFICE OF AEROSPACE RESEARCH (EOARD)
London, England

by

THE AERONAUTICAL RESEARCH INSTITUTE OF SWEDEN (FFA)
Stockholm, Sweden

FILE COPY

This research has been sponsored in part by the AFSC and,
to matched amount, by FFA

DDC

008550

B
79 07 27 082

UNCLASSIFIED

SECURITY CLASSIFICATION OF THIS PAGE (When Data Entered)

REPORT DOCUMENTATION PAGE		READ INSTRUCTIONS BEFORE COMPLETING FORM
1. REPORT NUMBER <i>(B)</i> AFOSR-TR-79-0868	2. GOVT ACCESSION NO.	3. RECIPIENT'S CATALOG NUMBER <i>(C)</i>
4. TITLE (and Subtitle) INVESTIGATION OF THE BOUNDARY CONDITION AT A WIND TUNNEL TEST SECTION WALL FOR A LIFTING WING-BODY MODEL AT LOW SUPERSONIC SPEED.		5. TYPE OF REPORT & PERIOD COVERED FINAL 1 April 1977 - 31 March 1979
7. AUTHOR(s) SVEN-ERIK NYBERG, HANS ISORENSEN SVEN G. HEDMAN ARTHUR RIZZI		6. PERFORMING ORG. REPORT NUMBER AFOSR 77-3282
9. PERFORMING ORGANIZATION NAME AND ADDRESS FFA, THE AERONAUTICAL RESEARCH INSTITUTE OF SWEDEN AERODYNAMICS DEPARTMENT PO BOX 11021, S-161 11 BROMMA, SWEDEN		10. PROGRAM ELEMENT, PROJECT, TASK AREA & WORK UNIT NUMBERS 2307A1 61102F
11. CONTROLLING OFFICE NAME AND ADDRESS AIR FORCE OFFICE OF SCIENTIFIC RESEARCH/NA BLDG 410 BOLLING AIR FORCE BASE, D C 20332		12. REPORT DATE May 1979
14. MONITORING AGENCY NAME & ADDRESS (if different from Controlling Office)		13. NUMBER OF PAGES 97
		15. SECURITY CLASS. (of this report) UNCLASSIFIED
		15a. DECLASSIFICATION/DOWNGRADING SCHEDULE
16. DISTRIBUTION STATEMENT (of this Report) Approved for public release; distribution unlimited.		
17. DISTRIBUTION STATEMENT (of the abstract entered in Block 20, if different from Report)		
18. SUPPLEMENTARY NOTES		
19. KEY WORDS (Continue on reverse side if necessary and identify by block number) TRANSONIC WIND TUNNELS WALL BOUNDARY CONDITION LOW SUPERSONIC SPEED		
20. ABSTRACT (Continue on reverse side if necessary and identify by block number) The purpose of the investigation is to study theoretically and experimentally at low supersonic speed the interference-free flow field around a lifting wing-body wind tunnel model at locations where the tunnel walls are normally situated. The undisturbed flow properties are used to establish criteria for cross flow characteristics of wave-attenuating ventilated wind tunnel walls. The flow field has been calculated theoretically by a relaxation method based on the transonic small perturbation (TSP) equation and for one sample case for the body alone with a method based on the solution of the full gas dynamic equations (the Euler		

~~UNCLASSIFIED~~

~~SECURITY CLASSIFICATION OF THIS PAGE(When Data Entered)~~

equations) in a time-dependent finite volume formulation. A survey of the flow has been made experimentally with a probe in wind tunnel tests. Pressure and flow deflection in the flow field near a delta-wing-body configuration have been calculated at free stream Mach number 1.2 and at angles of attack of 0° and 5°. The same properties have been determined in wind tunnel tests at Mach numbers 1.15, 1.20 and 1.30 and at nominal angles of attack 0°, 5°, 15° and 25°. The theoretical results obtained using the TSP method show only qualitative agreement with experimental data and the shocks are smeared out. Theoretical results obtained by the time-dependent finite volume method for the body alone show promising agreement with experiments. The experimental results show that for the wing-body model investigated within the Mach number and angle of attack range tested, the required relationship between pressure drop and cross flow for a minimum interference wind tunnel wall are quite different from the hitherto used criteria based on the requirements for a cone-cylinder at zero angle of attack.

~~UNCLASSIFIED~~

AIR FORCE OFFICE OF SCIENTIFIC RESEARCH (AFSC)
 NOTICE OF TRANSMITTAL TO DDC

LIST OF CONTENTS

This technical report has been reviewed and is
 approved for public release IAW AFR 190-12 (7b).
 Distribution is unlimited.

A. D. BLOSE

Technical Information Officer

	Page
SYMBOLS	5
1. INTRODUCTION	7
2. THEORETICAL INVESTIGATION	9
2.1 Calculation of the supersonic flow field around the wing-body model by means of a transonic small perturbation potential method	9
2.11 Theory	9
2.12 Application	11
2.2 Calculation of the supersonic flow field around the body at zero angle of attack by means of a method based on the Euler equations	11
3. EXPERIMENTAL INVESTIGATION	12
3.1 Test method and set-up	12
3.2 Model, balance and sting	13
3.3 Combined flow inclination and static/pitot pressure probe	13
3.4 Test program	14
3.5 Accuracy	16
4. RESULTS	17
4.1 Theoretical investigation	17
4.2 Experimental investigation	19
4.21 Longitudinal pressure and flow angle distribution	19
4.22 Relationship between pressure disturbance and flow angle	21
5. CONCLUSIONS	24
6. REFERENCES	26
FIGURES (Figures 1 - 35)	29
APPENDIX 1 (Figures 36 - 54)	61
APPENDIX 2 (Figures 55 - 73)	81

SYMBOLS

c	wing chord
c_p	pressure coefficient
f	function describing model surface
k	slope of pressure-differential ratio versus pitch angle curve $= \partial(\frac{p_{s1} - p_{s3}}{q})/\partial\theta \text{ and } \partial(\frac{p_{s4} - p_{s2}}{q})/\partial\theta$
M	Mach number
p_{si}	pressure measured at orifice i on the probe
q	dynamic pressure
r	radial distance model-probe axis (mm), (Figure 2)
U	velocity
x,y,z	Cartesian coordinates (mm), (Figures 1 and 2) x in flow direction y in spanwise direction z upwards
α	angle of attack
δ	wing thickness ratio
$\delta_{1-3}, \delta_{4-2}$	angle between the geometric probe centerline and the aerodynamic centerline projected in the vertical plane (1-3) and in the horizontal plane (4-2), (Figures 8 and 9)
δ_v	flow inclination in the tunnel vertical plane, positive when the flow direction is up, (Figure 8)
ϵ	scaling factor
ϕ	velocity potential or roll angle of the probe, (Figure 8)
ψ	perturbation velocity potential or meridian angle model-probe, (Figure 2)

θ

flow deflection angle, positive out from tunnel centerline at different wall positions or angle of pitch of the probe with respect to the tunnel centerline, positive, when probe nose is up, (Figure 8)

Subscripts

n denotes nominal value

∞ free stream condition

i probe hole number i = 1-6, (Figure 8)

Accession For	
NTIS GRA&I	<input checked="" type="checkbox"/>
DDC TAB	<input type="checkbox"/>
Unannounced	<input type="checkbox"/>
Justification _____	
By _____	
Distribution/ _____	
Availability Codes	
Dist	Avail and/or special
A	

1. INTRODUCTION

The model in a supersonic wind tunnel produces compression and expansion waves which are reflected at the test section wall. The type and the strength of the reflection depend on the wave attenuation properties of the wall. Below a certain Mach number, depending primarily on the model length in relation to its distance from the nearest test section wall, the reflected waves will hit the model and distort the pressure distribution over it.

There is today no method available to make reliable corrections for this kind of wall interference. The main research efforts over the last few decades have therefore been directed to minimizing the wall interference to such an extent that uncorrected data obtained in tunnels with wave-attenuating walls can be accepted.

Criteria for the desired cross flow characteristics of a wave-attenuating ventilated wall have been obtained by theoretical calculations of the undisturbed flow field at a distance from the model corresponding to the position of a hypothetical wall [1] and [2]^{*}. Accurate calculation of the flow field at low supersonic free stream Mach numbers has only been possible for two-dimensional wings and for zero-lift axisymmetric bodies.

The performed calculations have shown that the required relationship between pressure drop and cross flow for the wall varies within the flow field for the same model and also with model configuration and Mach number. Consequently it does not seem possible to find a fixed geometry wall that is interference-free. Some wall configurations have, however, been developed which offer an acceptable compromise among the various known design requirements.

The most successful configuration, currently in use in a number of operating wind tunnels, is the differential resistance perforated wall, developed at AEDC. The differential resistance to inflow and outflow is tailored to calculated and experimen-

* Numbers in brackets refer to entries in REFERENCES

tally verified requirements for cone-cylinder models and slender continuously curved axisymmetric models at zero angle of attack [1]. Later versions of this wall have variable porosity [3].

A cone-cylinder model is usually used to evaluate the wave-attenuating properties of the wall. These can be estimated by comparing the measured pressure distribution on the model with the theoretical one or with a pressure distribution obtained experimentally with a model that is so small in relation to the tunnel that the results can be considered as interference-free.

It could be said that the design criteria for the wall cross-flow characteristics and the methods to evaluate the wave-attenuating properties of the walls have resulted in test section wall configurations which are tailored to tests of axisymmetric bodies at zero angle of attack. Most wind tunnels are, however, mainly used for development testing of airplanes and missiles. Some calibration tests with models of different sizes in relation to the test section have shown that although the wall interference is far from negligible, the results can in most cases be considered as acceptable for routine testing [4].

Little is known however about the requirements on the wall cross-flow characteristics for a lifting aircraft configuration. It is the objective of this investigation to study experimentally and theoretically the undisturbed flow field around a lifting wing-body wind tunnel model at locations where the tunnel walls are normally situated. The results might be used to establish relevant wall boundary conditions for this type of model.

This investigation has been carried out as a two year program. The first year activities were reported in an Interim Scientific Report [5], which covered the theoretical computations and the preparations for the wind tunnel tests. Most of the material presented in [5] is included in this report, which covers all the activities of the two year program.

Principal investigator has been S.-E. Nyberg; S.G. Hedman has carried out the theoretical investigation with the TSP method, assisted by N. Agrell, who carried out part of the calculations; A. Rizzi carried out the calculations with the method based on the Euler equations; H. Sörensen has been responsible for the wind tunnel tests.

Papers on material from this investigation have been presented at the 50th Semi-annual Meeting of the Supersonic Tunnel Association, Sept. 1978 [6] and at "Sitzung des DGLR Fachausschusses 3.1", Feb. 1979 [7].

2. THEORETICAL INVESTIGATION

2.1 Calculation of the supersonic flow field around the wing-body model by means of a transonic small perturbation potential method

2.11 Theory

The transonic small perturbation (TSP) method is described in [8].

A perturbation potential ϕ is defined in terms of the full velocity potential ψ ,

$$\phi(x, y, z) = U_\infty [x + \epsilon \psi(x, y, z)]$$

where the scaling factor ϵ is chosen to be $\epsilon = \delta^{2/3}/M_\infty$ and δ is taken as the average wing thickness ratio. The transonic small perturbation equation written in ϕ is

$$[(1 - M_\infty^2) - (\gamma + 1) M_\infty^2 \epsilon \phi_x] \phi_{xx} + \phi_{yy} + \phi_{zz} = 0 .$$

This equation is put in finite difference form and solved by a relaxation procedure introduced by Murman and Cole [9]. Its mixed flow character is catered for through the use of centered

differences in subsonic portions and upstream differences in supersonic portions of the field.

The surface of the configuration may be written as $z = f(x, y)$. For field points adjacent to the body the boundary condition becomes

$$\varphi_z = \left(\frac{1}{\epsilon} + \varphi_x \right) f_x + \varphi_y f_y$$

and for wing boundary points

$$\varphi_z = \frac{1}{\epsilon} f_x .$$

The calculations of the flow field are made at points in a rectangular grid covering a finite domain of the physical space. The condition at the most upstream side of the box containing all the field points is $\varphi = 0$. No condition is forced on the most downstream side. At the remaining four exterior surfaces of the box the potential φ is put to zero. These surfaces are situated so far away from the model that effects from them should be negligible at the points investigated.

The pressure coefficient in the field is computed from

$$C_p = 2 \epsilon \varphi_x ,$$

and the flow angle from

$$\theta = \tan^{-1} [(\varphi_y + N\varphi_z) / (\frac{1}{\epsilon} + \varphi_x)]$$

where $N = \pm 1$ for $y = 0, z \gtrless 0$.

In the absence of a shock fitting procedure shocks are smeared out over several mesh widths in finite difference calculations. In particular this is so when shocks are swept [10]. The calculations therefore will not be able to give discontinuous changes in C_p and θ at the shock.

2.12 Application

The main portion of the calculations was performed in grid 1, described in the table below. To estimate the effect of the size of the box, control runs were made in the slightly wider grid 2. The model positioned in grid 1 can be seen in Figure 1.

Grid	Type of calculation	No. of points			Size in model scale		
		x	y	z	x	y	z
1	Main	37	40	27	-90/165	-294/294	0/286
2	Control	34	42	28	-63/142	-355/355	0/337

A relaxation factor of approximately one was used. The changes in the flow field settled down at first at the upstream end. Thus during most iterations, only the downstream portion was recalculated. 520 iterations were performed for the $\alpha = 0^\circ$ case. This solution was then used as a start for the 5° incidence case and 340 more iterations were made. Small changes in the field were still observed in the planes $x = 142$ and $x = 165$.

The effects of the change of grid system were so small that they could not be seen in the plotted results.

2.2 Calculation of the supersonic flow field around the body at zero angle of attack by means of a method based on the Euler equations

In view of the limitation of the potential flow solution to irrotational flow and to its treatment of differencing the potential function across shock waves, it seemed worthwhile to examine an alternative numerical procedure, namely, the solution of the full equations of gas dynamics (Euler equations) in a finite-volume formulation. This type of procedure in a wide variety of forms [11] was originally developed about 10 years ago for the calculation of flow fields about re-entry vehicles and missiles which travel at high supersonic Mach numbers. While in principle

the method is applicable to flow at low supersonic speeds, in practice a number of difficulties is known to arise and it is only recently that efforts have been made to overcome them [12, 13].

In Rizzi's approach the Euler equations are integrated by taking finite differences in a fully conservative form. The bow shock wave is searched for and found and the correct jump relations across it are then inserted into the flow field at that location. In this way finite differences of discontinuous variables are never encountered. Essential to this technique is the implementation of a computational mesh that can move and adjust to the flow field as it evolves during the course of the computation (in contrast to the relaxation method for which the mesh is fixed). While more sophisticated, this mesh-adjusting procedure can run into difficulties as the free stream Mach number approaches unity. Consider, for example, the case of flow past a cone-cylinder for which the bow wave is just detached from the tip. The distance between the body and the shock then varies, as one proceeds from the tip to the flank, by orders of magnitude, and an accurate computation will require a specially refined mesh network.

As a preliminary test of the suitability of this approach at low supersonic speed in the present context and as an illustration by concrete example of the difficulties inherent in it, flow with $M_\infty = 1.2$ and zero incidence past the body without wing was computed.

3. EXPERIMENTAL INVESTIGATION

3.1 Test method and set-up

The experimental investigation was carried out in the FFA TVM-500 wind tunnel, which is a blow-down tunnel with $0.5 \times 0.5 \text{ m}^2$ cross sectional area in the test section [14]. The tunnel has a single-jack flexible supersonic nozzle and a transonic test section with porous walls. The tests reported in this report have been performed in the supersonic nozzle, which allows the Mach number to be varied continuously.

The testing method was earlier successfully used in sonic boom research to determine the flow field around lifting SST configurations at $M = 2.7$ [15]. Figures 2 and 3 show the test set-up. By a special support mechanism the model can be translated in the x direction along the tunnel centerline during the test and it can also be rolled around the x axis. The position of the combined flow inclination and static/pitot pressure probe is fixed during a test run, but the radial position (y and z directions) can be changed between the runs.

3.2 Model, balance and sting

The model had to be small enough for the waves generated by the model after reflection at the real wind tunnel wall not to interfere with the measurements at the hypothetical wall (Figure 2). For measurements at $M_\infty = 1.2$ in wind tunnel TVM-500 a model span of 70 mm was chosen. The model is composed of an axisymmetric body and a delta wing typical for a supersonic fighter. The selected configuration is geometrically similar to a larger model, extensively tested at FFA earlier.

A two-view sketch of the model arrangement is shown in Figure 4. The wing has a leading edge sweep back angle of 40° . The aspect ratio is 3.2 and the taper ratio 0.2. The wing profile parallel to the plane of symmetry of the body is a modified NACA-64A004 airfoil section. The construction of the model required a thickened profile from $x/c = 0.5697$ to the trailing edge. The coordinates of the modified NACA profile are given in Figure 5. The body is a circular cylinder with a pointed ogive nose section.

The model is mounted on a two-component strain gauge balance and a sting. A photograph of the test set-up is shown in Figure 6.

3.3 Combined flow inclination and static/pitot pressure probe

The hemispherical probe employed to determine the flow condition is shown in Figure 7. The probe has a diameter of 3 mm. Four

static pressure orifices are located circumferentially 90° apart on the hemispherical surface for determination of the flow inclination and four on the cylindrical surface for determination of the free stream static pressure. A pitot pressure orifice is located at the probe nose. The static pressure orifice diameters are 0.5 mm and the pitot pressure orifice diameter is 0.9 mm.

The probe has been calibrated at Mach numbers of 1.11, 1.16, 1.21 and 1.30 for a Reynolds number of $35 - 40 \times 10^6$ per meter. At each Mach number the flow inclination probe was held at pitch angle settings of ± 9 , ± 7 , ± 5 , ± 2 and 0 degrees for roll angles of 0° , 90° , 180° , 270° and 300° . These runs provided the information necessary to calibrate the probe. In Figures 8 and 9 are presented probe calibration results which enable the determination of Mach number, total pressure and flow angles.

Due to the geometry of the probe the pitot pressure, the flow inclination pressures and the static pressure were measured at different axial stations in the wind tunnel. The procedure used in determining the pressure coefficient C_p and the flow direction θ from the measured probe pressures is as follows. A tentative Mach number is first calculated, assuming $\theta = 0$, for the x station where the static pressure orifices are situated. Then the Mach number is interpolated to the probe nose and the pressure coefficient and flow inclination angle are determined. Now, in order to correct the Mach number, the angles of pitch and roll must be calculated and from the probe calibration curves the correction factor is found. The second approximation to the Mach number can now be determined and the same calculations as above can be repeated giving new values of the pressure coefficient and flow inclination angle. For this investigation one iteration was found to be sufficient.

3.4 Test program

The test program included determination of local pressure coefficients and flow angle in the undisturbed flow field around

the wing-body model at locations, where the wind tunnel test section walls would typically be situated. The major part of the measurements was made at $M_n = 1.20$ and consisted of surveys along the centerlines of the top ($\varphi = 0$), side ($\varphi = 90^\circ$) and bottom ($\varphi = 180^\circ$) walls for three hypothetical wind tunnel sizes of 140 ($r_n = 70$), 200 ($r_n = 100$) and 300 ($r_n = 150$) mm. The blockage area ratios for the model corresponding to these "tunnel sizes" are 0.7%, 0.4% and 0.2% respectively. The model was tested at the nominal angles of attack $\alpha_n = 0, 5^\circ, 15^\circ$ and 25° . The actual angles of attack, corrected for deflection in sting and support as computed from the balance measurements, are presented in the table below.

α_n^0	α^0		
	$M_\infty = 1.15$	$M_\infty = 1.20$	$M_\infty = 1.30$
0	0	0	0
5	5.7	5.7	5.7
15	16.8	16.9	17.1
25	-	27.9	28.3

Schlieren photographs were taken of the flow field generated by the model and the probe.

Tests were also made at $M_n = 1.15$ and 1.30 for one "tunnel size" 200 ($r_n = 100$) mm. At $M_n = 1.15$ the highest angle of attack $\alpha_n = 25^\circ$ was omitted because at this angle the waves generated by the model after reflection at the real wind tunnel wall disturbed the measurements severely.

The wind tunnel was operated at 230 - 270 kPa stagnation pressures and 295 K stagnation temperature.

The probe was directly fixed to the supersonic nozzle of the wind tunnel. The distance between the nozzle and the model varied

slightly with Mach number, and consequently also the distance from the model to the probe. The corrected distances are presented in the following table.

r_n mm	r mm		
	$M_\infty = 1.15$	$M_\infty = 1.20$	$M_\infty = 1.30$
20	-	73.2	-
100	102.6	103.2	105.3
150	-	153.2	-

3.5 Accuracy

The absolute level of accuracy of the results is very difficult to establish, because of the combined effects of the many possible sources of error. Precautions were however taken to reduce the magnitude and probability of significant errors. The facility instrumentation consists primarily of high sensitivity pressure measurement devices for determining both stagnation and reference pressures. The instruments were calibrated carefully preceding the investigation. The free stream properties are considered accurate within the following limits

$$\begin{array}{ll} M_\infty & \pm 0.003 \\ P_\infty & \pm 0.4\% \end{array}$$

The precision with which local flow quantities can be determined is estimated to be as follows

Errors at $M_\infty = 1.2$

$$\begin{array}{ll} M & \pm 0.006 \\ P_{si} & \pm 0.2\% \\ C_p & \pm 0.02 \\ \theta & \pm 0.2^\circ \end{array}$$

The values of the errors in angles quoted here do not include the influence of the non-uniform flow on the probe. The inter-

action of the shock with the subsonic flow in front of the probe produces locally large errors. Therefore, the measurement is not accurate very close to shocks. In addition there is some influence due to Mach number gradients ($\Delta\theta \approx 0.1^\circ$).

4. RESULTS

4.1 Theoretical investigation

In the first phase of the investigation the flow field was calculated with the TSP method described in Section 2.1 for $\alpha = 0$ and 5° at $M_\infty = 1.20$ only. The intention was that, if the agreement was satisfactory between the theoretical calculations and the experimental results obtained later during the second phase, the calculations should be extended to lower Mach numbers, where the experiments are severely disturbed by wall interference. Pressure coefficient C_p and flow deflection angle θ as obtained by these calculations are presented as functions of the flow direction coordinate x in Figures 10 and 11. Calculations were made for radial distances from the model, $r = 73.2, 103.2$ and 153.2 mm and for meridian angles $\varphi = 0, 90^\circ$ and 180° corresponding respectively to the position of the top, side and bottom walls of three hypothetical wind tunnels of different size. Please note that the flow angle θ is defined positive for radial outflow from the model.

It can be seen

- that the calculated pressure and flow angle vary continuously through the shocks, because the shocks are smeared out in the calculation procedure.
- that effects due to lift decay faster than those due to thickness.

To assess the validity of the TSP calculations before experimental results were available for comparison, a numerical solution of the complete equations of gas dynamics was included for flow past the body without wing at $\alpha = 0$. The time-dependent finite volume method,

mentioned in Section 2.2 was used. In this method the shock wave is "fitted" so that the calculations yield a distinct point where the discontinuity lies. Comparison of the calculated results with the results obtained with the TSP method are shown in Figure 10. It can be seen that, while the location of the largest gradients in the TSP solution lies near the fitted shock wave, the amplitude of the change in C_p is much smaller.

The characteristics of a ventilated test section wall are frequently described by the relationship between the pressure drop of the flow when it passes through the wall and the flow angle of this flow at the wall [1, 2, 16]. It is therefore convenient to plot the undisturbed flow field data, obtained in this investigation, in the same manner in diagrams of the pressure disturbance C_p as a function of the flow angle θ . These diagrams can then be interpreted as the required characteristics for a hypothetical interference-free wall for the location and flow condition investigated.

Figures 12 and 13 present the calculated results for the wall positions investigated. The origin for each curve is positioned at the corresponding y and z coordinates in the (y,z) plane. These curves represent the required flow characteristics for an interference-free wall. As the characteristics vary throughout the flow field it does not seem possible to find a fixed geometry perforated wall configuration which is completely interference-free for this model.

Theoretical disturbance distributions for a cone-cylinder model with 2 per cent blockage [1] at the same Mach number $M_\infty = 1.2$ and zero angle of attack are shown for comparison in Figures 12 and 13. In the outflow region the flow characteristics for the wing-body model are similar to those for the cone-cylinder, but in the inflow region large differences occur. The results indicate that the need for differential-resistance characteristics for the wall is much less pronounced in the expansion region above this three-dimensional lifting wing than in the expansion region of the cone-cylinder.

Comparisons of the theoretical TSP results and the experimental results obtained in the second phase of this investigation are

shown in Figures 14-19 and 23-24. It is obvious that the TSP results for C_p as well as for θ show only qualitative agreement with the experimental data. The flow is "smeared out" in both compression and expansion areas and the peak values of C_p and θ are strongly underestimated. It was therefore considered appropriate not to extend the calculations to lower free stream Mach number until the TSP method has been further developed to handle them more accurately.

The results obtained with the method based on the Euler equations for the body alone case at $\alpha = 0$ are compared with experiments in Figure 15. The calculated shape of the bow shock is blunter than the measured. The pressure rise is well determined. A future extension of the calculations to include angle of attack for the body and later the complete wing-body configuration could be very useful for investigation of flow fields at low Mach numbers and for high angles of attack, where the experiments are highly disturbed by wall interference.

4.2 Experimental investigation

4.21 Longitudinal pressure and flow angle distribution

Examples of the experimentally determined flow field parameters are depicted in Figures 14-19. Shown are the C_p and θ distributions in the x direction at $M_\infty = 1.20$ over, under and at the side of the model at radial distance in these examples of $r = 73.2, 103.2$ and 153.2 mm from the model center. For comparison purposes the theoretical results calculated with the TSP method and in the $\alpha = 0$ case (Figure 15) the solution based on the Euler equations for the body alone are shown. Schlieren pictures in the same linear scale as the diagrams are incorporated in each figure to facilitate interpretation of the flow field parameters.

A complete set of diagrams of this kind, covering all tests performed, is to be found in Appendix 1 (Figures 36-54). At some test conditions with high angle of attack, large distance model-

probe and/or low free stream Mach number it can be seen from the Schlieren picture, that waves generated by the model are reflected at the real wind tunnel wall, see for instance Figure 49. Data points obtained downstream of the reflected bow wave are disturbed by wall interference and are in the diagrams marked with filled symbols.

Repeatability checks were made for some of the test conditions. The results, depicted in Figure 20, show satisfactory agreement among the different runs.

The longitudinal distance between two consecutive data points is determined by the stroke of the model, the number of recordings for each averaged data point, the multiplexing frequency of the data recording system, the number of pressures recorded and the available testing time for each run. The standard tests were made with 150 mm stroke, 20 recordings for each data point, 10.000 kHz multiplexing frequency, which resulted in 6.8 mm longitudinal distance between the data points. This gives in some cases too few data points for accurate determination of the shock locations. This is however, with the purpose of this investigation in mind, not very important as long as the magnitude of the maximum pressure and flow angle disturbance are reproduced with reasonable accuracy. This was checked in some tests with reduced stroke, giving high point density at the shocks. The results are shown in Figure 21 in comparison with the result from a standard test and the agreement is considered to be acceptable. It should however be noted that, with the high point density, as can clearly be seen, the curves have a finite slope at the bow wave, which is not correct. This is, as discussed in Section 3.5, due to probe-shock interference. In Appendix 1, where the data points are few at shocks, the shock-position has in some cases been marked with hatched lines in accordance with the shock position indicated by the Schlieren picture.

4.22 Relationship between pressure disturbance and flow angle

To establish the flow characteristics for an interference-free wall it is, as outlined in Section 4.1, convenient to plot the pressure disturbance C_p as function of the flow angle θ . An example of this type of disturbance distribution is depicted in Figure 22. It can be seen that the measured points form different curves in different parts of the flow field. The disturbance distribution ($C_p - \theta$ relationship) is for some cases split into two or three diagrams to facilitate interpretation of the results. The ends of each curve in these diagrams are marked with a letter, which is also shown at the corresponding point in the flow field diagram, included in the same figure.

A complete set of figures of this kind, covering all tests performed, is included in Appendix 2 (Figures 55-73). As outlined in Section 4.21 the measurements are for some test conditions partly disturbed by wall interference from the real test section wall. Data points, which are believed to be disturbed by wall or model support interference, are marked with filled symbols in the flow field diagrams and are excluded from the disturbance distributions. Consequently, and this must be emphasized, the disturbance distributions are incomplete for some test conditions, mainly combinations of low Mach number, high angle of attack and large values of the distance model-probe. The extent to which results are excluded from the disturbance distributions is in detail demonstrated in the figures of Appendix 2.

Figures 23-33 present the experimental disturbance distributions obtained for each combination of Mach number and angle of attack investigated. The origins for the disturbance distributions are positioned at the corresponding y and z coordinates in the (y, z) plane. Only test results which are considered unaffected by interference from the real wind tunnel wall are included. Please note that the C_p and θ scales are enlarged for the low angle of attack cases.

The theoretical results for the wing-body configuration mentioned in Section 4.1 and the theoretical results for a 10° half-angle

cone-cylinder with 2 per cent blockage at $\alpha = 0$ according to Goethert [1] are included for comparison in Figures 23 and 24. The comparison between theory and experiment is discussed in Section 4.1. Comparison with the cone-cylinder curves shows that the disturbance from the body nose for the wing-body model even at a distance $r = 103.2$ mm (corresponding to 0.4% blockage) is of similar magnitude to the disturbance from the cone of the cone-cylinder model (2% blockage) and also that the wing, even at 5.7° angle of attack, gives disturbances of similar magnitude to the expansion at the cone-cylinder junction. However the slope of the wing-body curves differs substantially from the slope of the cone-cylinder curves. The slope is higher in the outflow region and lower in the inflow region. Below the model ($\varphi = 180^\circ$) the curve is almost linear, while above and at the side of it ($\varphi = 0$ and 90°) it is curved upwards. This means that for this case ($\alpha = 0$ and 5.7° ; $M_\infty = 1.2$) a minimum interference wind tunnel wall should have linear flow characteristics or possibly differential resistance flow characteristics of a character different from what is required for a cone-cylinder.

All the experimental disturbance distributions shown in Figures 23-33 are summarized in Figures 34 and 35.

The influences of angle of attack and of distance from the model at a constant free stream Mach number of $M_\infty = 1.20$ are shown in Figure 34. It can be seen

- that the disturbance due to lift decays faster than the disturbance due to volume.
- that in some regions of the flow field outflow is required (θ positive) when the pressure is lower than the free-stream pressure (C_p negative) and vice versa. This displacement of the curves from the origin increases with increasing angle of attack, which probably is mainly due to flow curvature effects.

As pointed out by Goethert [1] perforated walls cannot produce characteristics to match the requirements for this

type of flow, but theoretically combined slotted-perforated test section configurations could be devised, to eliminate this basic difficulty. A convertible test section configuration providing open or perforated slots alternatively was suggested by Nyberg [17]. A pilot test section having perforated slots with variable porosity in accordance with this concept is now being investigated at FFA and could be a useful tool for further studies of these effects.

- that the $C_p - \theta$ relationship is linear or curved depending on position with respect to the model, with larger slope in the outflow region than in the inflow region. This curvature increases with angle of attack and is, as was mentioned in the discussion of the results for $\alpha_n = 0$ and 5° , opposite to the direction of the curvature of the characteristics required for the differential-resistance wall, which are based on cone-cylinder flow [1].

In view of these observations it is surprising that walls of this kind have shown acceptable wave attenuating properties for testing of wing-body combinations [4]. Recent measurements by Jacocks [16] have shown, however, that a fixed porosity wall of the so-called differential resistance type (60° slanted holes) does not have the supposed differential resistance character but has approximately linear characteristics instead. It was also found that a variable porosity wall of the same type but with the cut-off plate displaced upstream yielded non-linear characteristics with the largest slope in the outflow region, similar to the disturbance distribution for the wing-body model depicted in Figure 34. This is an important result, which deviates extensively from the earlier measurements [1] and which completely changes the picture of how the perforated wall with slanted holes behaves. The primary reason for the deviation is probably that Jacocks made careful Laser Doppler Velocity measurements directly of the flow inclination in the proximity of the ventilated wall while the earlier results were obtained by mass flux

measurements, assuming that the mass flux through the wall divided by the free stream mass flux is equivalent to the flow inclination remote from the wall. This assumption is reasonably valid for flow from the test section to the plenum (outflow) but breaks down totally for inflow [16]. Furthermore careful attention has to be paid to the influence of the wall boundary layer.

The influences of Mach number and angle of attack at a constant distance from the model $r_n = 100$ mm are shown in Figure 35. It is noted

- that the slope of the curve decreases with increasing Mach number
- that the experimental data are limited by interference from the real wind tunnel wall at low Mach numbers and high angles of attack. This emphasizes the need for reliable calculations at these flight conditions. Tests with the model in larger wind tunnels could give further valuable results, but difficulties with wall or probe interference will still occur when the Mach number approaches unity.

5. CONCLUSIONS

A theoretical and experimental investigation at low supersonic speed of the interference-free flow field around a lifting wing-body configuration at locations where the tunnel walls would be situated in a wind tunnel test has provided the following conclusions.

- Flow field data calculated by means of a transonic small perturbation potential method show only qualitative agreement with experimental data. Shocks are smeared out.

- Flow field data for the non-lifting body alone calculated by means of a method based on the Euler equations show promising agreement with experiments. A future extension of this work aiming at the calculation of the flow field around the lifting wing-body configuration should be of great importance particularly at low Mach numbers and high angles of attack, where the wind tunnel tests are hampered by wall and probe interference.
- The experimental method used seems to give flow field data with satisfactory accuracy provided that the local flow is supersonic and not disturbed by wall interference.
- The experimental flow field data show that the relationship between pressure disturbance and flow inclination varies throughout the flow field and is also affected by angle of attack and free stream Mach number. This relationship, which can also be interpreted as the required flow characteristics for an interference-free test section wall, may be linear or curved, with the largest slope in the outflow region. This is in contrast to the cone-cylinder flow field hitherto used as requirement for tunnel wall characteristics, where the largest slope is in the inflow region.
- In some areas of the flow field outflow is combined with underpressure and inflow with overpressure. Perforated walls cannot match the requirements for this type of flow, and it is therefore suggested that combined slotted-perforated walls, which theoretically are more suitable to eliminate this difficulty, should be investigated.

6. REFERENCES

1. Goethert, B.H. Physical aspects of three-dimensional wave reflections in transonic wind tunnels at Mach Number 1.20 (perforated, slotted, and combined slotted-perforated walls). AEDC-TR-55-45, March 1956
2. Goethert, B.H. Transonic wind tunnel testing. Edited by W.C. Nelson Published for and on behalf of AGARD by Pergamon Press, 1961
3. Jacocks, J.L. Comparison ov variable porosity wall transonic wind tunnel performance for upstream and downstream movement of the cutoff plates. ARO-AEDC-paper presented at the thirty-first Semiannual Meeting of the Supersonic Tunnel Association, April 24-25, 1969
4. Binion, Jr., T.W. An investigation of three-dimensional wall interference in a variable porosity transonic wind tunnel. AEDC-TR-74-76, Oct. 1974
5. Hedman, S.G.
Sörensen, H.
Nyberg, S.-E. Investigation of the boundary condition at a wind tunnel test section wall for a lifting wing-body model at low supersonic speed. Phase 1. Test preparations, revision of computer program and exploratory computations. Grant No. AFOSR-77-3282, Interim Scientific Report, 77 April 01 - 77 December 31, Feb. 1978
6. Hedman, S.
Nyberg, S.-E.
Sörensen, H. Methods used for investigation of the boundary condition at a wind tunnel test section wall for a lifting wing-body model at low supersonic speed and some preliminary results. Proc. of the 50th Semiannual Meeting of the Supersonic Tunnel Association, 20-22 Sept., 1978, Urbana, Illinois
7. Hedman, S.
Nyberg, S.-E.
Sörensen, H. Investigation of the boundary condition at a wind tunnel test section wall for a lifting wing-body model at low supersonic speed. FFAP-A-440, Material presented at Sitzung des DGLR Fachausschusses 3.1 "Hydro-, Aero- und Gasdynamik", DFVLR-AVA Göttingen, 6./7. Febr. 1979

8. Schmidt, W.
Hedman, S.G.
Recent explorations in relaxation methods for three-dimensional transonic potential flow.
ICAS-Paper 76-22, 1976
9. Murman, E.M.
Cole, J.D.
Calculation of plane steady transonic flows.
AIAA Journal, Vol. 9, No. 1, 1971
10. Murman, E.M.
Analysis of embedded shock waves calculated by relaxation methods.
AIAA Journal, Vol. 12, No. 5, 1974
11. Rusanov, V.V.
A blunt body in a supersonic stream.
In Annual Review of Fluid Mechanics, Vol. 8, eds. van Dyke, M. et al., Annual Reviews, Palo Alto, 1976
12. Rizzi, A.W.
Mesh-related problems in the calculation of supersonic flow near Mach number one.
Proc. Conf. on Num. Methods in Applied Fluid Dynamics, ed. B. Hunt, Academic Press, 1979
13. Rizzi, A.W.
Shock waves around bodies travelling at slightly-greater-than-sonic speed.
Theoretical and Experimental Fluid Mechanics, eds. U. Müller, K.G. Roesner and B. Schmidt, Springer-Verlag, 1979
14.
FFA Wind Tunnel Facilities
FFA Memorandum 93, Stockholm 1974
15. Landahl, M.
Sörensen, H.
Hilding, L.
Research on the sonic boom problem.
Part 2. - Flow field measurement in wind tunnel and calculation of second order F-function.
NASA CR-2340, Nov. 1973
16. Jacocks, J.
An investigation of the aerodynamic characteristics of ventilated test section walls for transonic wind tunnels.
The University of Tennessee,
Ph.D.-Thesis, 1976
17. Nyberg, S.-E.
A conceptual study of a convertible slotted transonic wall configuration.
Paper presented at the 46th Semiannual Meeting of the Supersonic Tunnel Association at Battelle Columbus Laboratories, Columbus, Ohio, 30 Sept - 1 Oct 1976

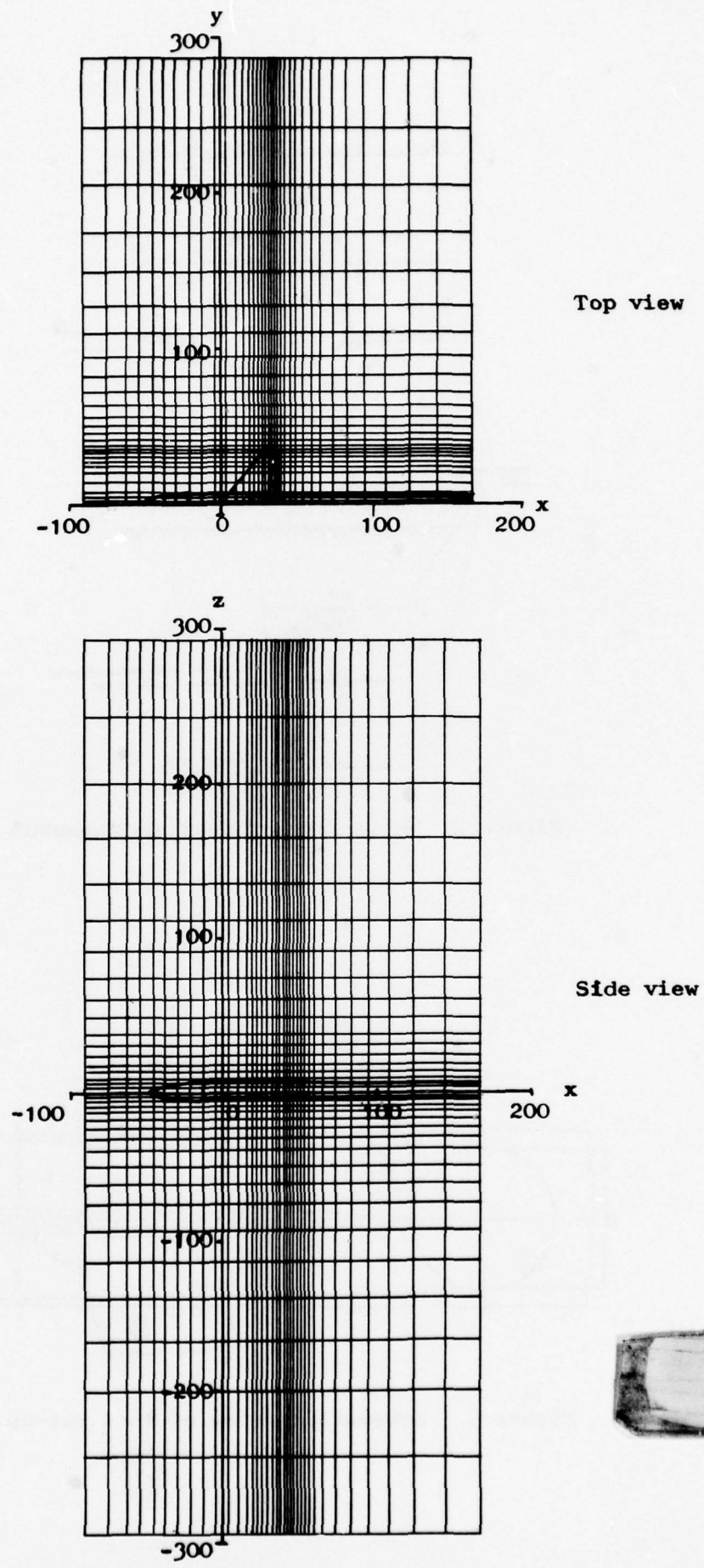


Figure 1. Model in computation grid.

PRECEDING PAGE BLANK

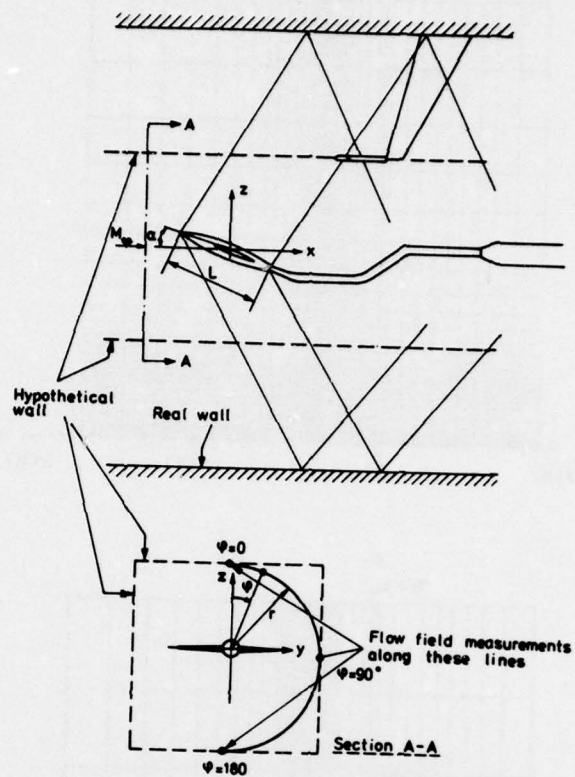


Figure 2. Principle of test arrangement.

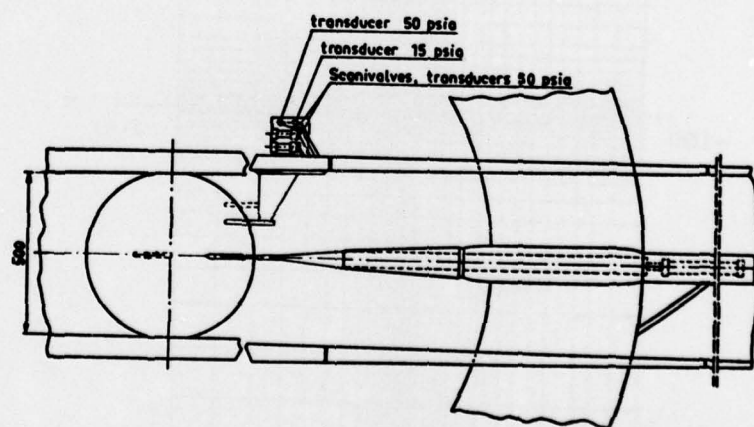


Figure 3. Schematic view of test set-up.

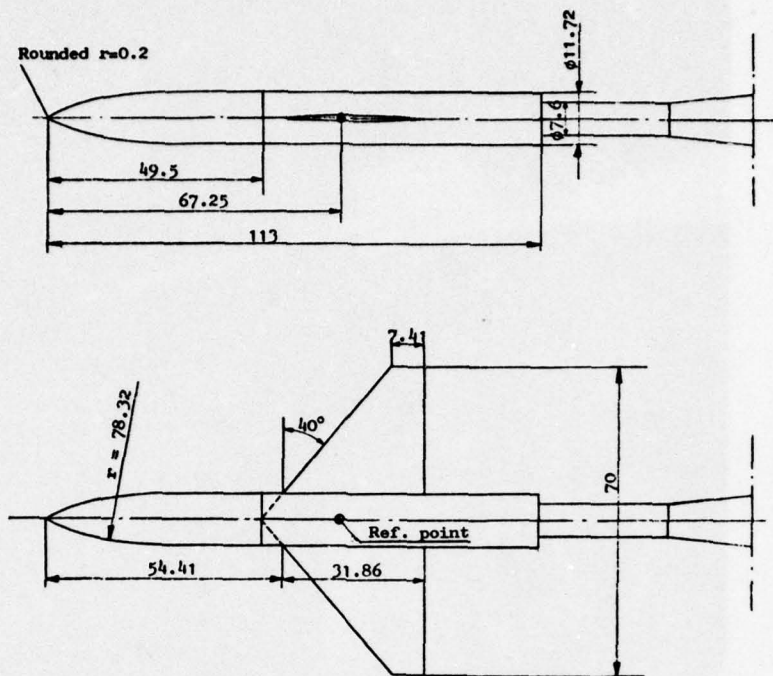
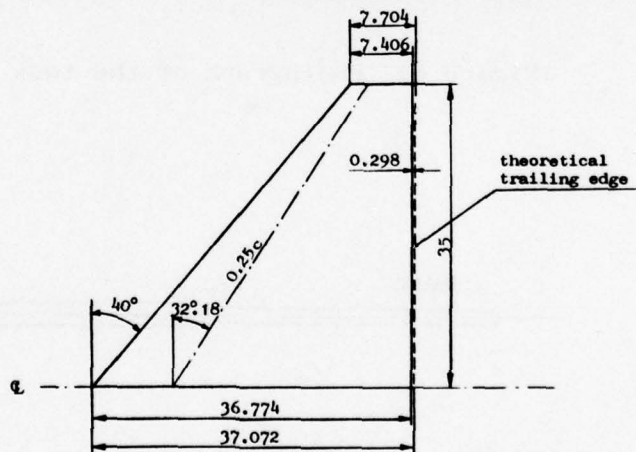


Figure 4. Wing-body model.



Aerofoil Section = Modified NACA 64A004

x/c %	z/c %	x/c %	z/c %	x/c %	z/c %
0	0	20	1.706	60	1.641
0.5	0.318	25	1.839	65	1.504
0.75	0.388	30	1.931	70	1.367
1.25	0.492	35	1.985	75	1.229
2.5	0.679	40	2.000	80	1.092
5	0.937	45	1.967	85	0.955
7.5	1.129	50	1.890	90	0.817
10	1.286	55	1.778	95	0.680
15	1.526	56.969	1.725	100	0.543

Figure 5. Wing data.

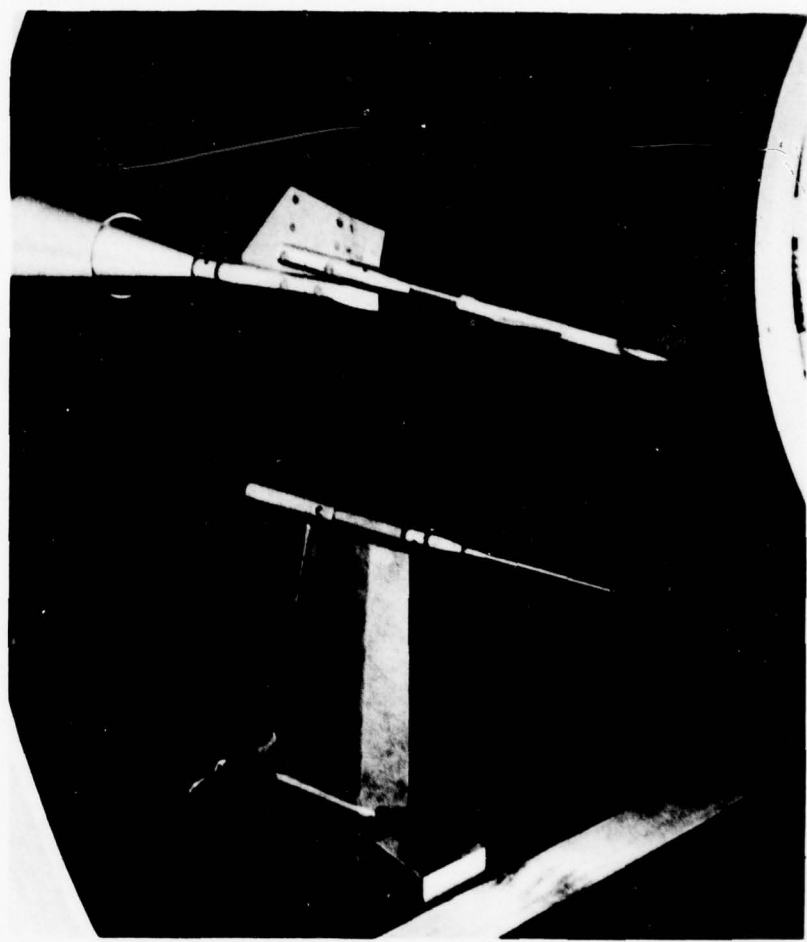


Figure 6. Photograph of the test set-up.

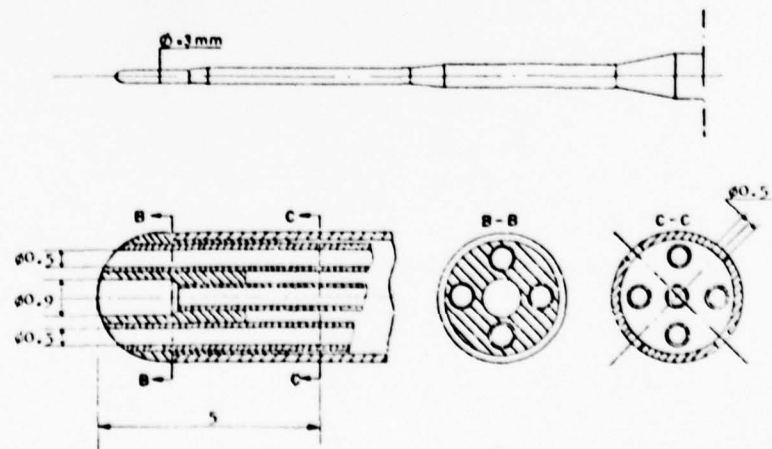
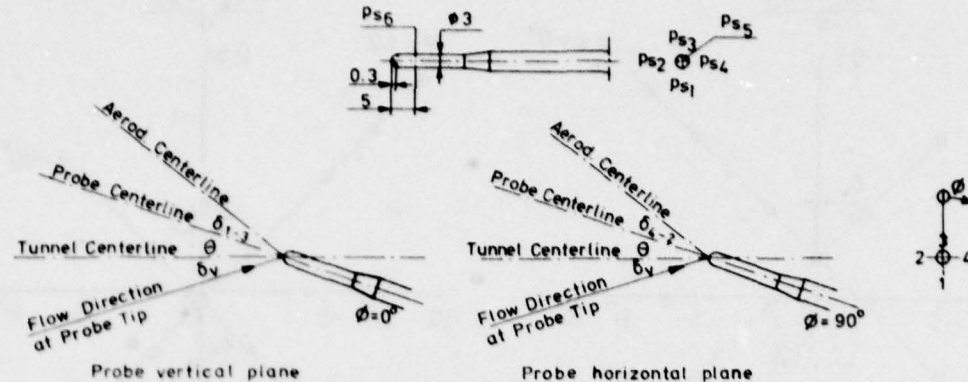
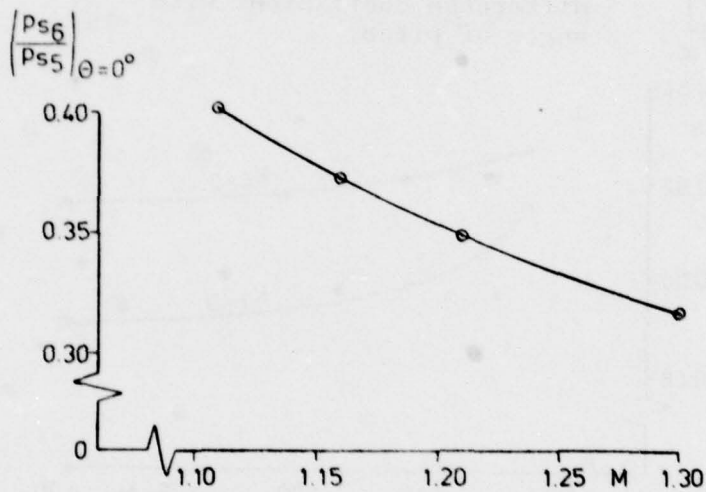


Figure 7. Combined flow inclination and static/pitot pressure probe.



Flow inclination geometry.



Variation of static-pitot pressure ratio with Mach number at zero angle of pitch.

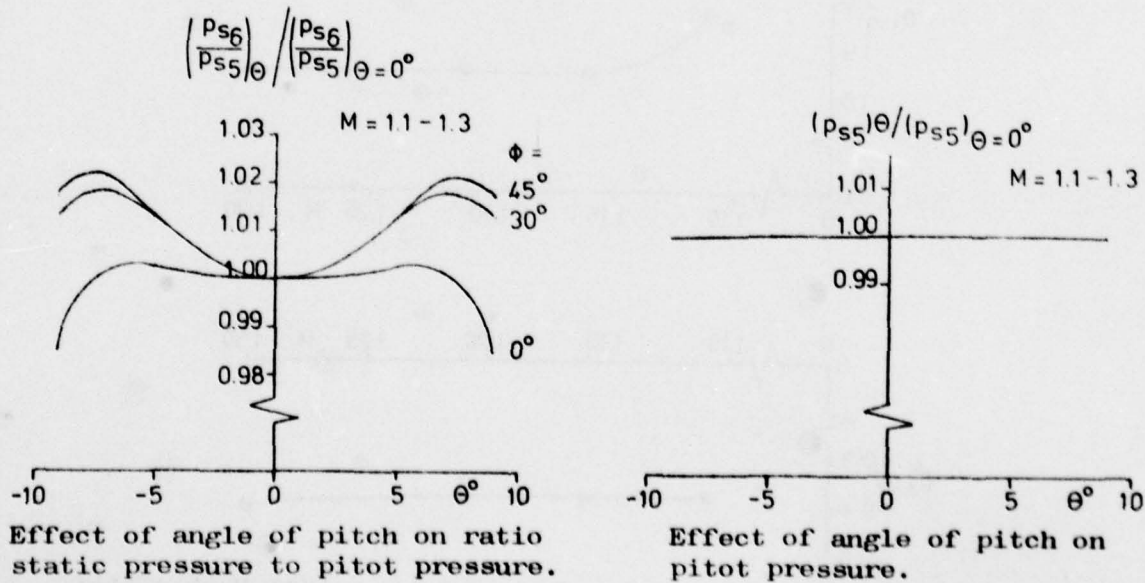


Figure 8. Examples of probe calibration results.

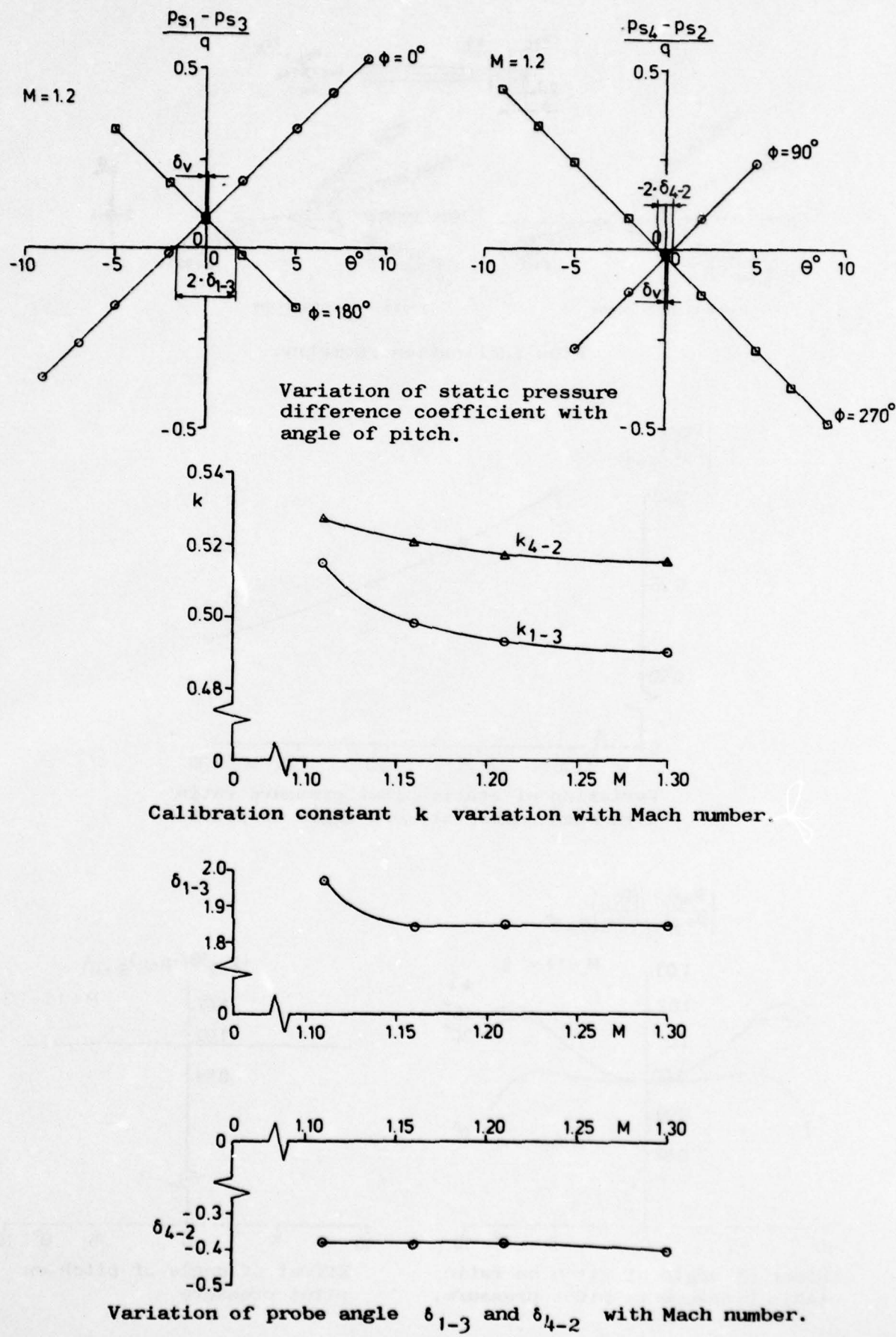


Figure 9. Examples of probe calibration results.

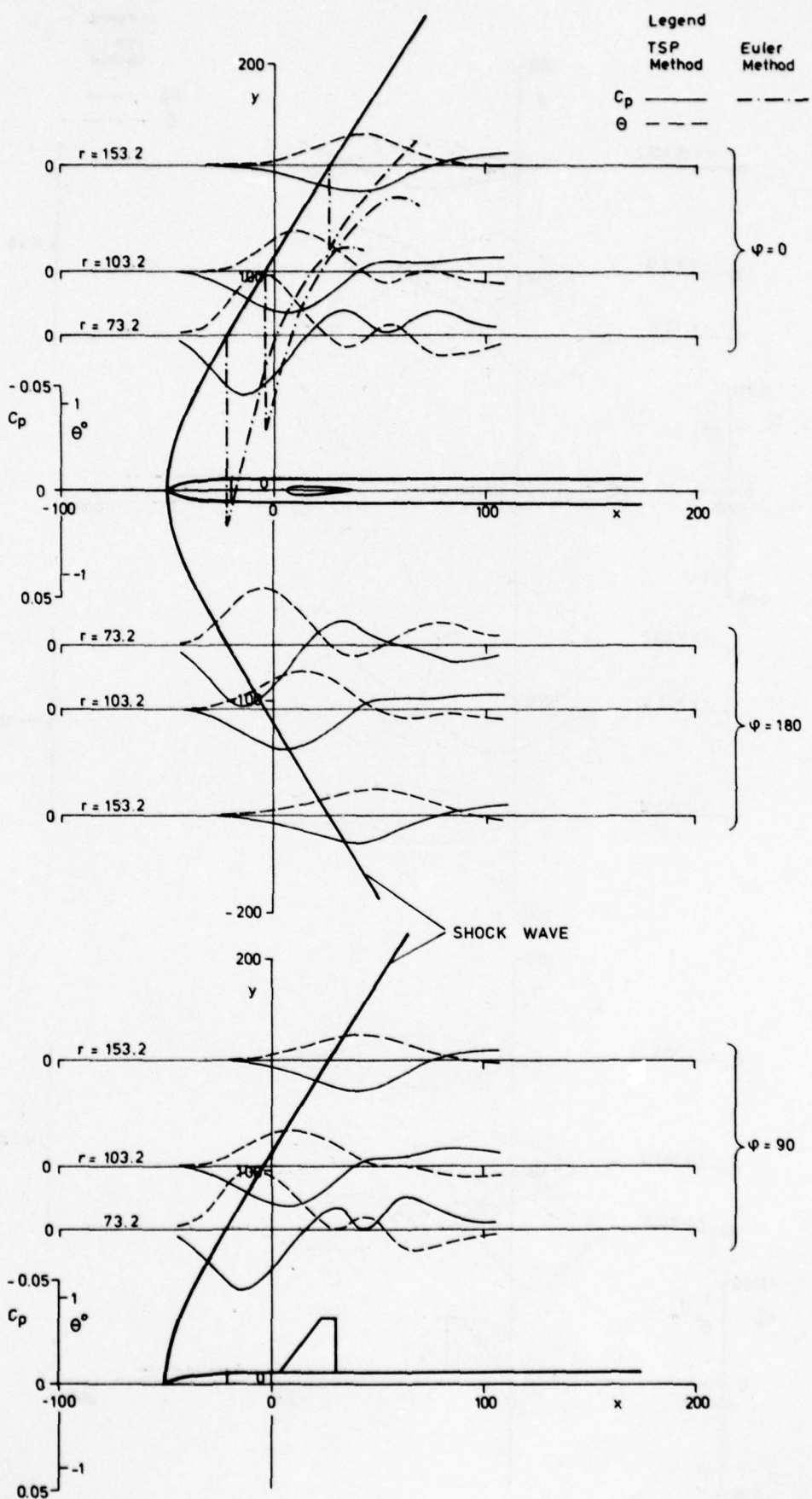


Figure 10. Theoretical flow field characteristics of the wing-body configuration at $M_{\infty} = 1.2$; $\alpha = 0^\circ$.

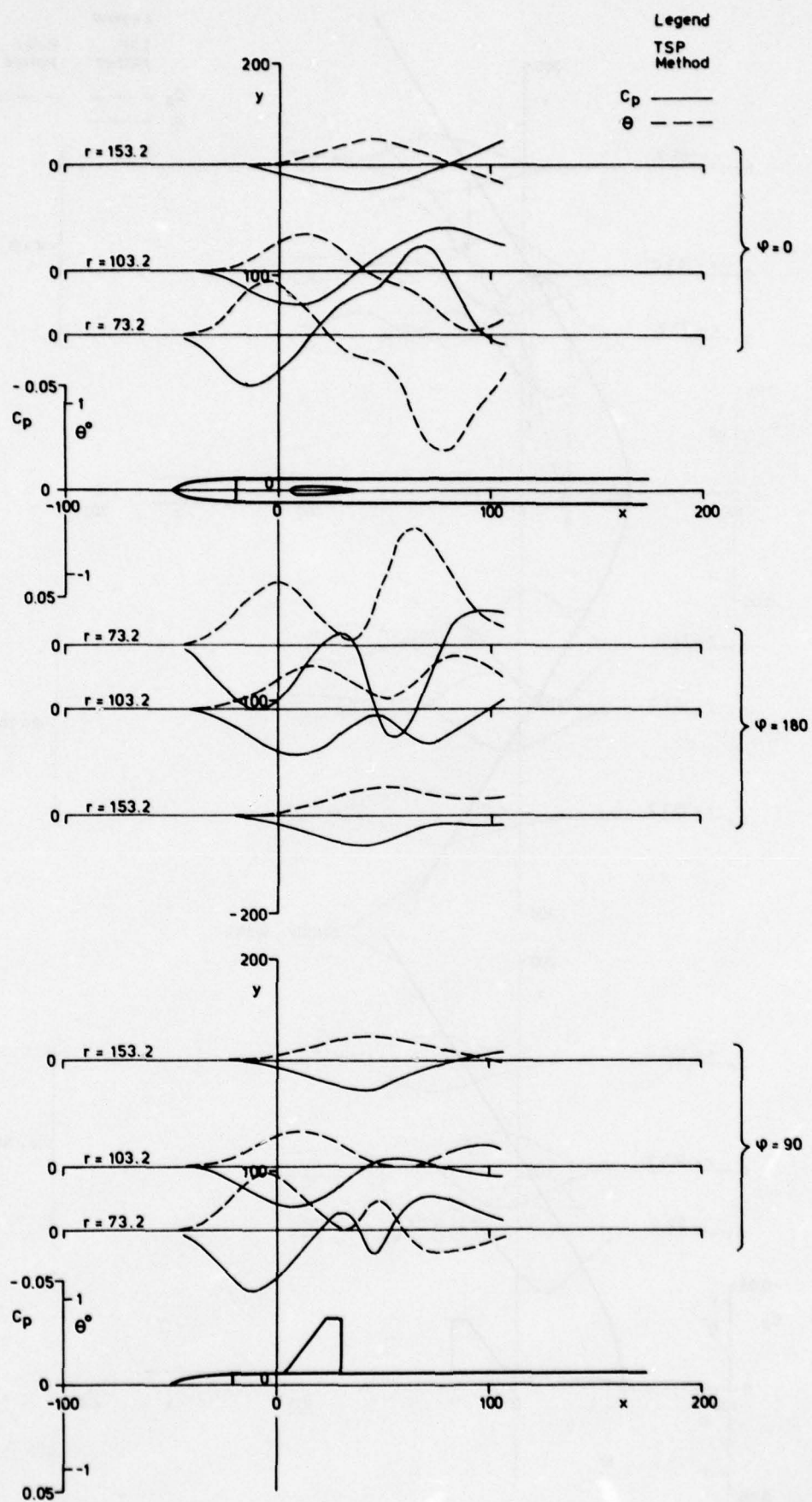


Figure 11. Theoretical flow field characteristics of the wing-body configuration at $M_{\infty} = 1.2$; $\alpha = 5.7^\circ$.

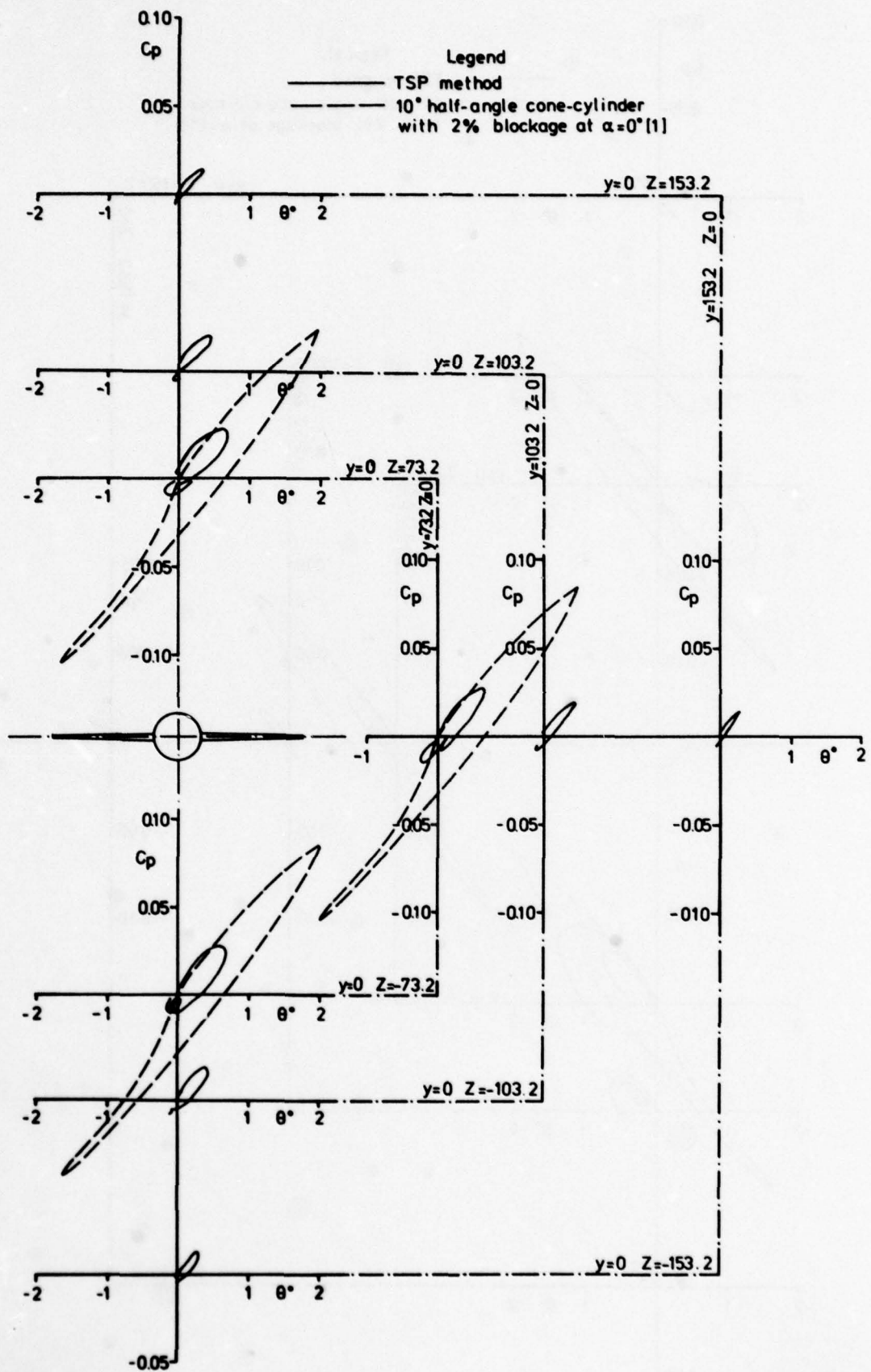


Figure 12. Calculated disturbance distribution of the wing-body configuration at $M_\infty = 1.2$ and $\alpha = 0^\circ$

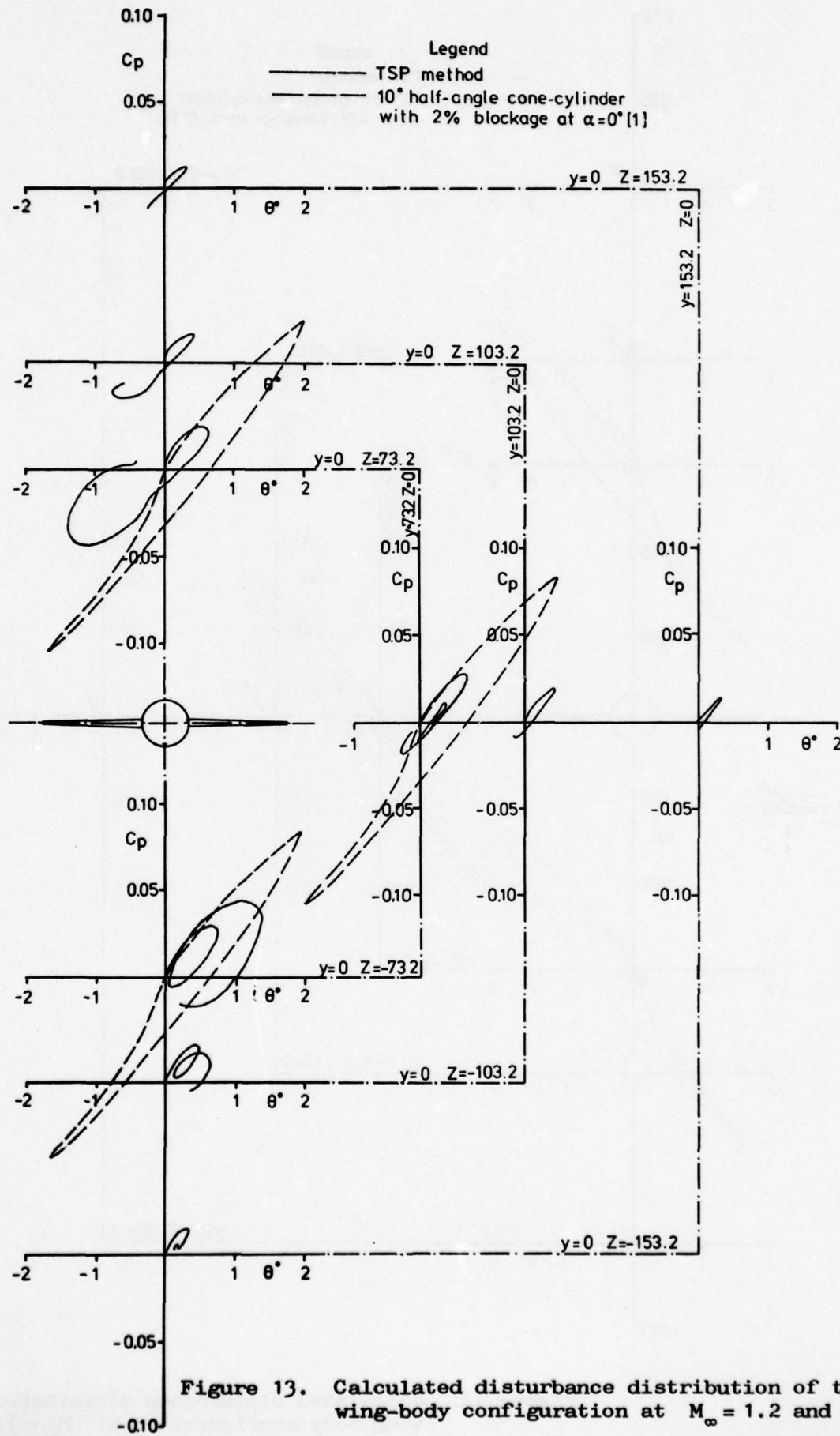


Figure 13. Calculated disturbance distribution of the wing-body configuration at $M_\infty = 1.2$ and $\alpha = 5.7^\circ$.

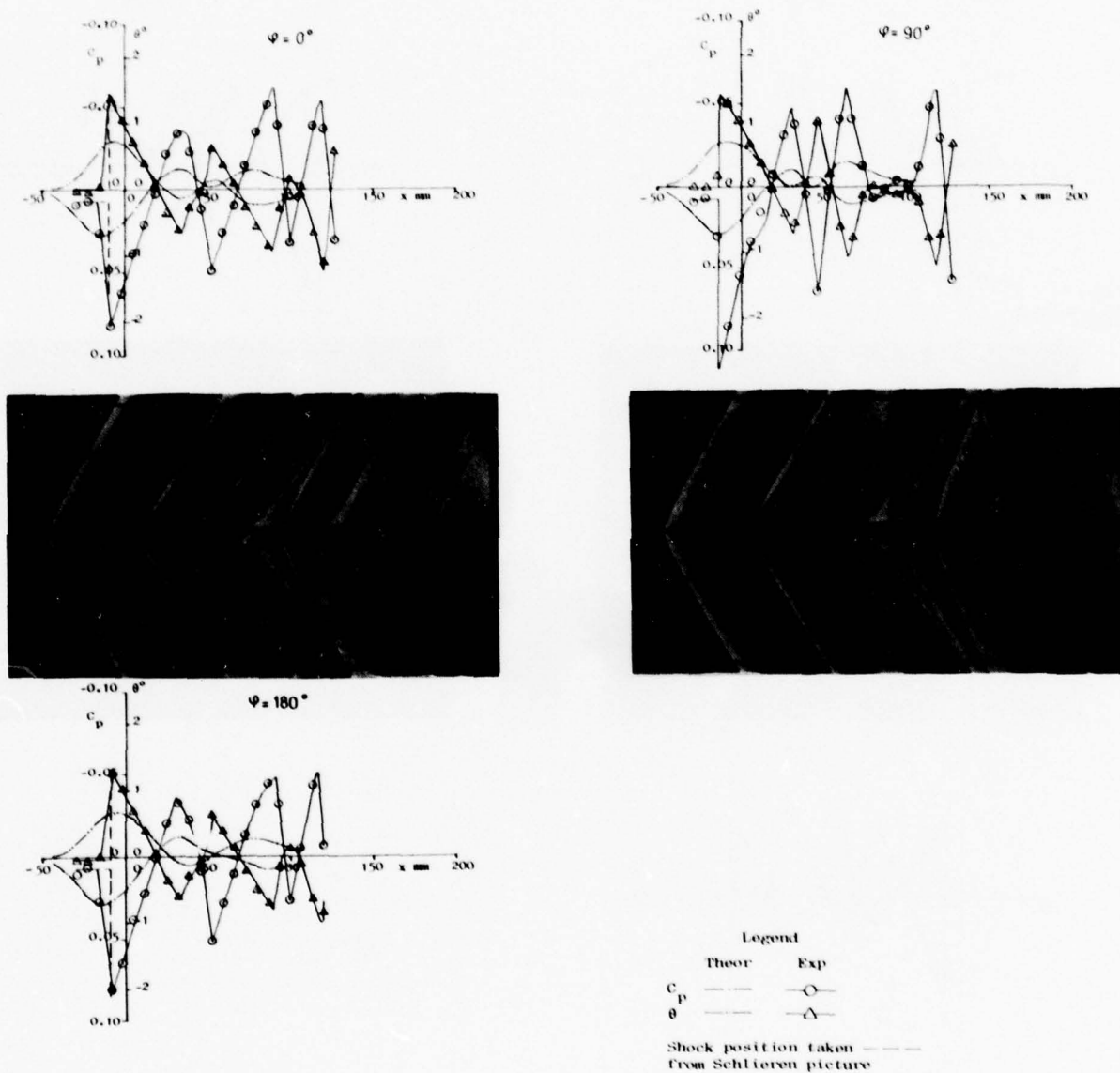


Figure 14. Theoretical and experimental flow field.

$M_\infty \approx 1.20$, $\alpha = 0^\circ$, $r = 73.2$ mm and $\varphi = 0^\circ, 90^\circ, 180^\circ$

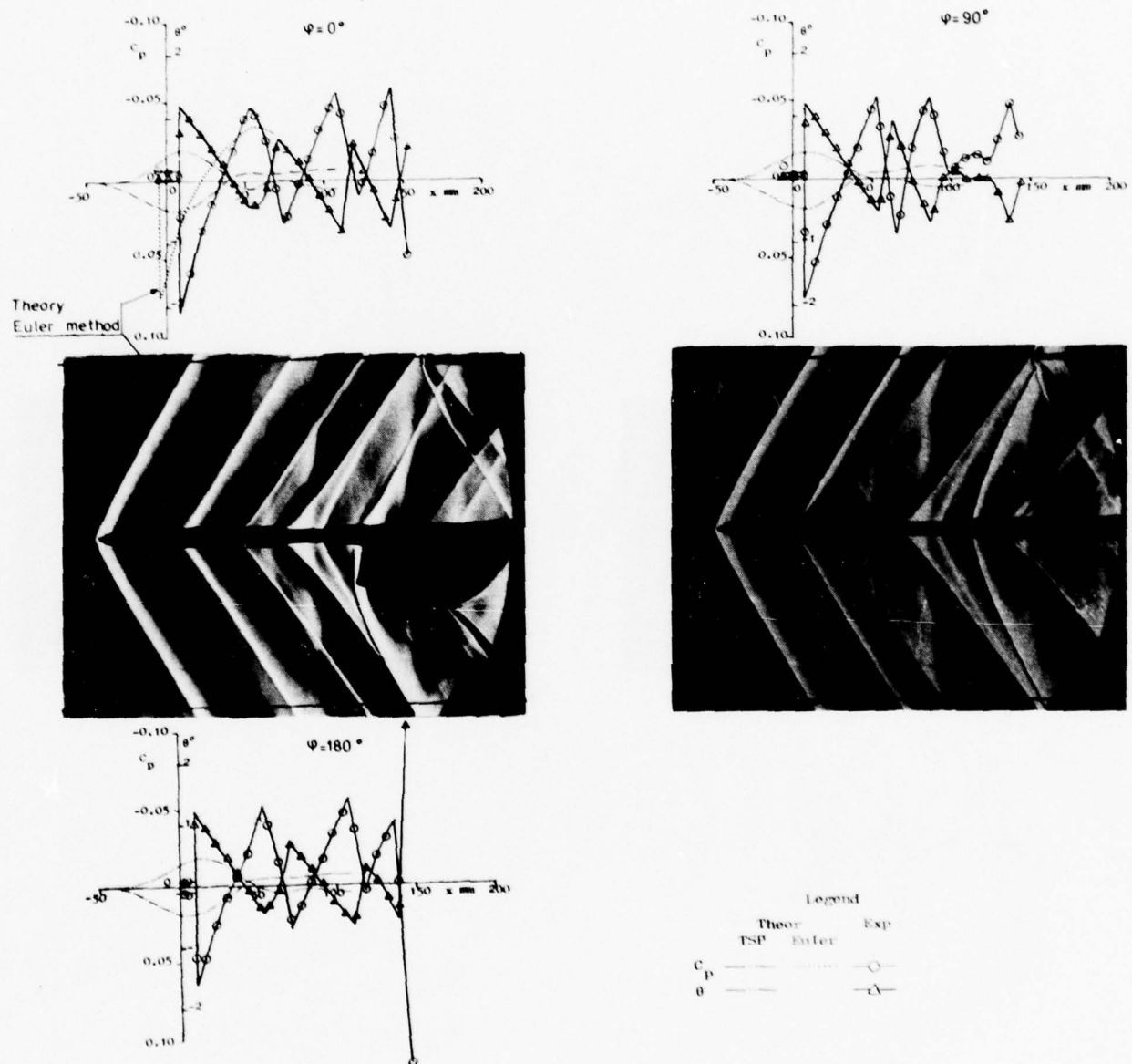


Figure 15. Theoretical and experimental flow field.

$M_\infty = 1.20$, $\alpha = 0^\circ$, $r = 103.2$ mm and $\varphi = 0^\circ, 90^\circ, 180^\circ$

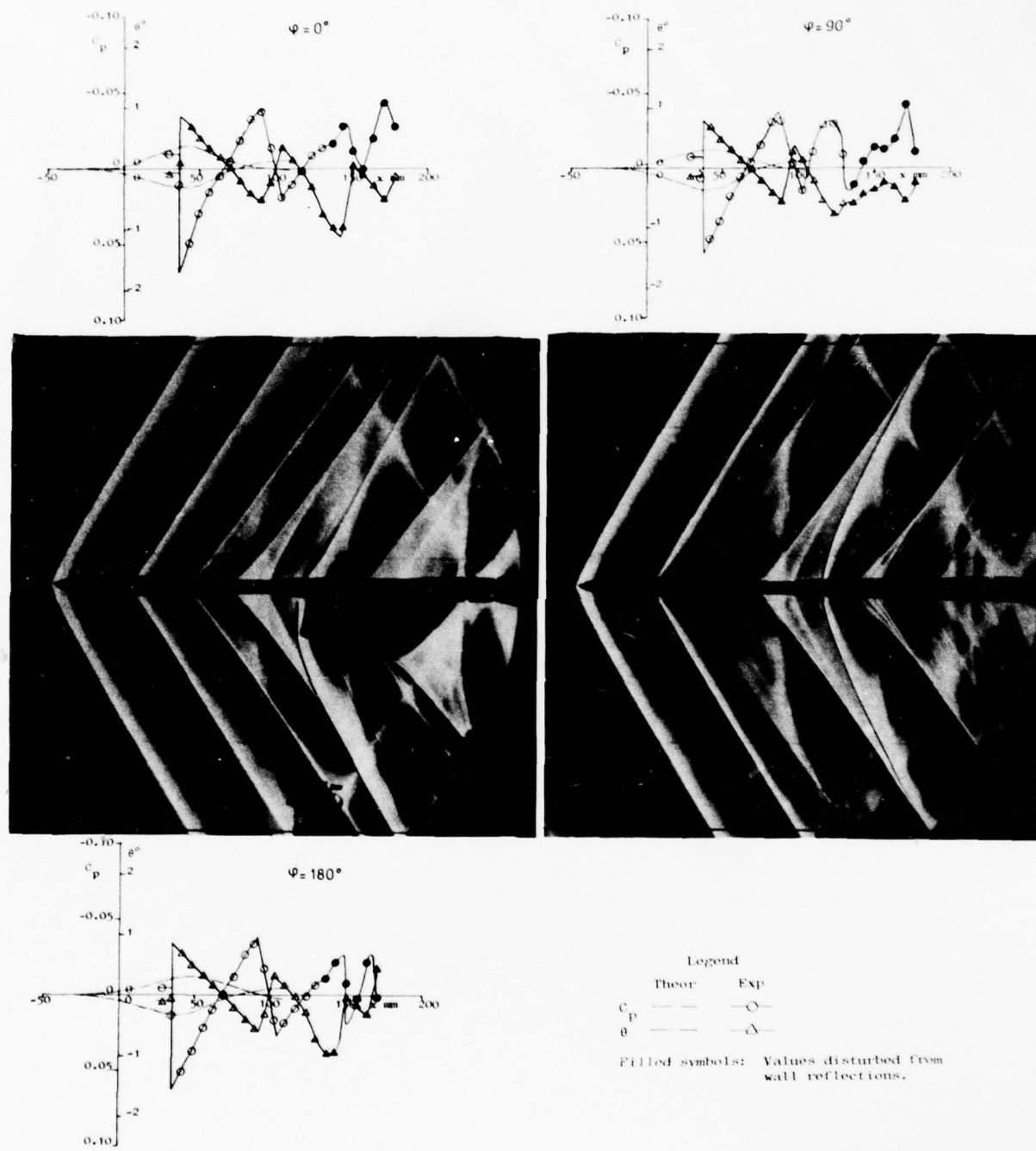


Figure 16. Theoretical and experimental flow field.

$M_\infty = 1.20$, $\alpha = 0^\circ$, $r = 153.2$ mm and $\varphi = 0^\circ, 90^\circ, 180^\circ$

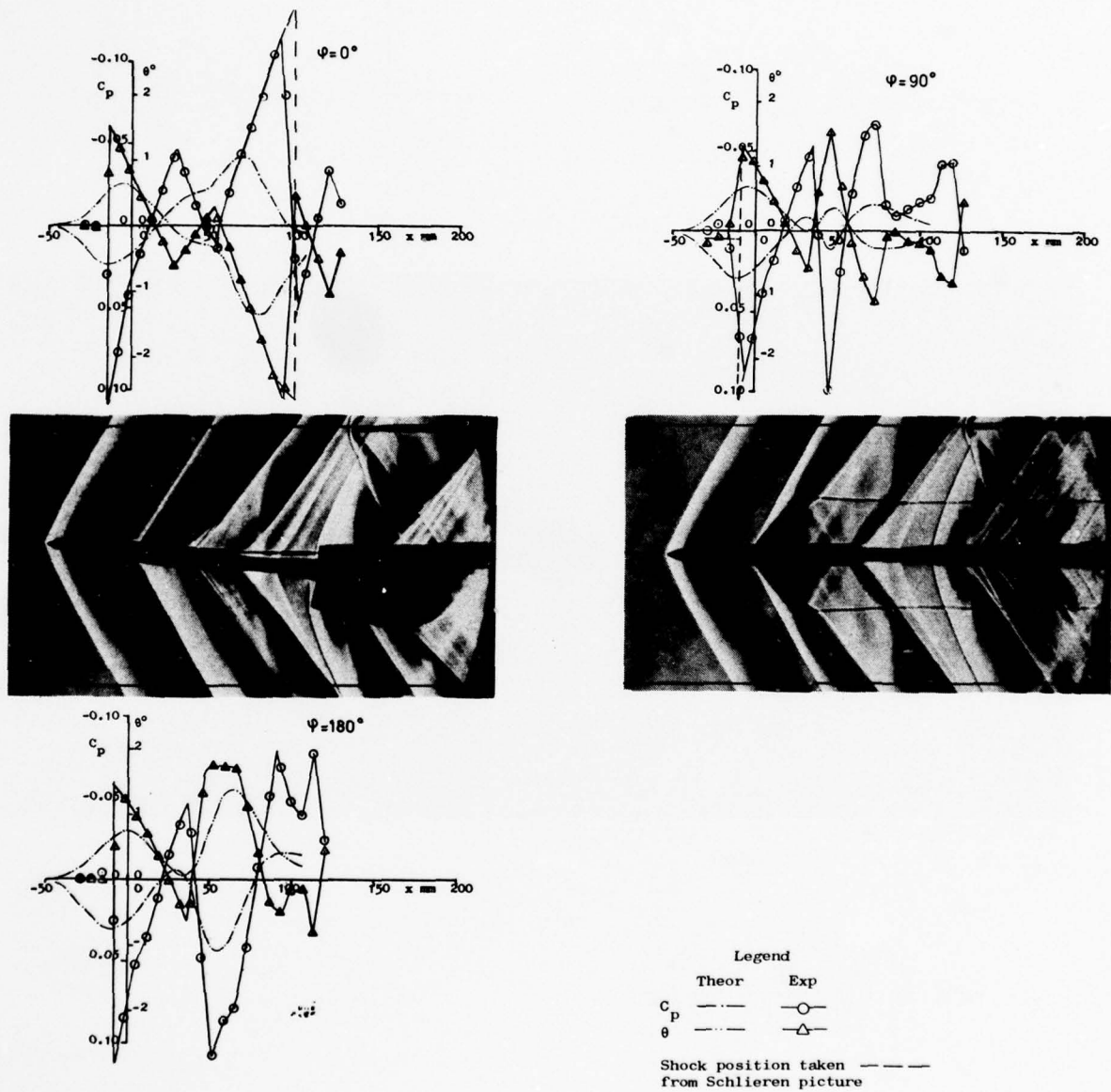


Figure 17. Theoretical and experimental flow field.

$M_\infty = 1.20$, $\alpha = 5.7^\circ$, $r = 73.2$ mm and $\varphi = 0^\circ, 90^\circ, 180^\circ$

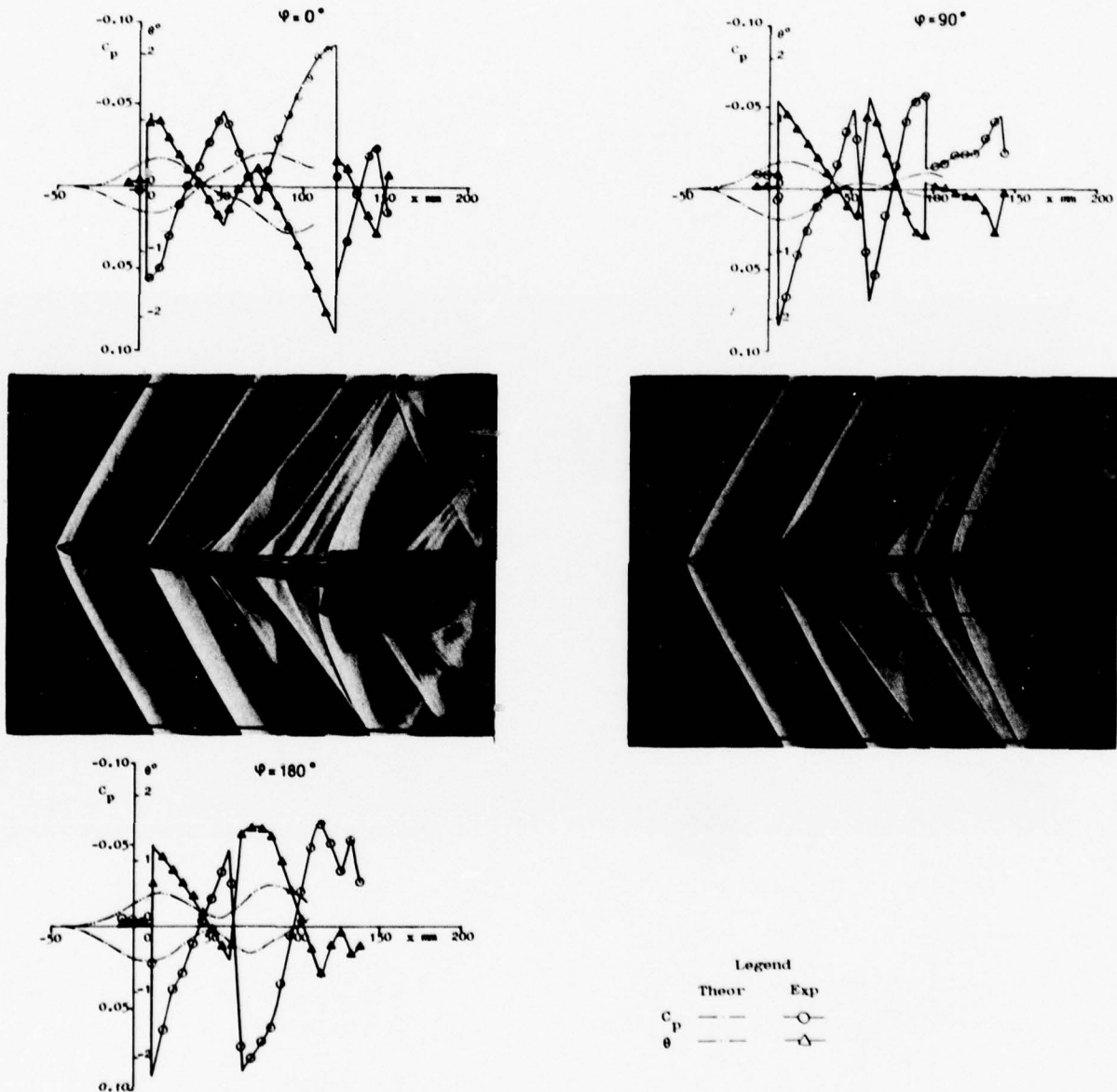


Figure 18. Theoretical and experimental flow field.

$M_\infty = 1.20$, $\alpha = 5.7^\circ$, $r = 103.2$ mm and $\phi = 0^\circ, 90^\circ, 180^\circ$

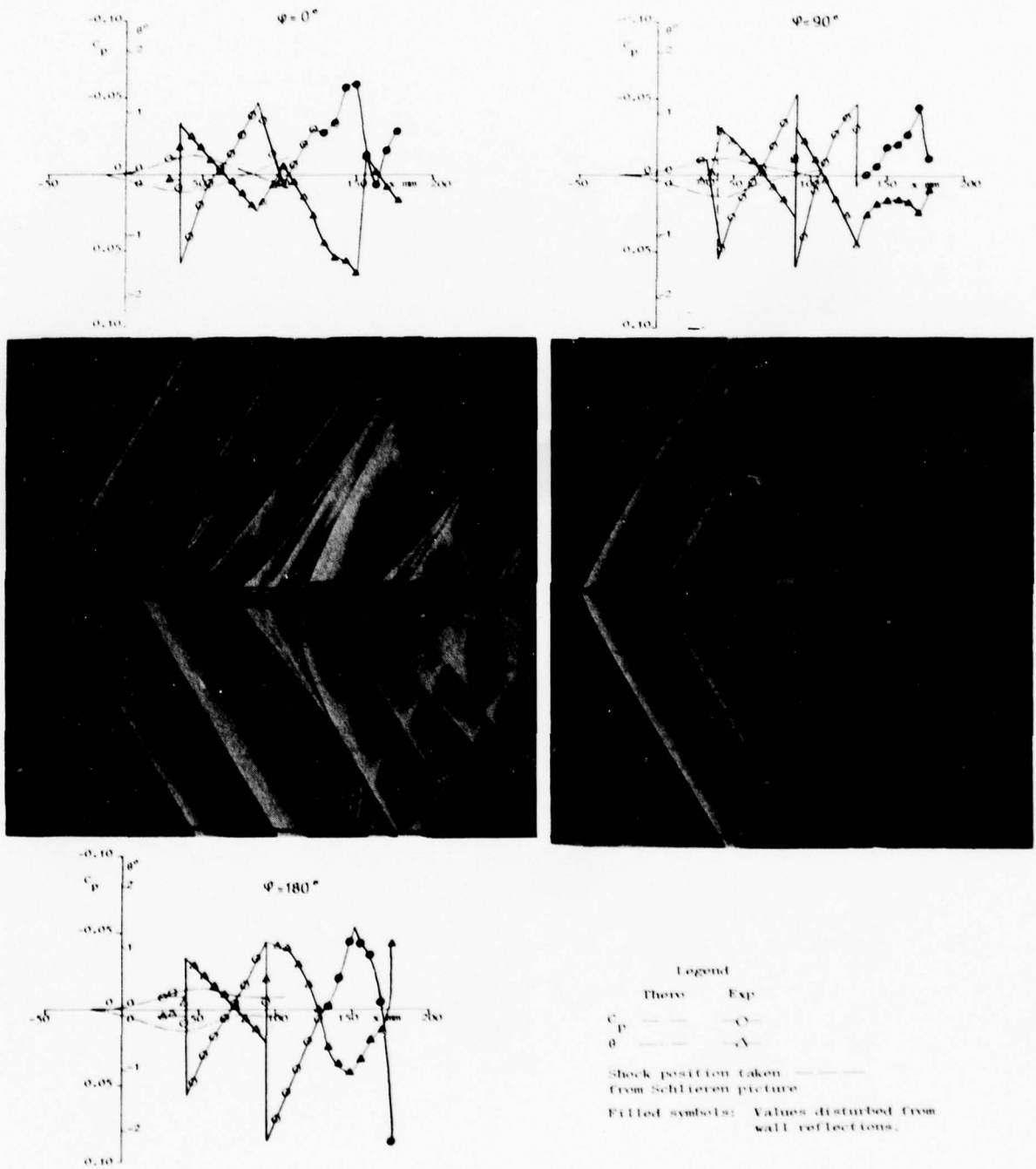


Figure 19. Theoretical and experimental flow field.

$M_\infty = 1.20$, $\alpha = 5.7^\circ$, $r = 153.2$ mm and $\varphi = 0^\circ, 90^\circ, 180^\circ$

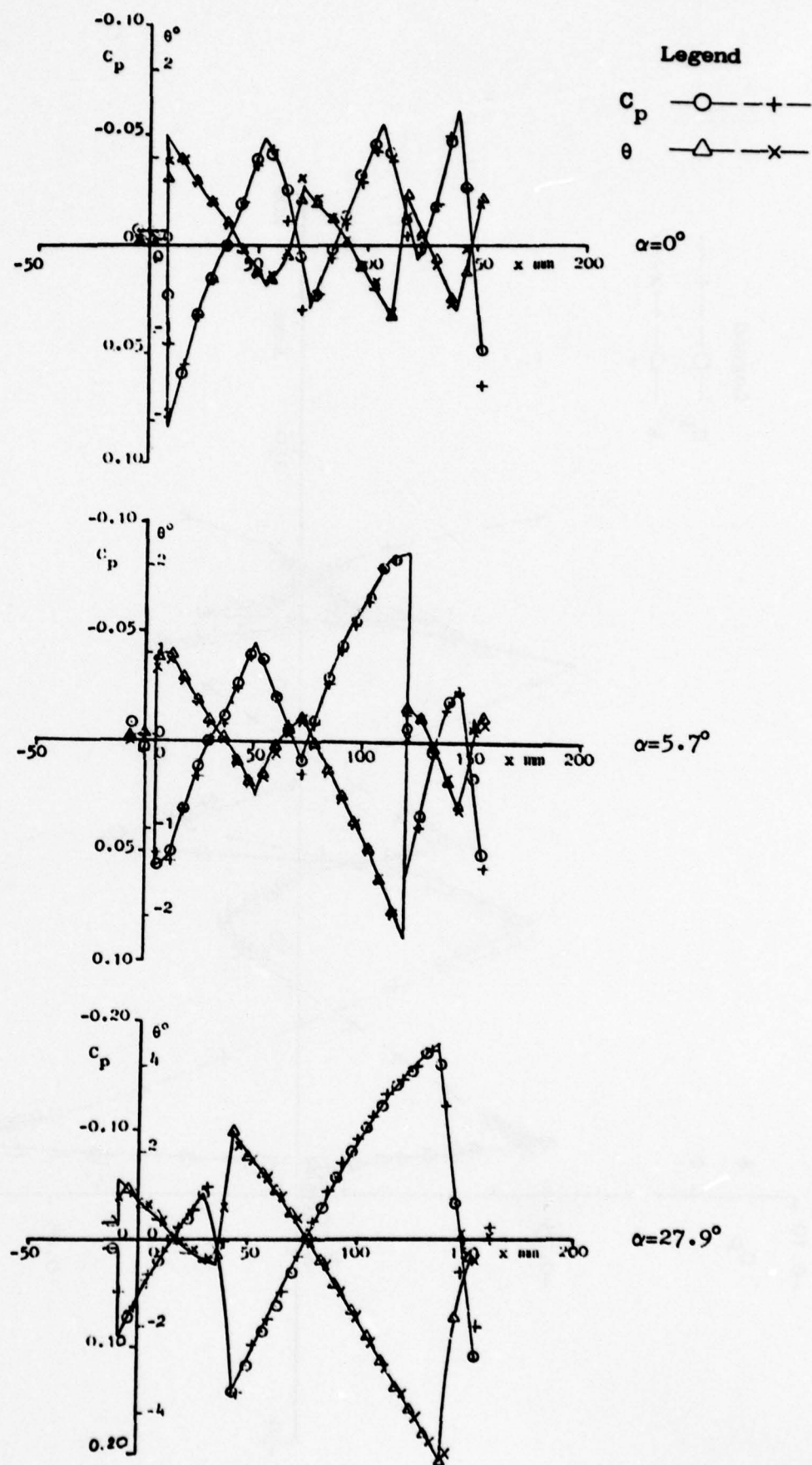


Figure 20. Repeatability checks.

$C_p(x)$ and $\theta(x)$ for the "top wall" ($\phi = 0^\circ$)

M = 1.2 Model blockage area 0.4% ($r = 103.2$ mm)

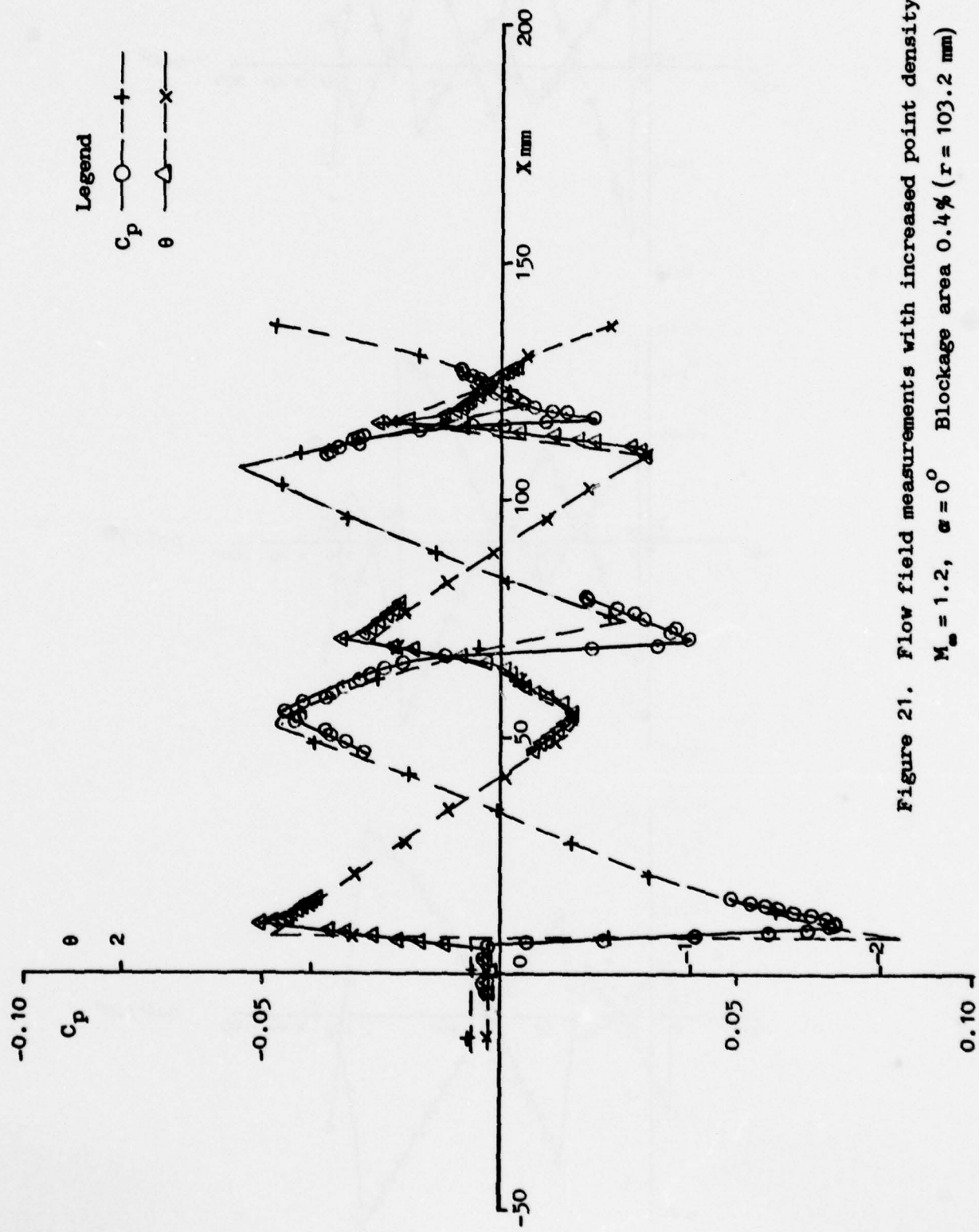


Figure 21. Flow field measurements with increased point density
 $M_\infty = 1.2, \alpha = 0^\circ \text{ Blockage area } 0.4\% (r = 103.2 \text{ mm})$

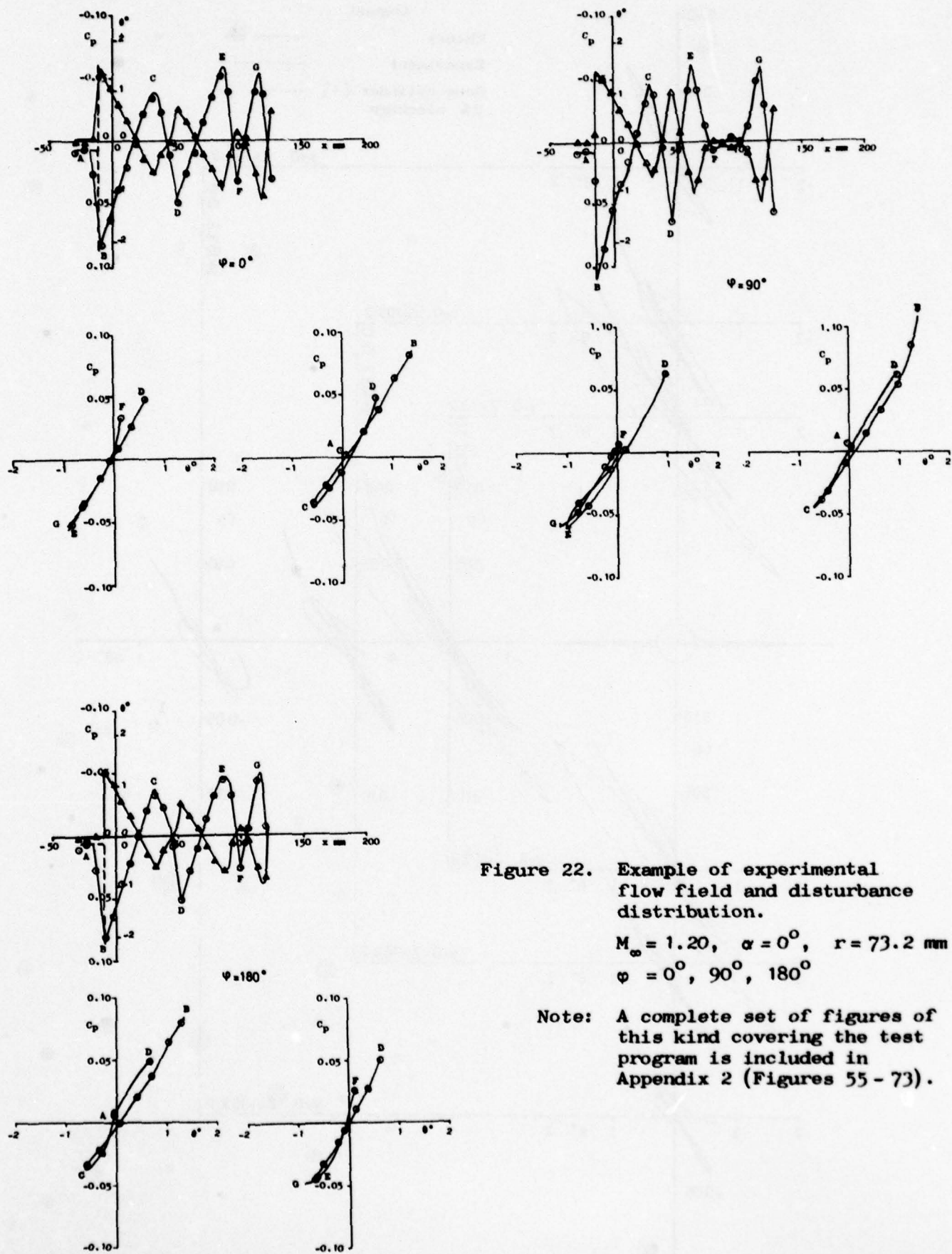


Figure 22. Example of experimental flow field and disturbance distribution.

$M_\infty = 1.20$, $\alpha = 0^\circ$, $r = 73.2$ mm
 $\phi = 0^\circ, 90^\circ, 180^\circ$

Note: A complete set of figures of this kind covering the test program is included in Appendix 2 (Figures 55 - 73).

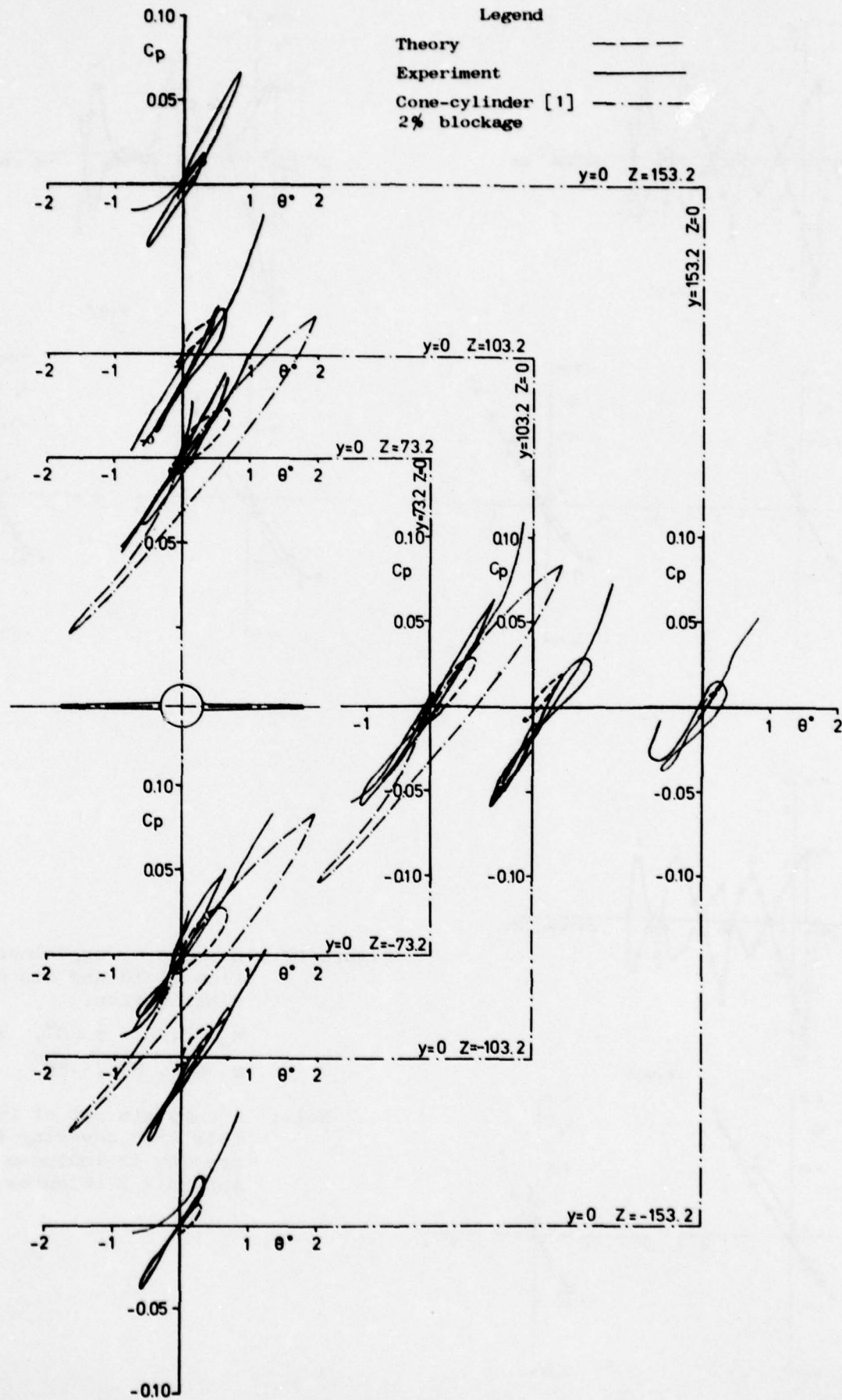


Figure 23. Theoretical and experimental disturbance distribution

$M_\infty = 1.20 \quad \alpha = 0^\circ$

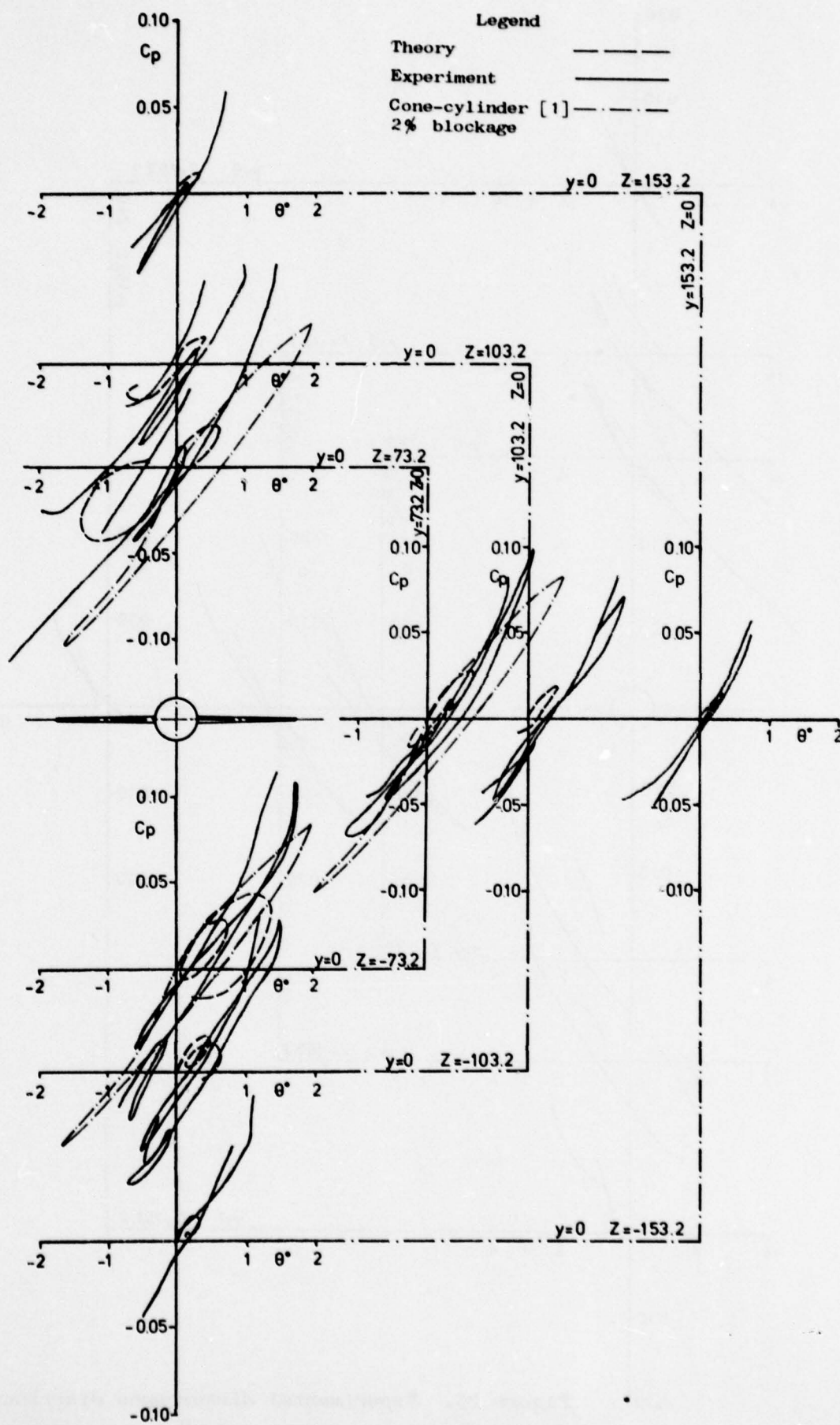


Figure 24. Theoretical and experimental disturbance distribution

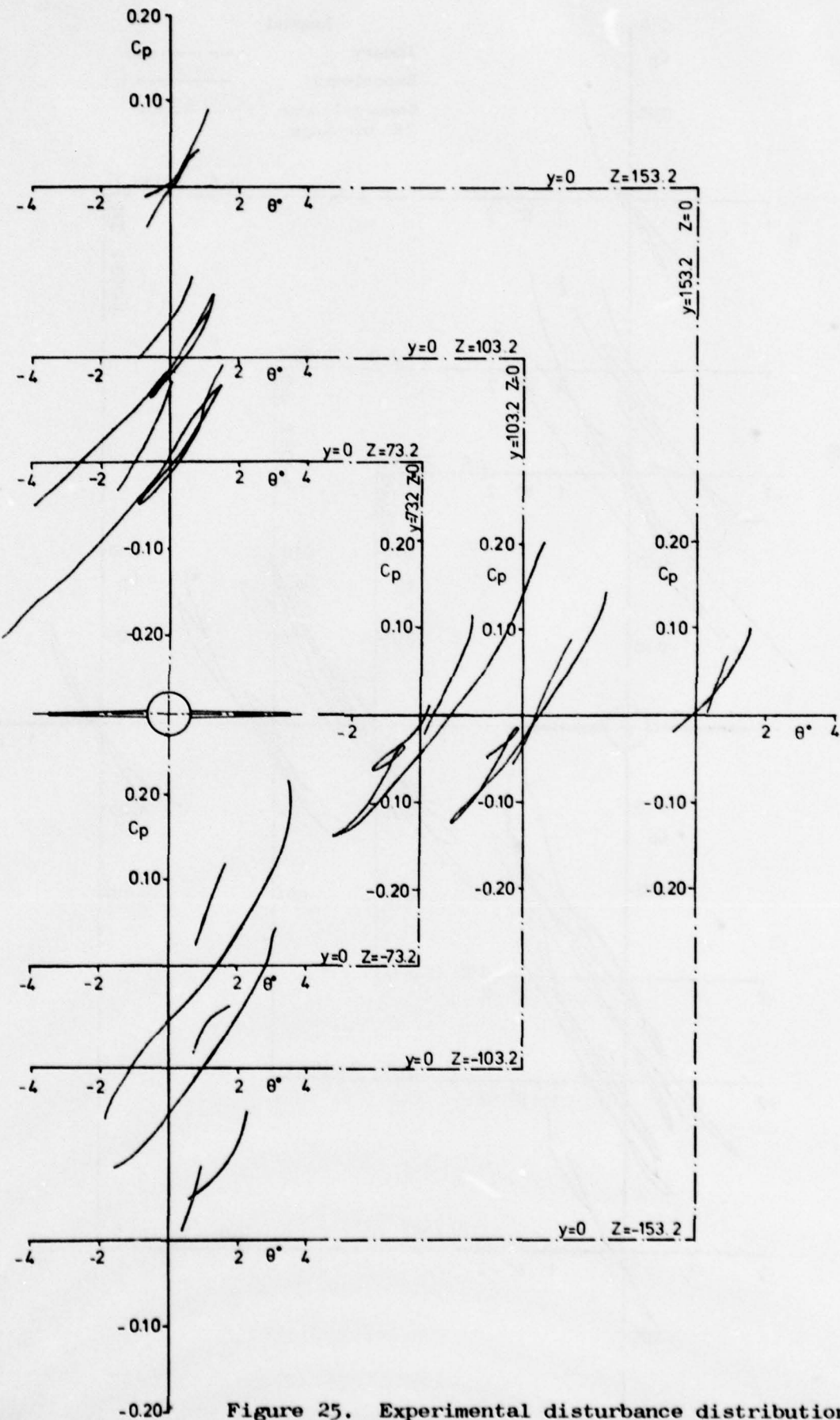


Figure 25. Experimental disturbance distribution.

 $M_\infty = 1.20, \alpha = 16.9^\circ$.

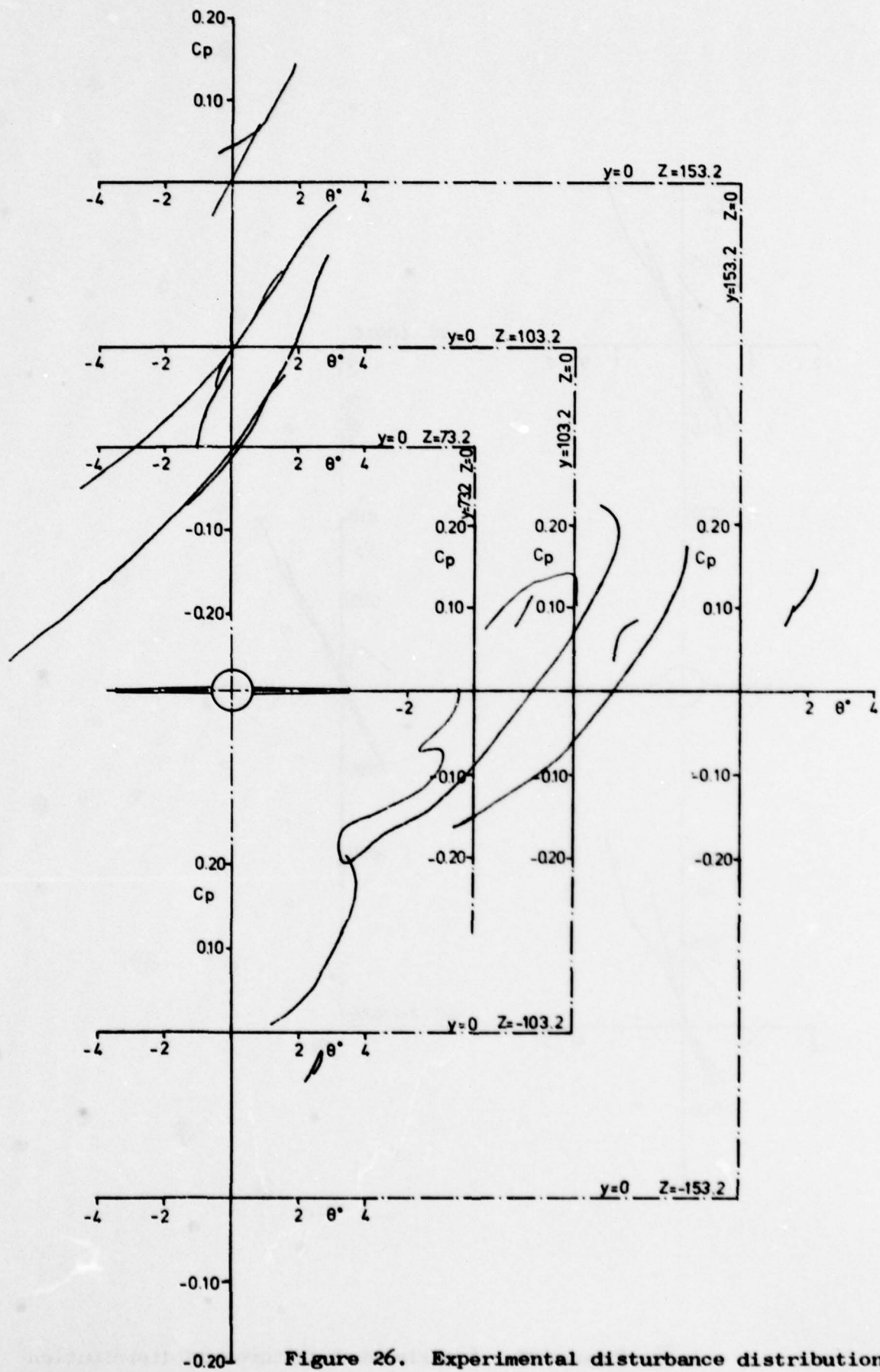


Figure 26. Experimental disturbance distribution.

$M_\infty = 1.20, \alpha = 27.9^\circ$.

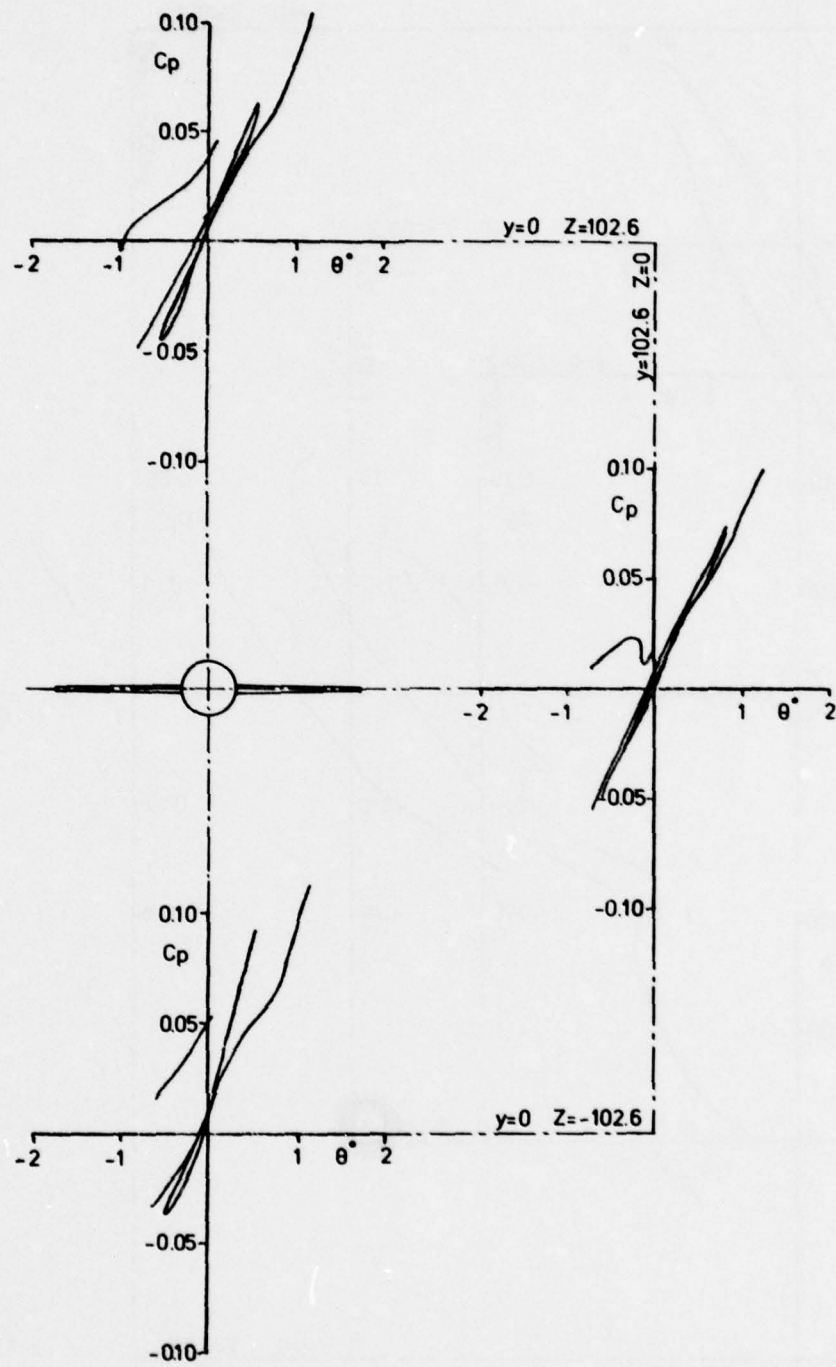


Figure 27. Experimental disturbance distribution
 $M_{\infty} = 1.15, \alpha = 0^{\circ}$.

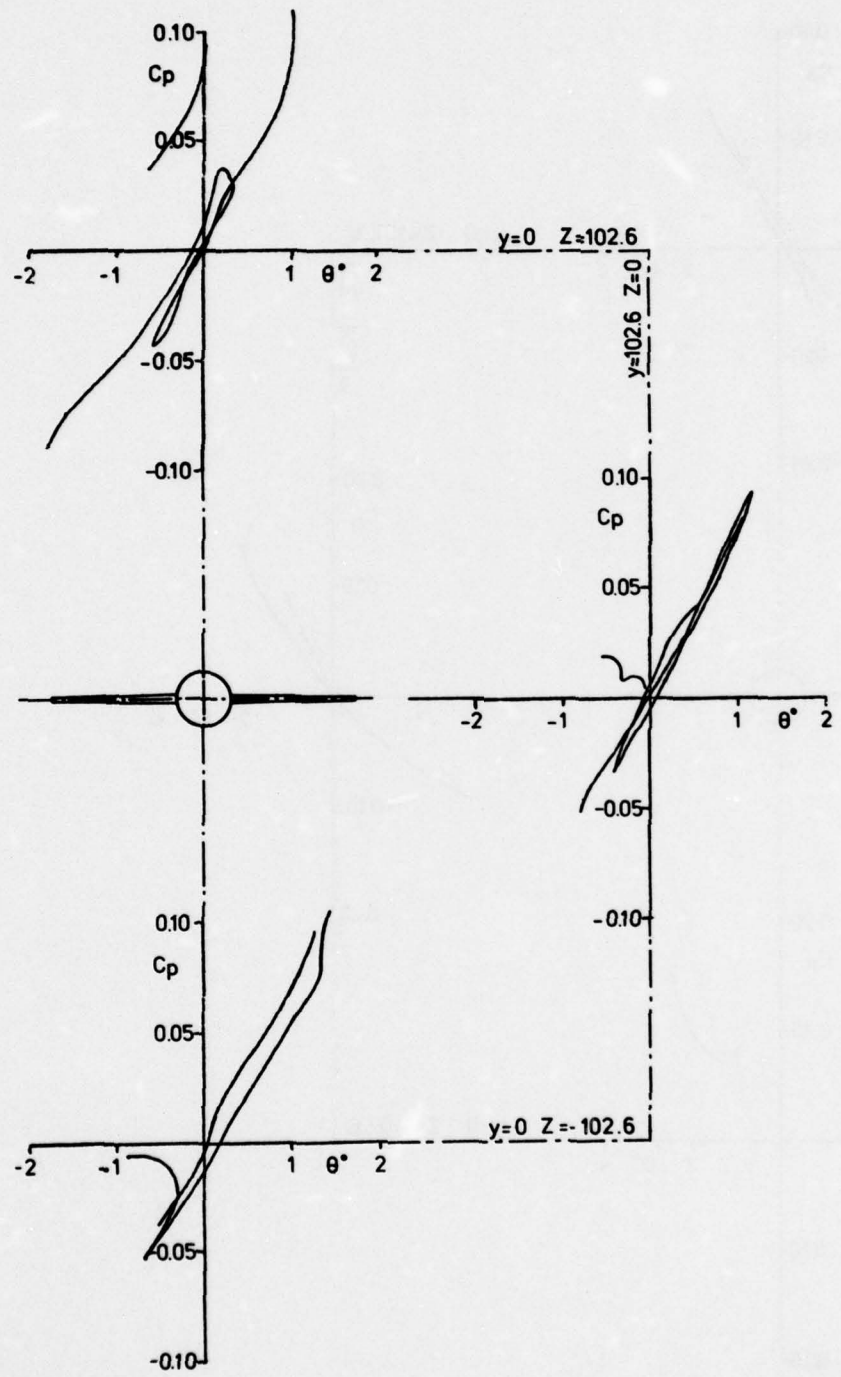


Figure 28. Experimental disturbance distribution
 $M_{\infty} = 1.15, \alpha = 5.7^{\circ}$.

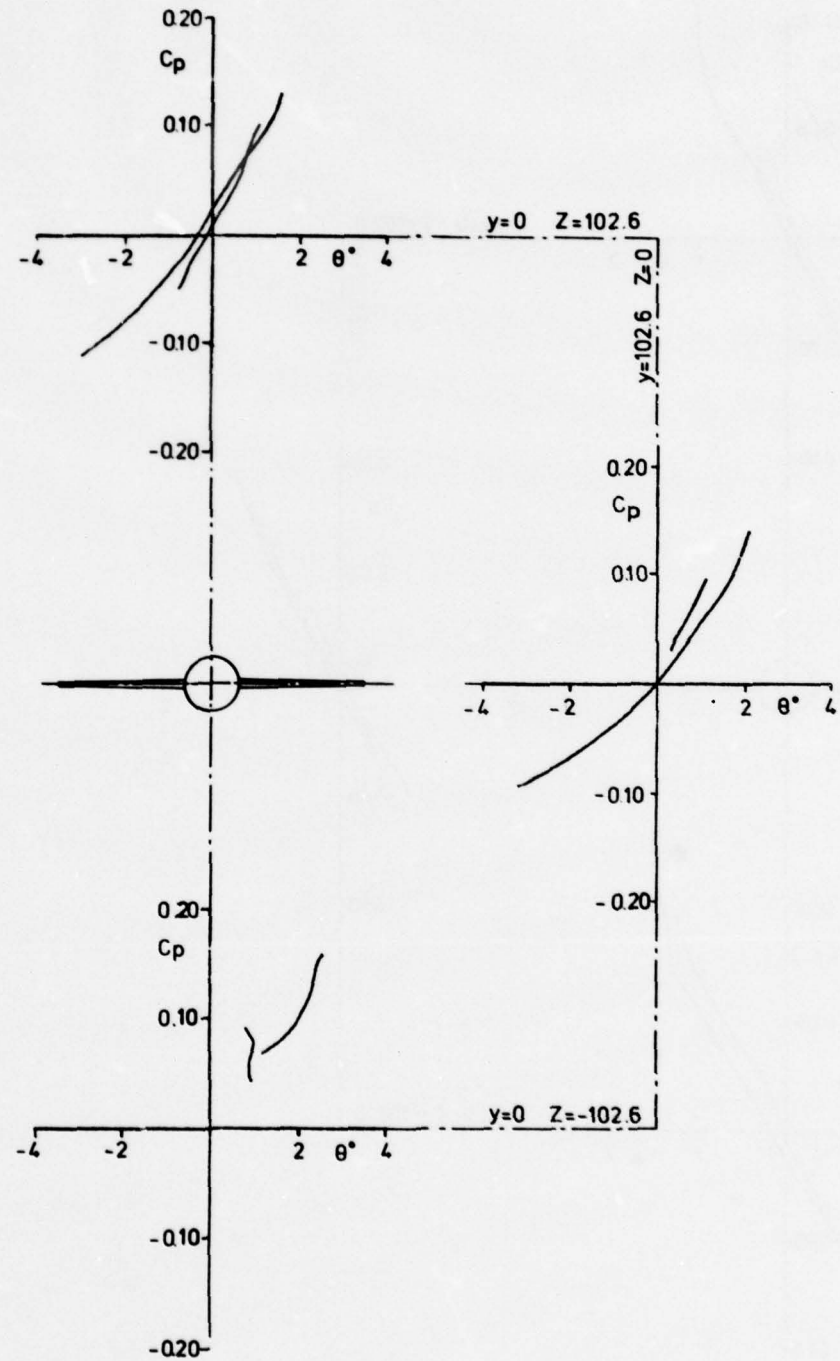


Figure 29. Experimental disturbance distribution
 $M_{\infty} = 1.15, \alpha = 16.8^{\circ}$.

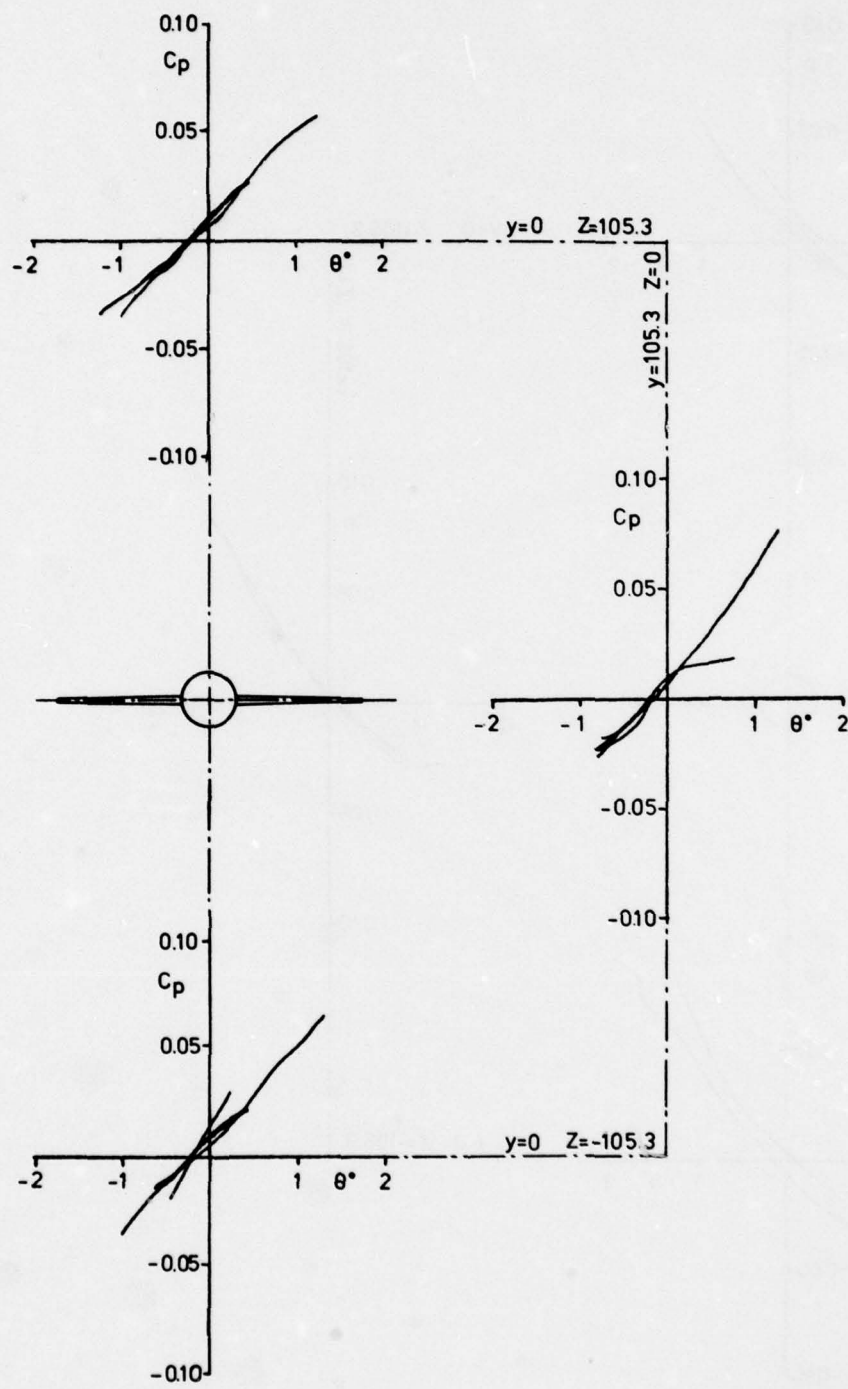


Figure 30. Experimental disturbance distribution
 $M_{\infty} = 1.30, \alpha = 0^{\circ}$.

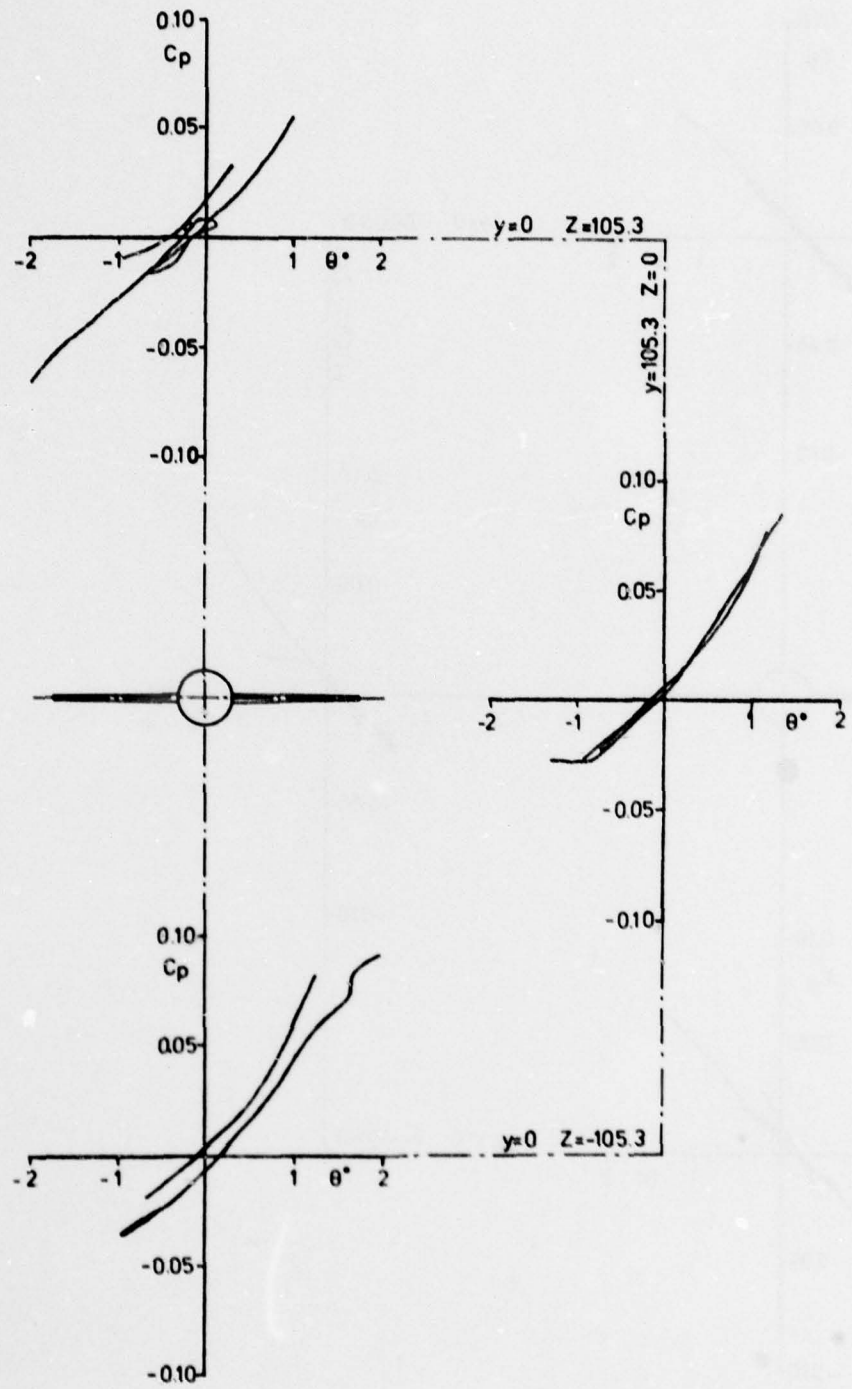


Figure 31. Experimental disturbance distribution
 $M_\infty = 1.30, \alpha = 5.7^\circ$.

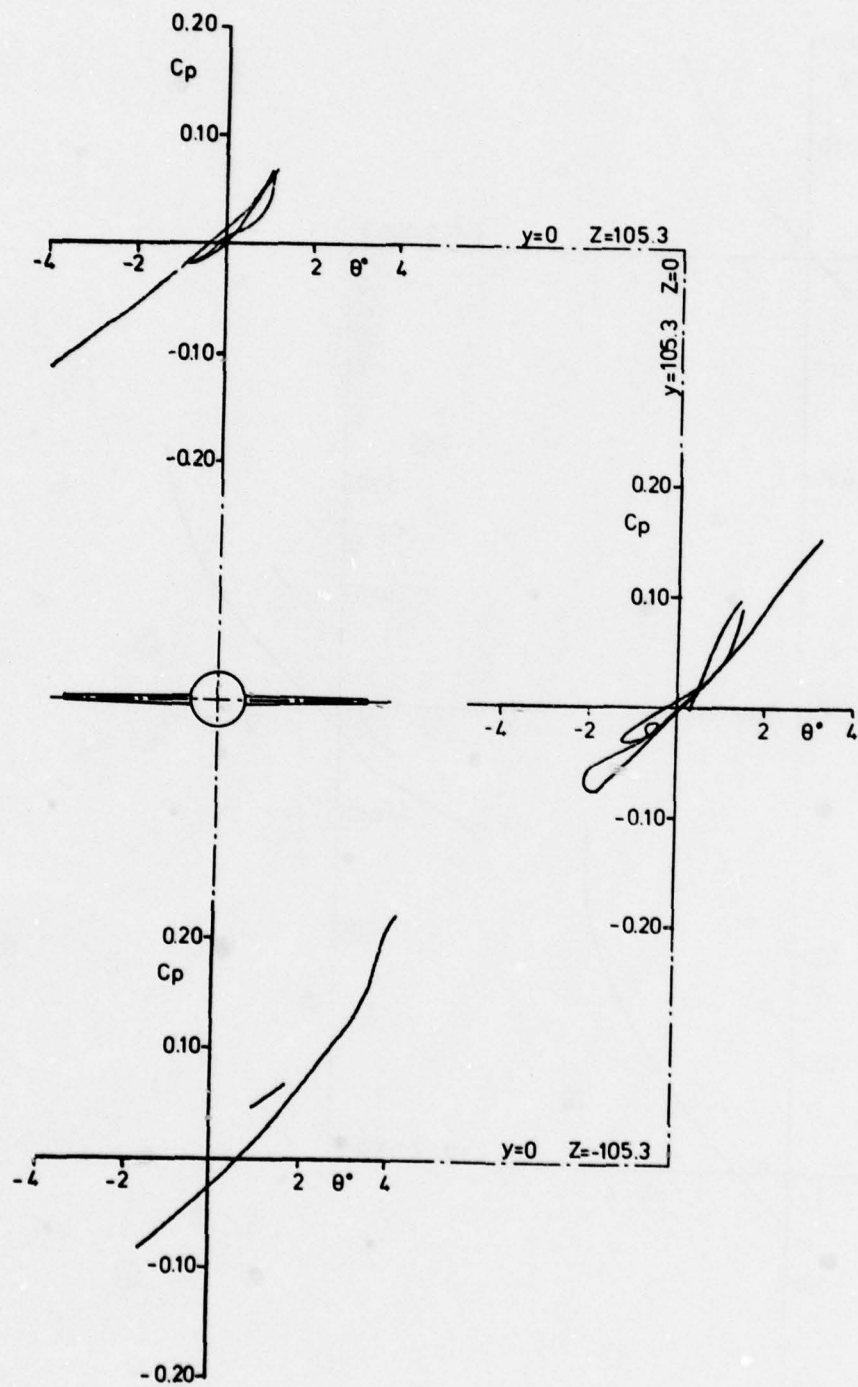


Figure 32. Experimental disturbance distribution
 $M_{\infty} = 1.30, \alpha = 17.1^{\circ}$.

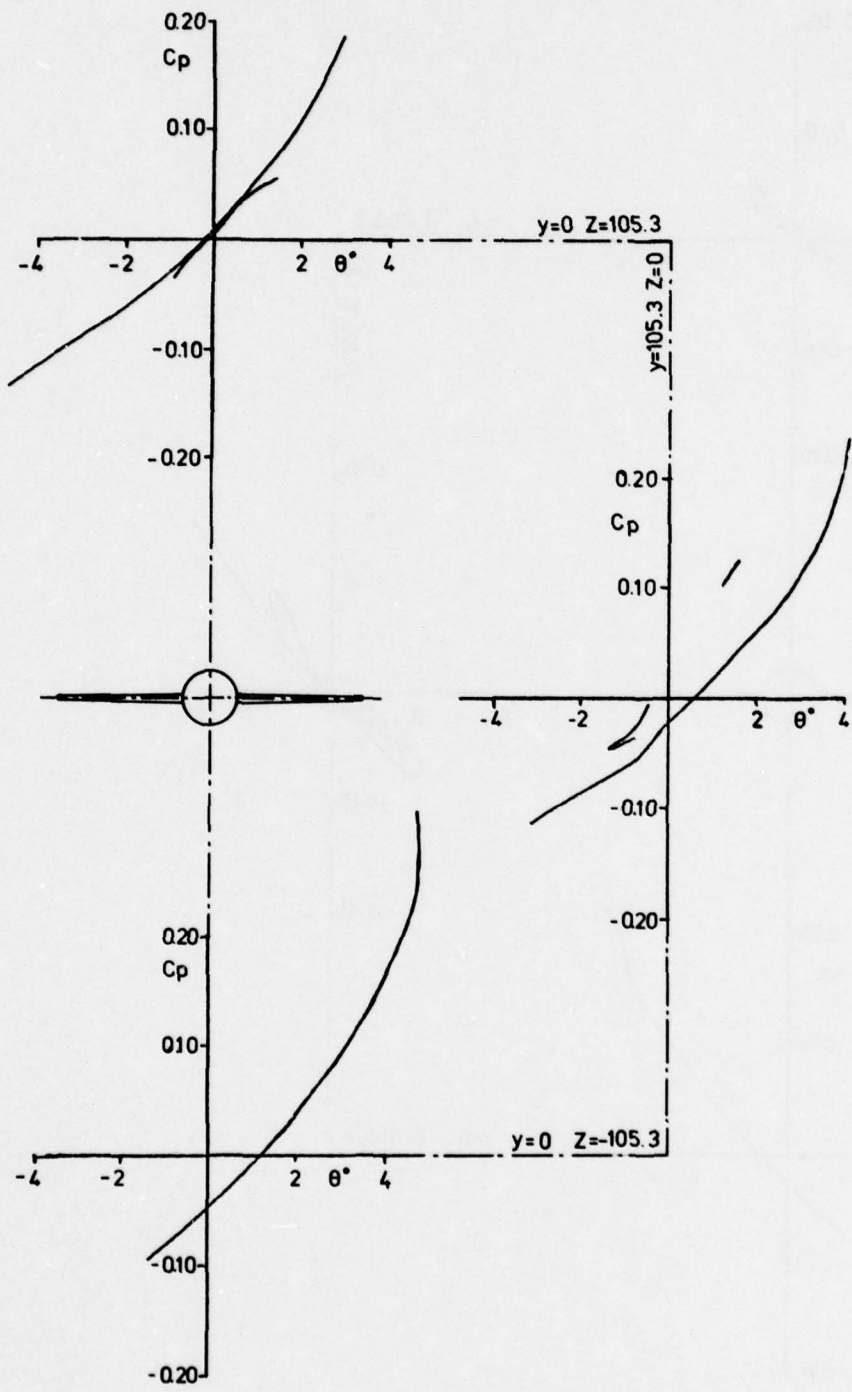


Figure 33. Experimental disturbance distribution
 $M_{\infty} = 1.30, \alpha = 28.3^{\circ}$.

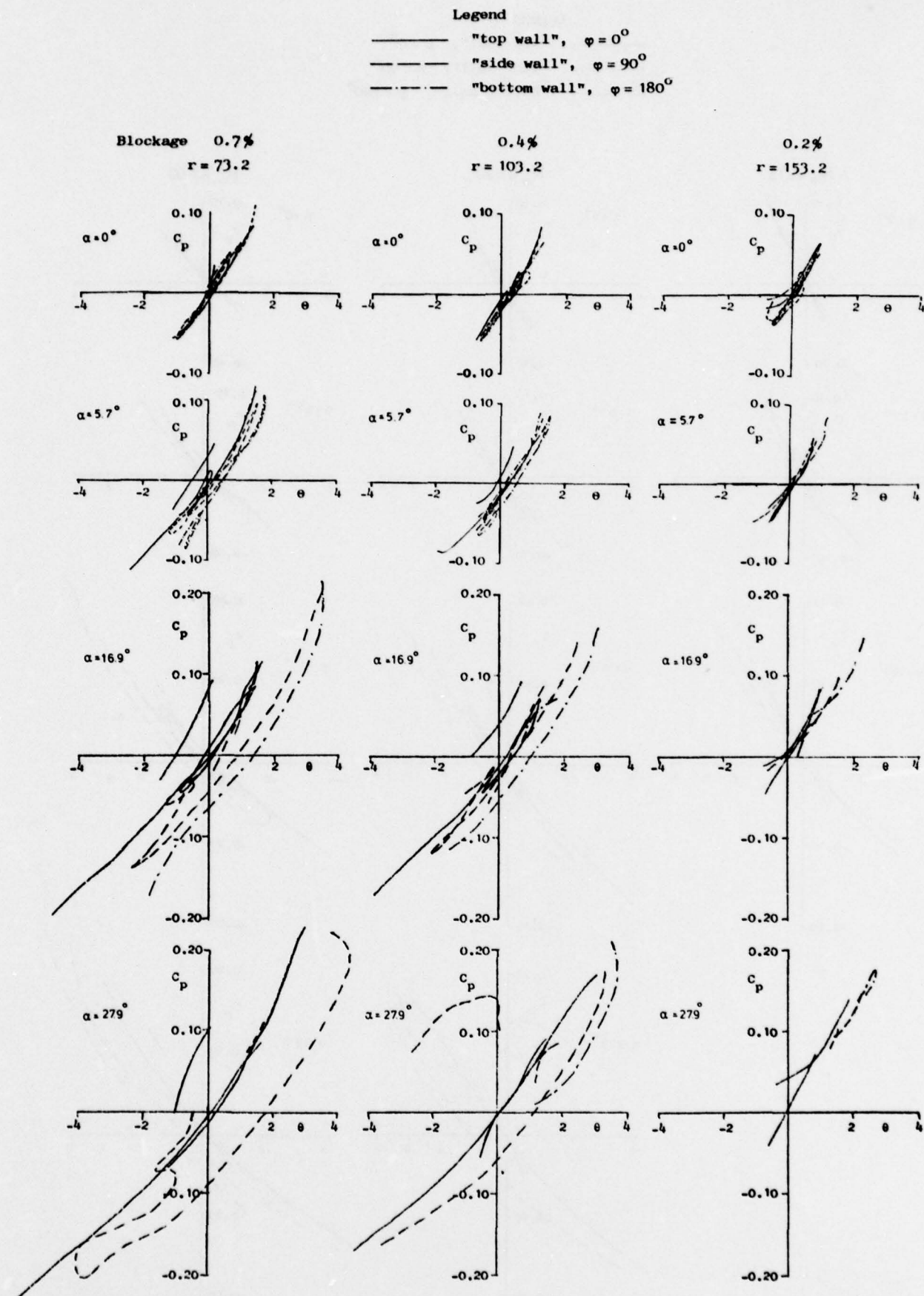


Figure 34. Experimental disturbance distribution $C_p(\theta)$ due to wing-body configuration for model blockage areas 0.2 - 0.7% and angles of attack $\alpha = 0^\circ - 28^\circ$, $M_\infty = 1.20$.

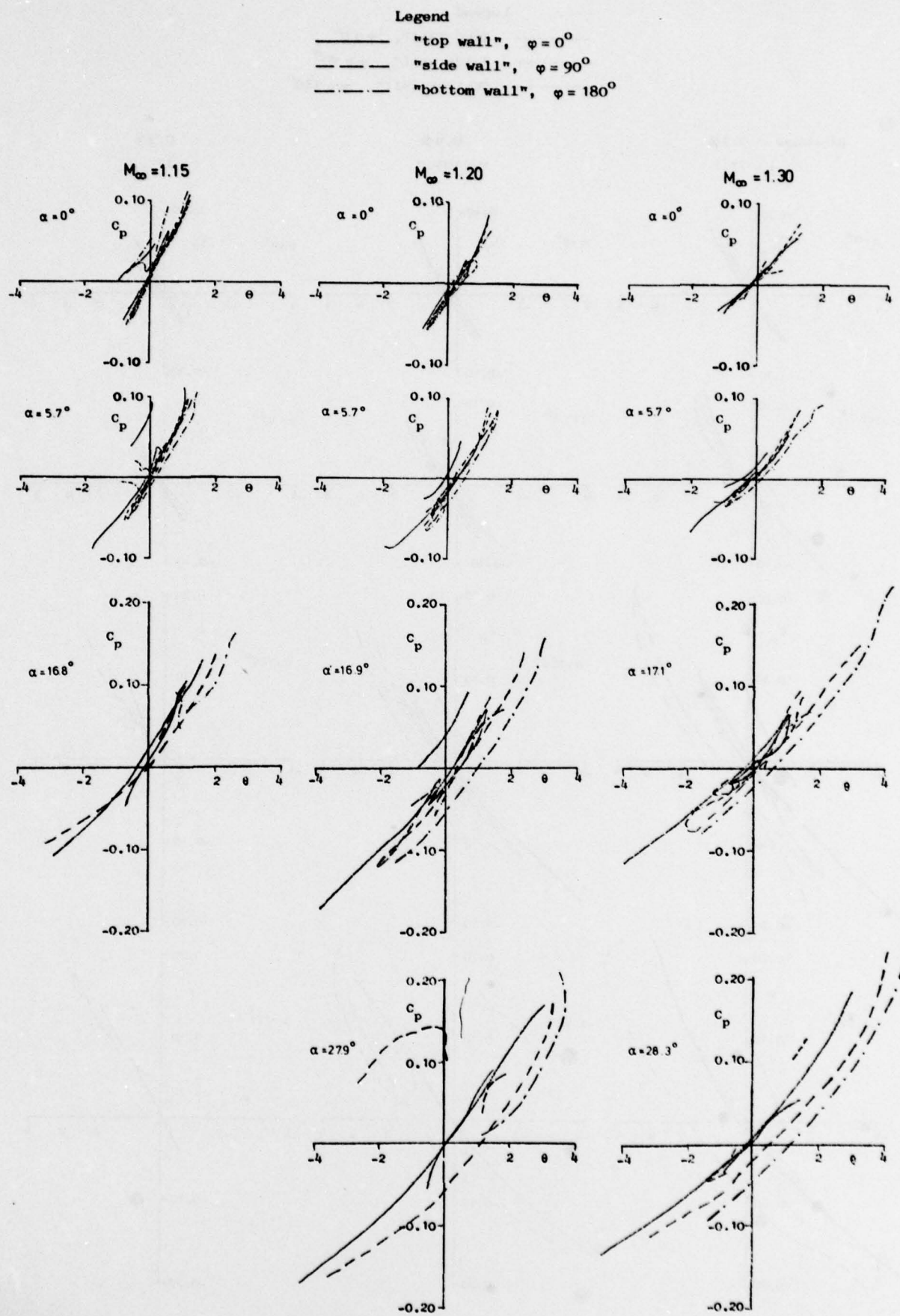


Figure 35. Experimental disturbance distribution $C_p(\theta)$ due to wing-body configuration for Mach numbers $M_\infty = 1.15, 1.20, 1.30$ and angles of attack $\alpha = 0^\circ - 28^\circ$. Blockage area 0.4%. $r_n = 100$ mm.

A P P E N D I X 1

Figures 36 - 54

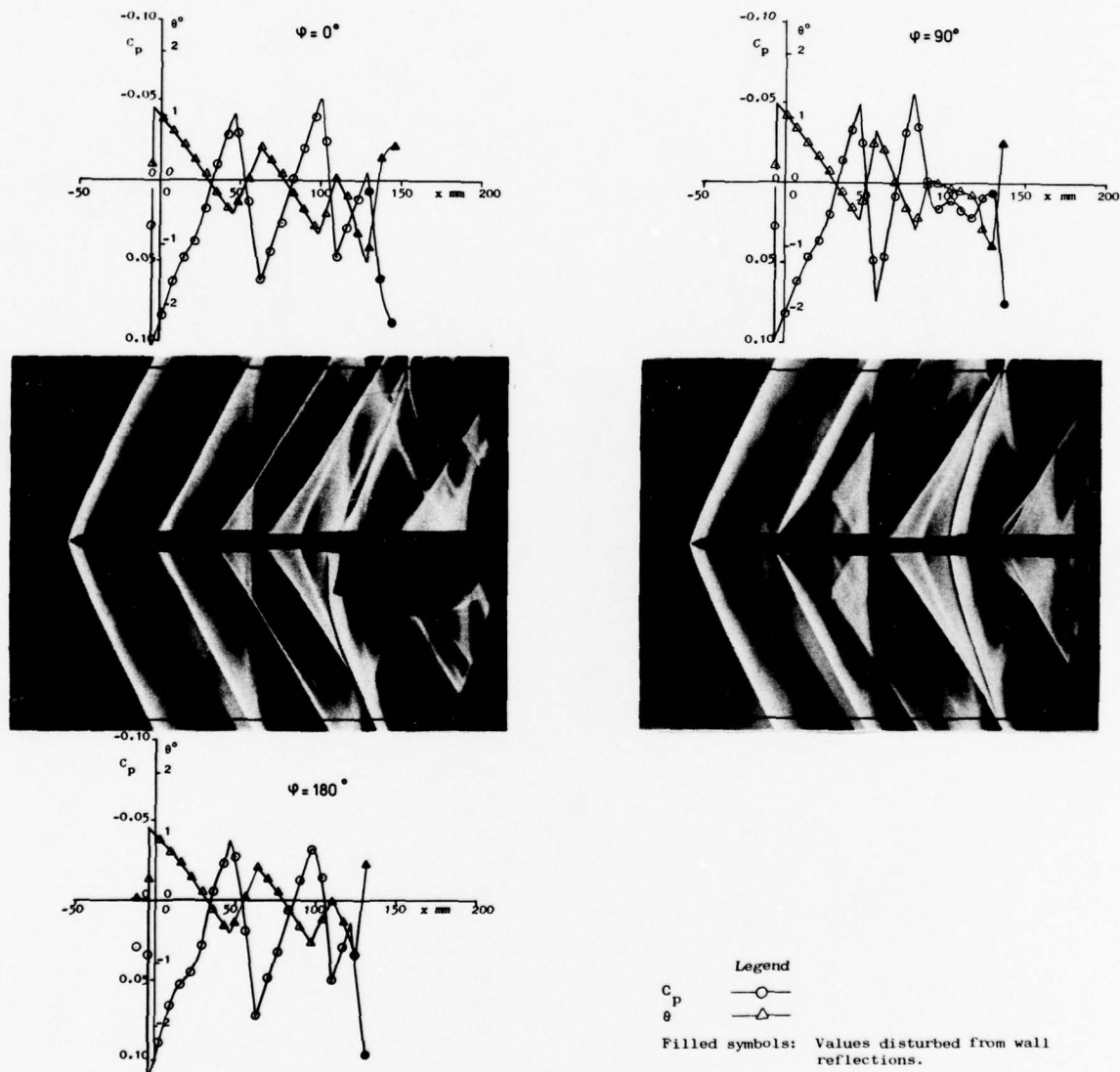


Figure 36. Experimental flow field

$M_\infty = 1.15$, $\alpha = 0^\circ$, $r = 102.6$ mm and $\varphi = 0^\circ, 90^\circ, 180^\circ$

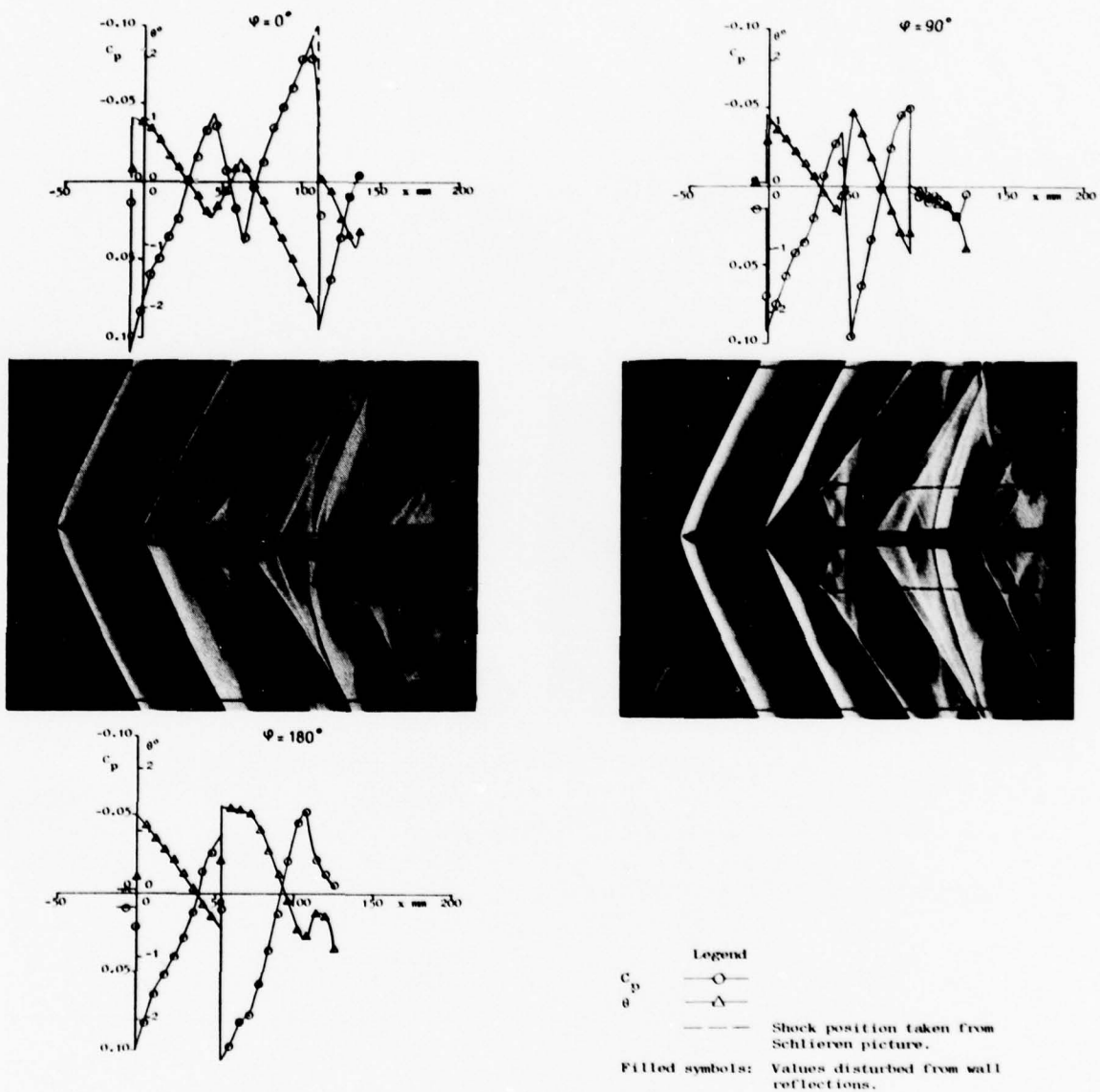


Figure 37. Experimental flow field

$M_\infty = 1.15$, $\alpha = 5.7^\circ$, $r = 102.6 \text{ mm}$ and $\varphi = 0^\circ, 90^\circ, 180^\circ$

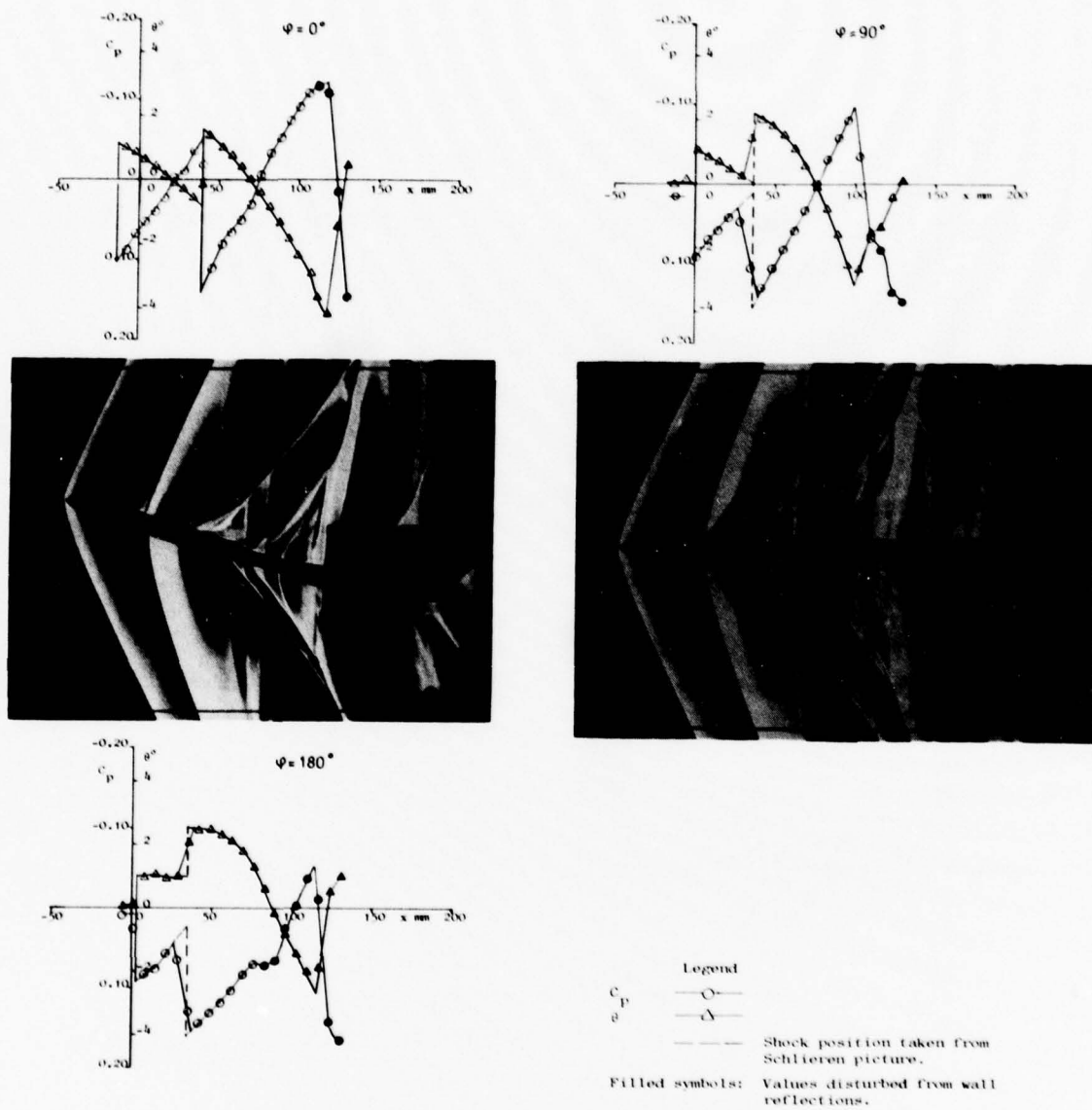


Figure 38. Experimental flow field

$M_\infty = 1.15$, $\alpha = 16.8^\circ$, $r = 102.6$ mm and $\phi = 0^\circ, 90^\circ, 180^\circ$

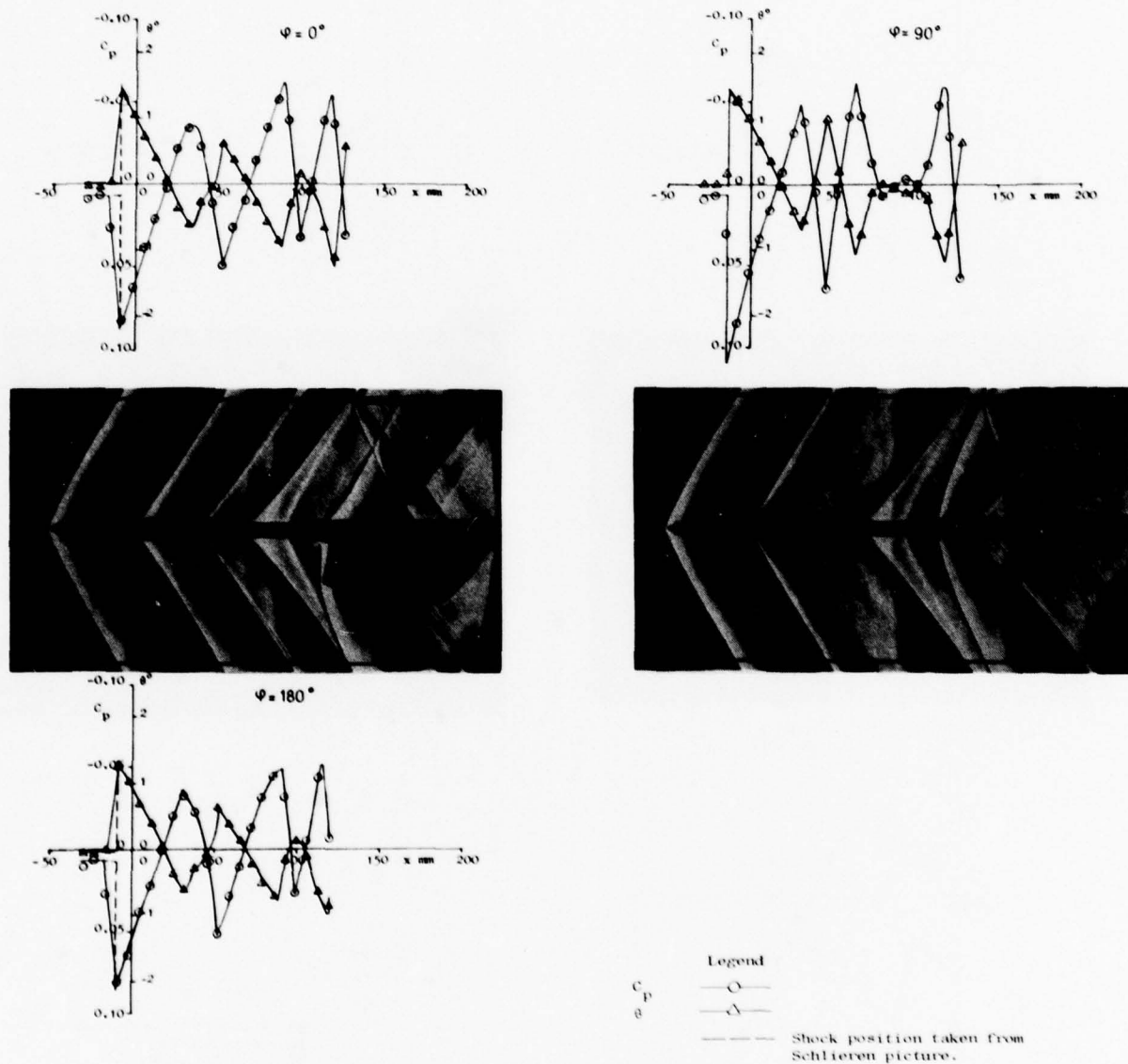


Figure 39. Experimental flow field

$M_\infty = 1.20$, $\alpha = 0^\circ$, $r = 73.2 \text{ mm}$ and $\varphi = 0^\circ, 90^\circ, 180^\circ$

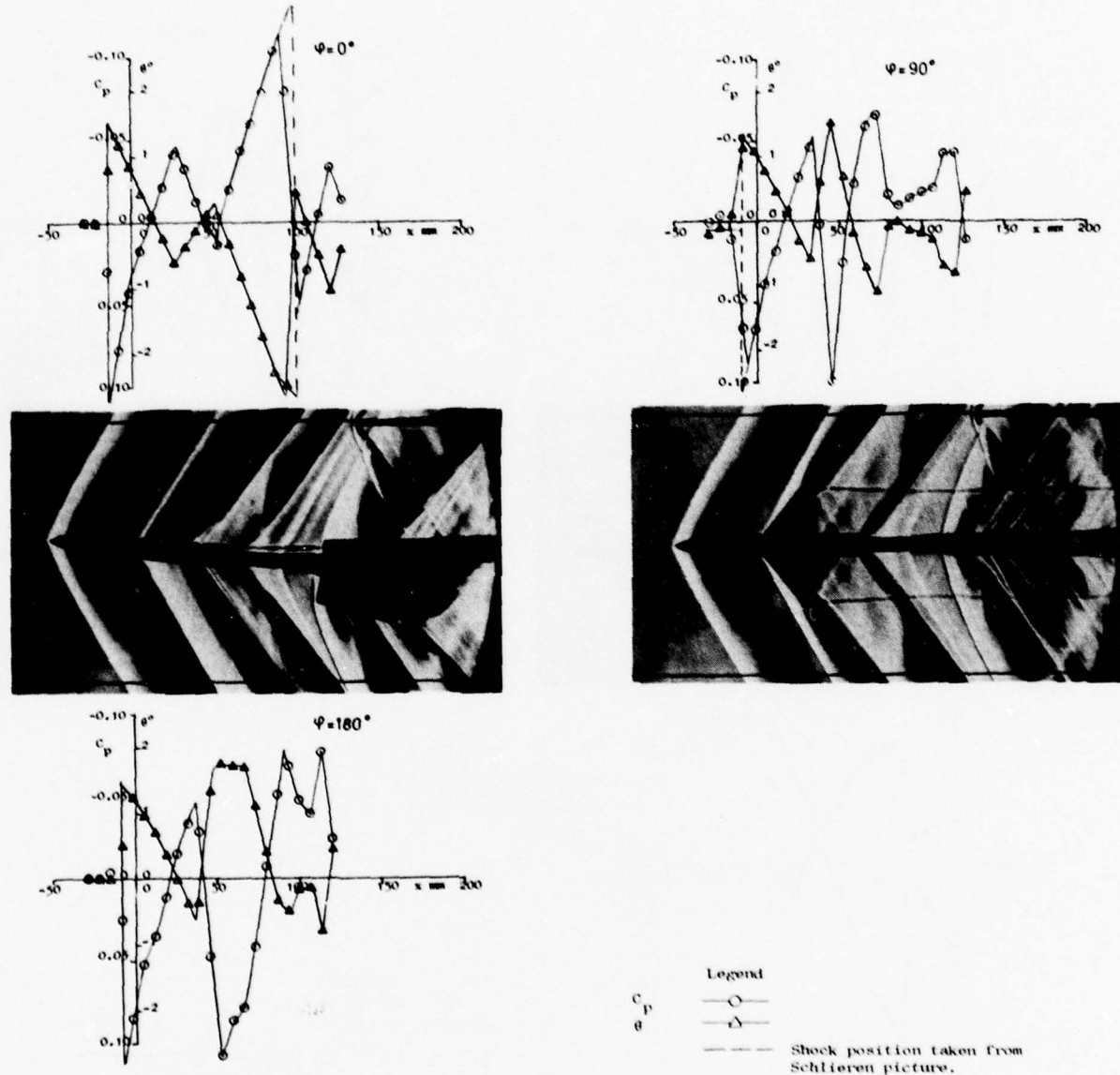


Figure 40. Experimental flow field

$M_\infty = 1.20$, $\alpha = 5.7^\circ$, $r = 73.2$ mm and $\varphi = 0^\circ, 90^\circ, 180^\circ$

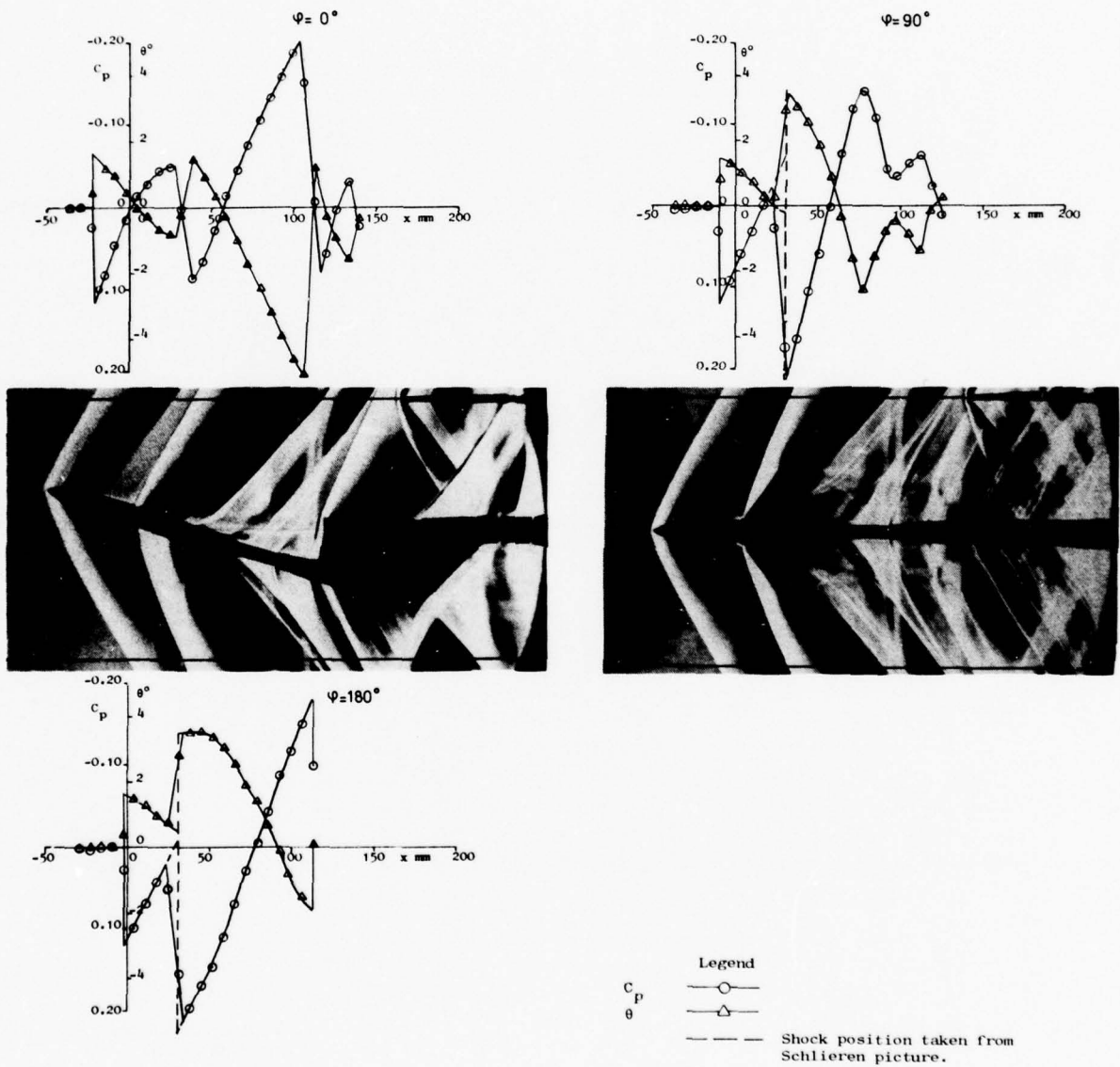


Figure 41. Experimental flow field

$$M_\infty = 1.20, \quad \alpha = 16.9^\circ, \quad r = 73.2 \text{ mm} \quad \text{and} \quad \varphi = 0^\circ, 90^\circ, 180^\circ$$

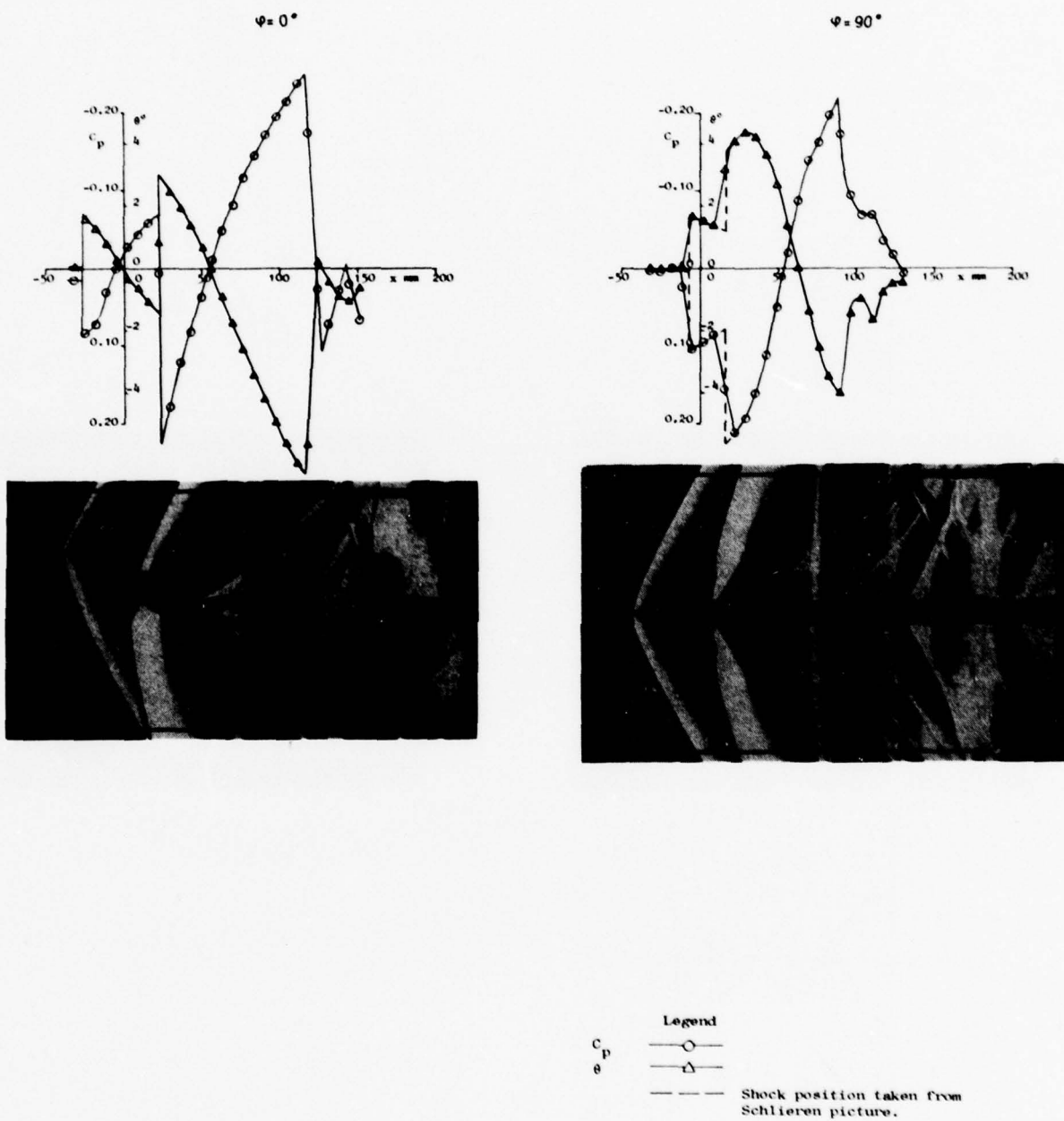


Figure 42. Experimental flow field

$M_\infty = 1.20$, $\alpha = 27.9^\circ$, $r = 73.2 \text{ mm}$ and $\varphi = 0^\circ, 90^\circ, 180^\circ$

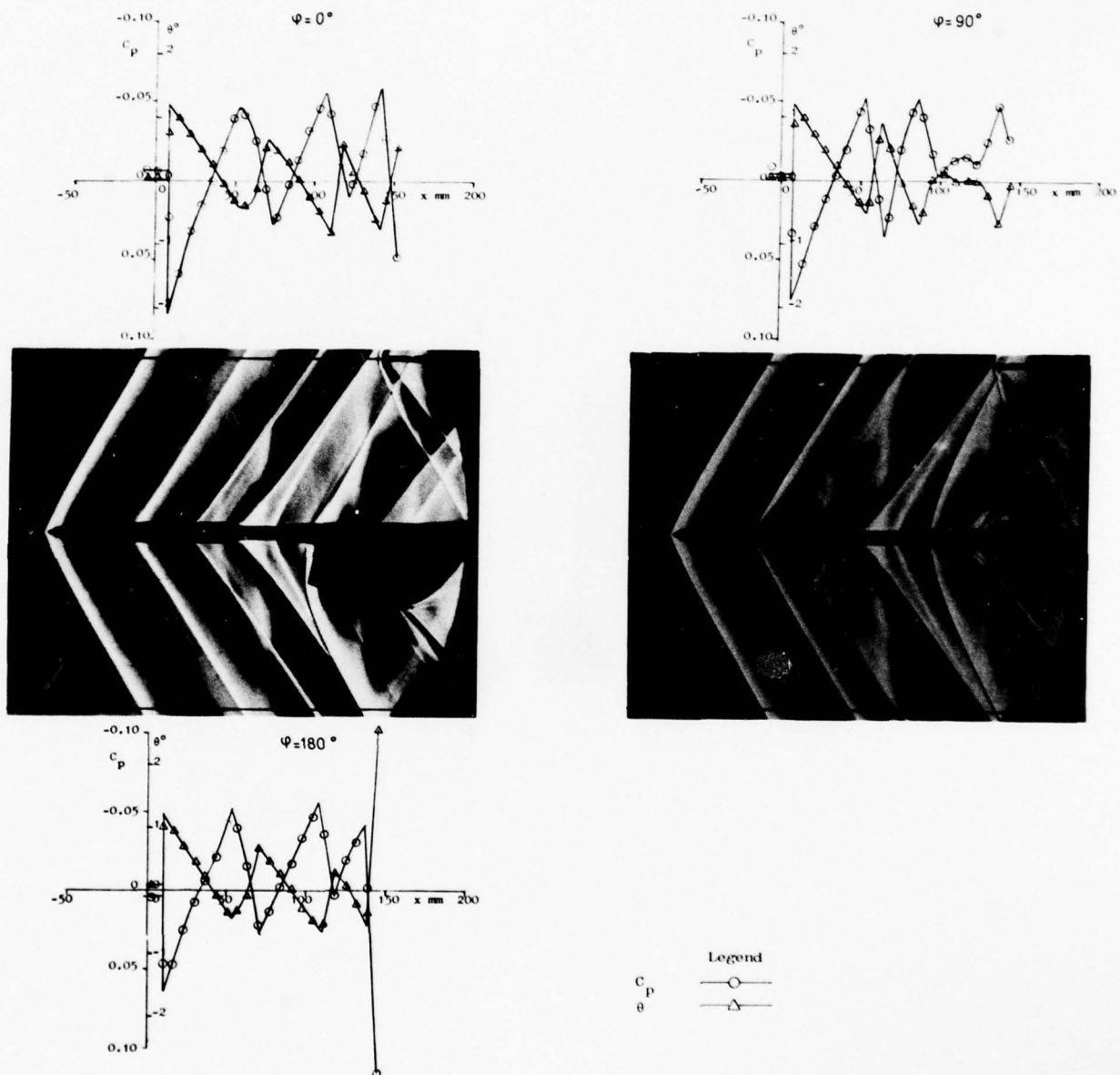


Figure 43. Experimental flow field

$M_\infty = 1.20$, $\alpha = 0^\circ$, $r = 103.2$ mm and $\varphi = 0^\circ, 90^\circ, 180^\circ$

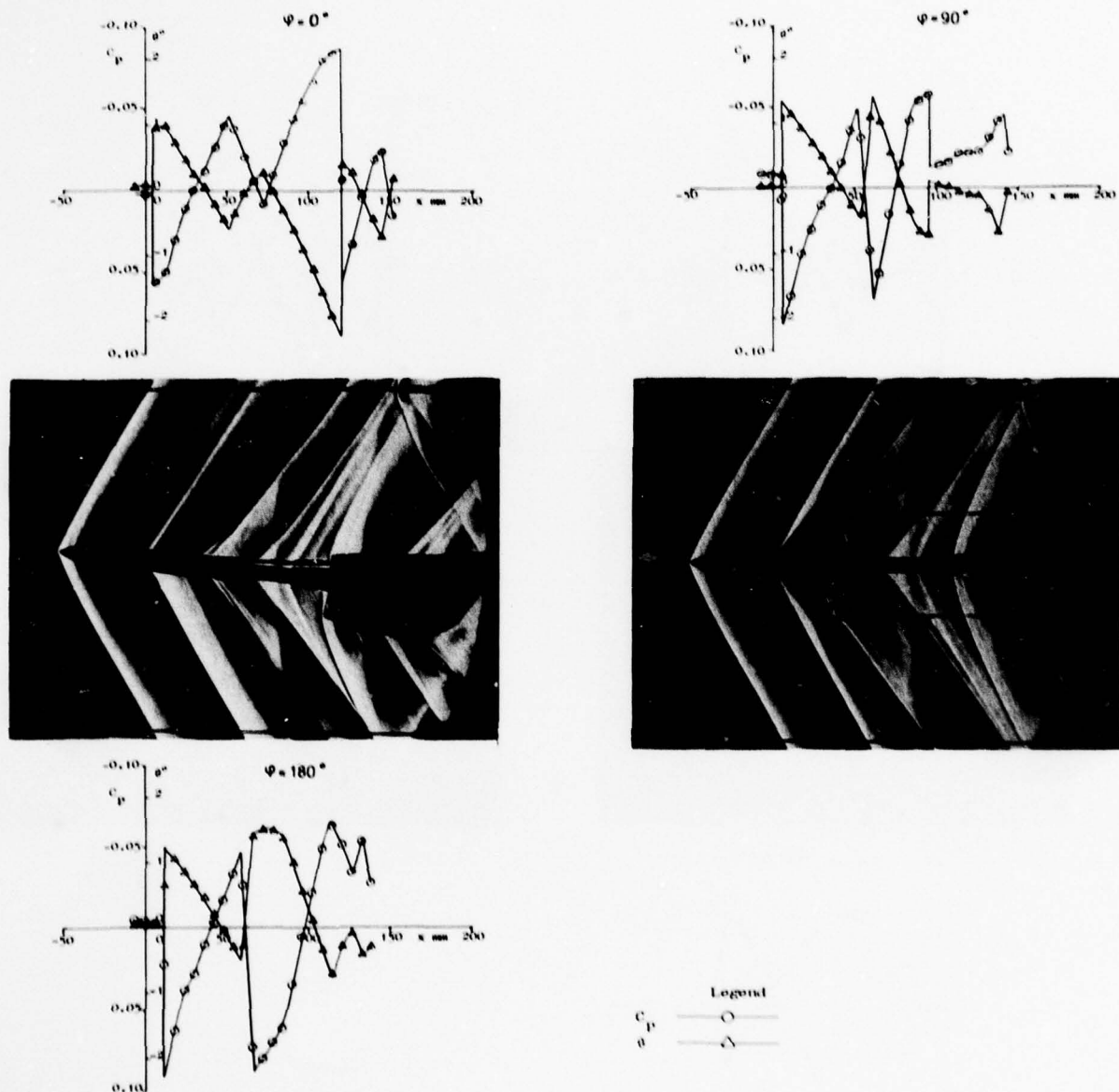


Figure 44. Experimental flow field

$M_\infty = 1.20$, $\alpha = 5.7^\circ$, $r = 103.2$ mm and $\varphi = 0^\circ, 90^\circ, 180^\circ$

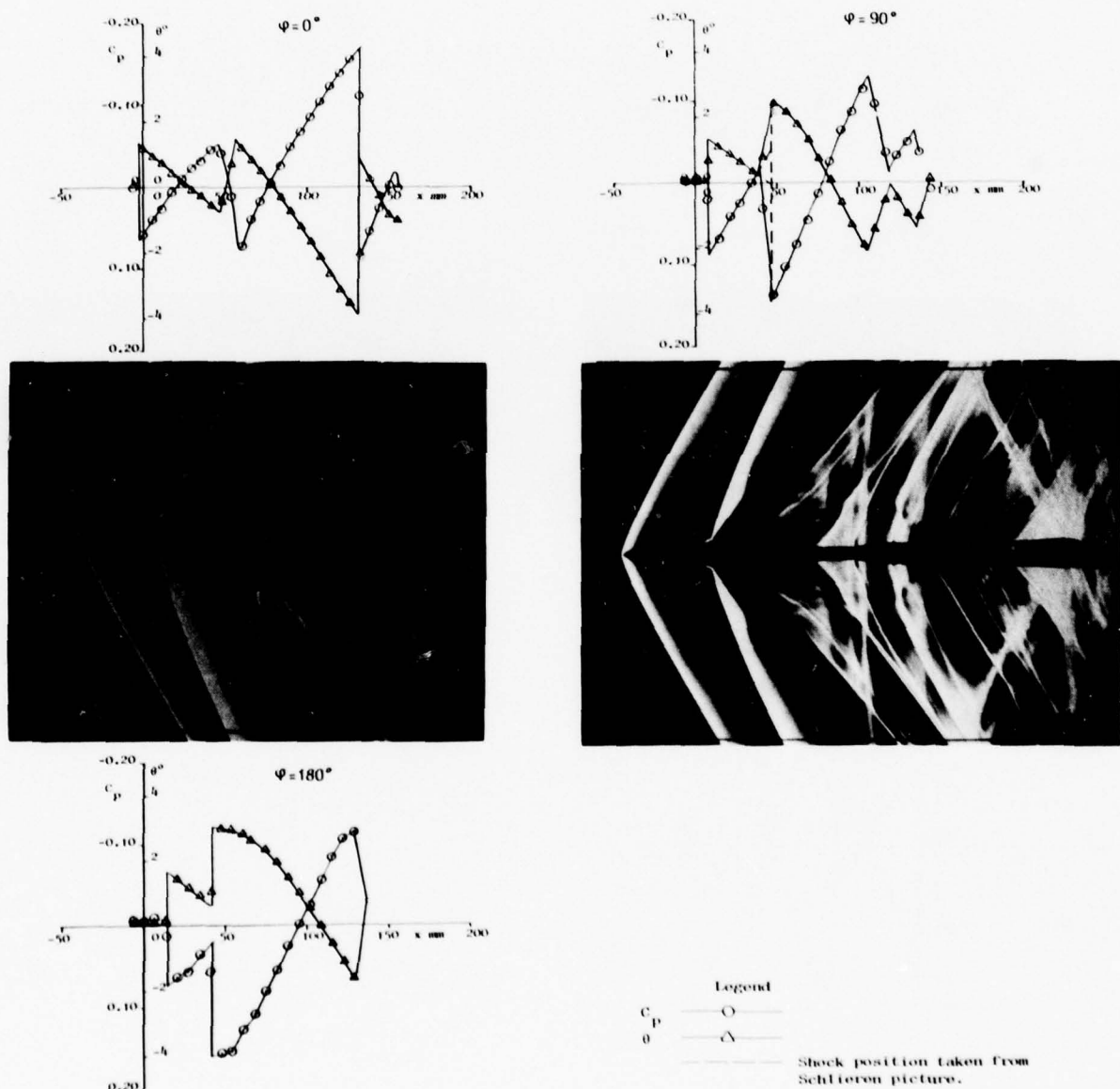


Figure 45. Experimental flow field

$M_\infty = 1.20$, $\alpha = 16.9^\circ$, $r = 103.2$ mm and $\varphi = 0^\circ, 90^\circ, 180^\circ$

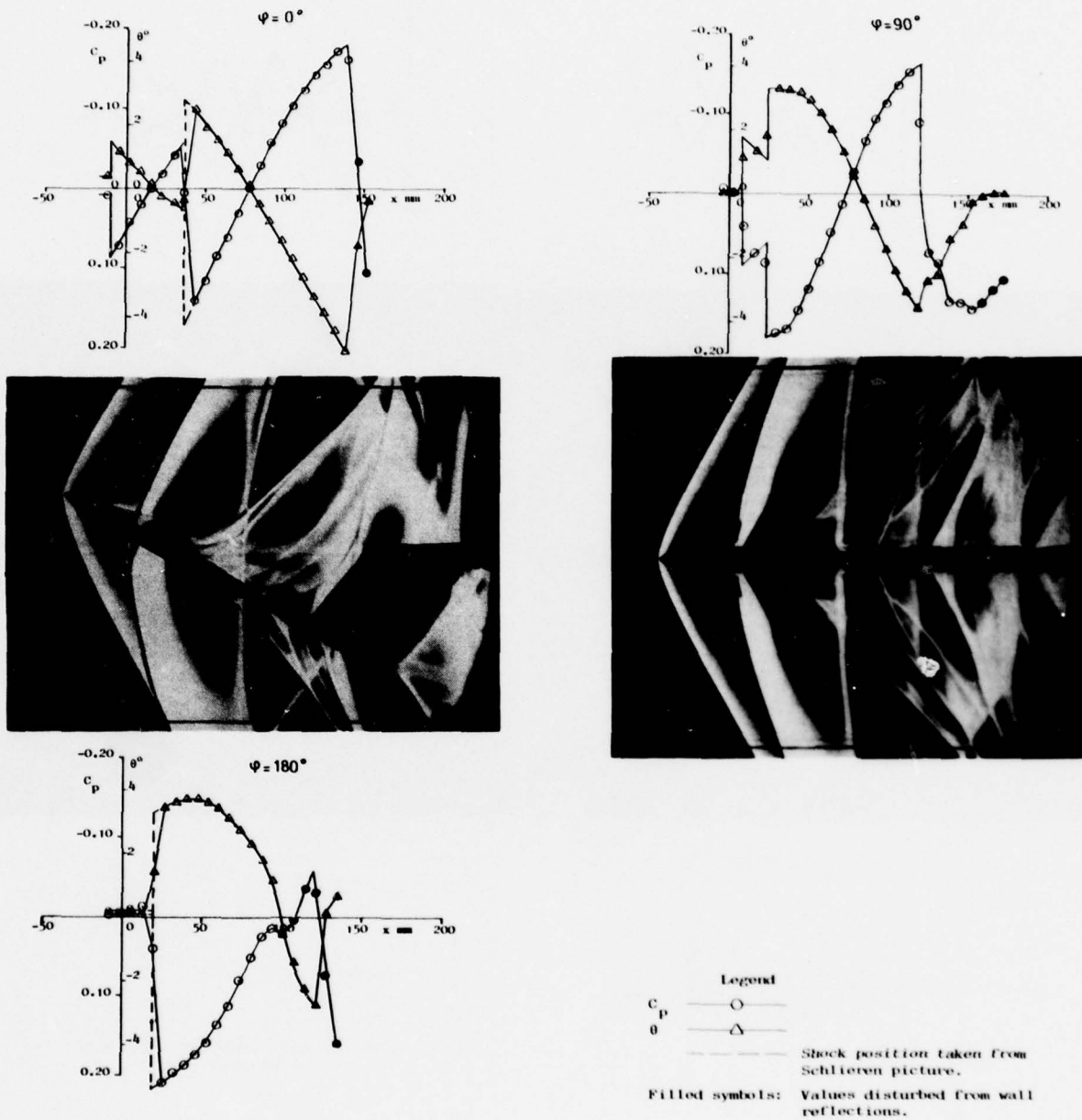


Figure 46. Experimental flow field

$$M_\infty = 1.20, \quad \alpha = 27.9^\circ, \quad r = 103.2 \text{ mm} \quad \text{and} \quad \varphi = 0^\circ, 90^\circ, 180^\circ$$

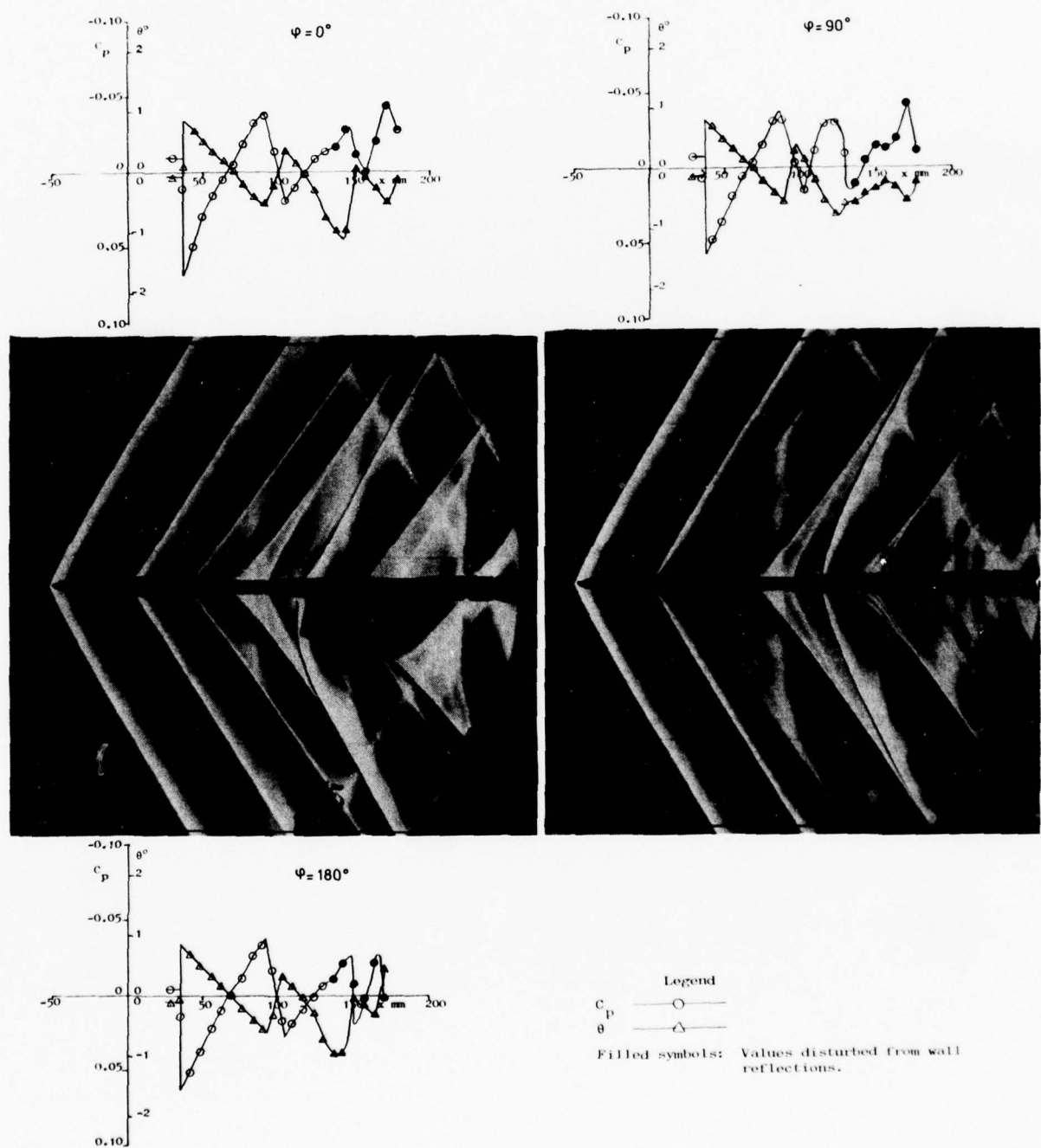


Figure 47. Experimental flow field

$M_\infty = 1.20$, $\alpha = 0^\circ$, $r = 153.2$ mm and $\varphi = 0^\circ, 90^\circ, 180^\circ$

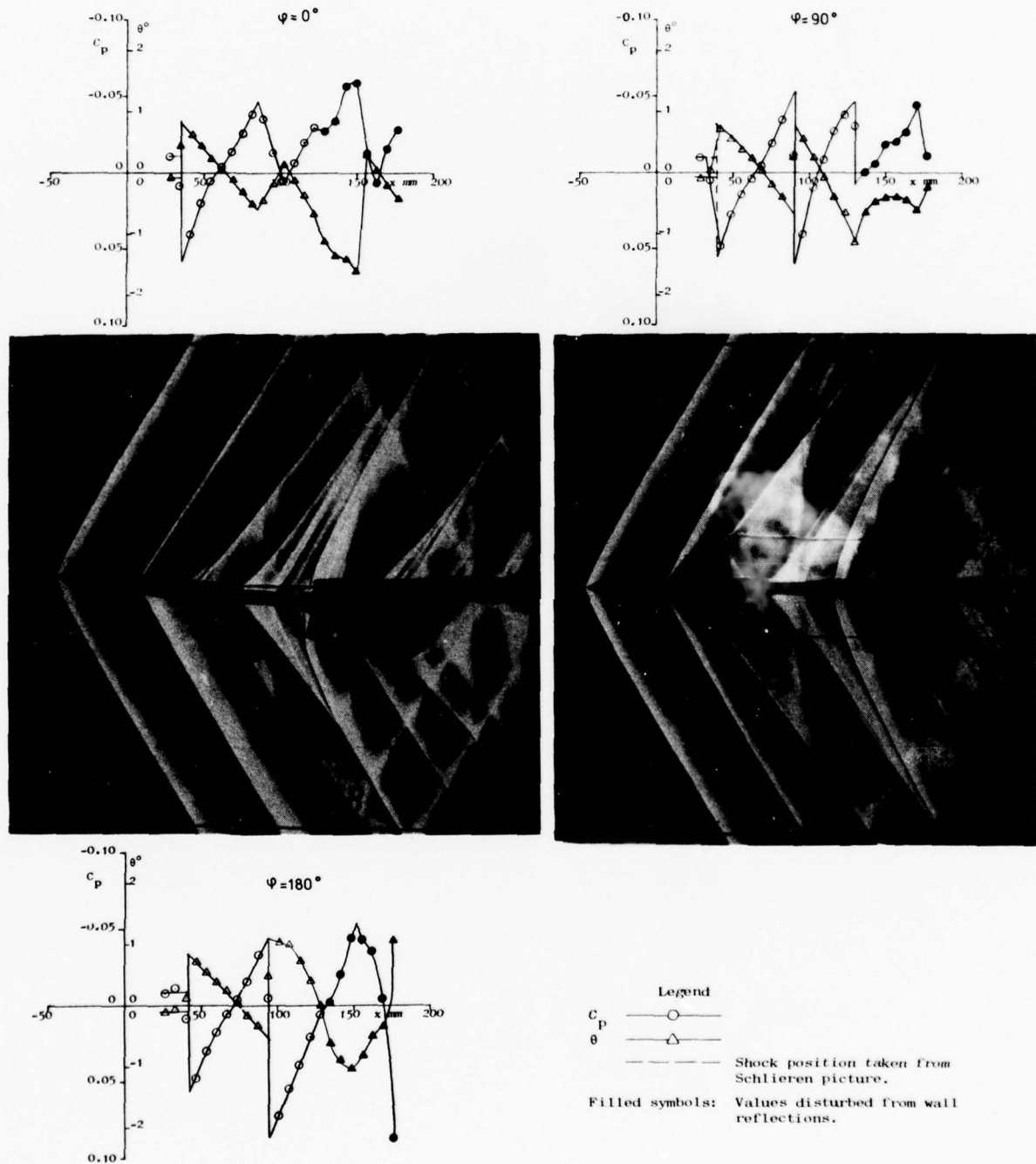


Figure 48. Experimental flow field

$$M_\infty = 1.20, \quad \alpha = 5.7^\circ, \quad r = 153.2 \text{ mm} \quad \text{and} \quad \varphi = 0^\circ, 90^\circ, 180^\circ$$

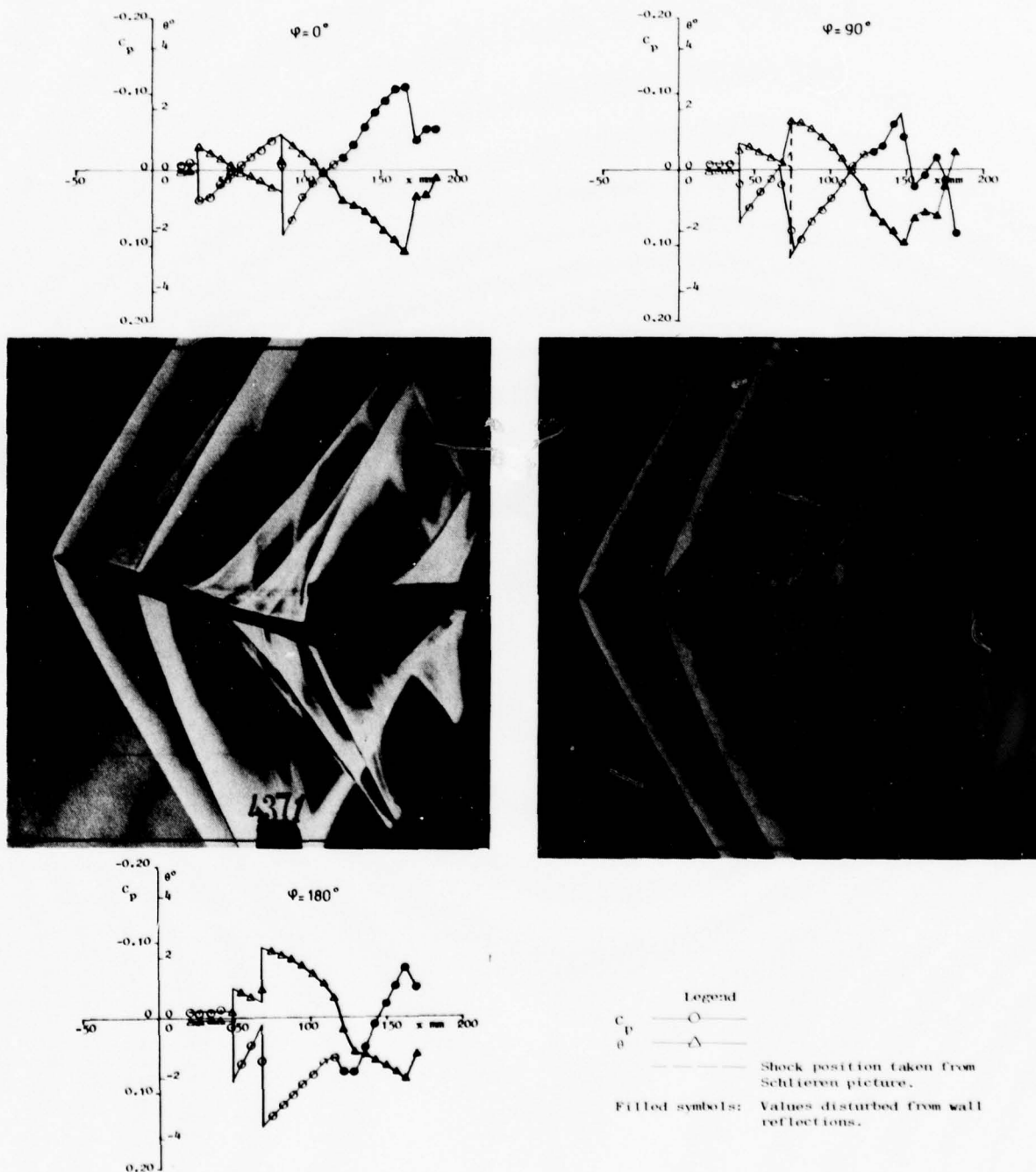


Figure 49. Experimental flow field

$M_\infty = 1.20$, $\alpha = 16.9^\circ$, $r = 153.2$ mm and $\phi = 0^\circ, 90^\circ, 180^\circ$

Figure 36. Experimental flow field

$M_\infty = 1.15$, $\alpha = 0^\circ$, $r = 102.6$ mm and $\varphi = 0^\circ, 90^\circ, 180^\circ$

75

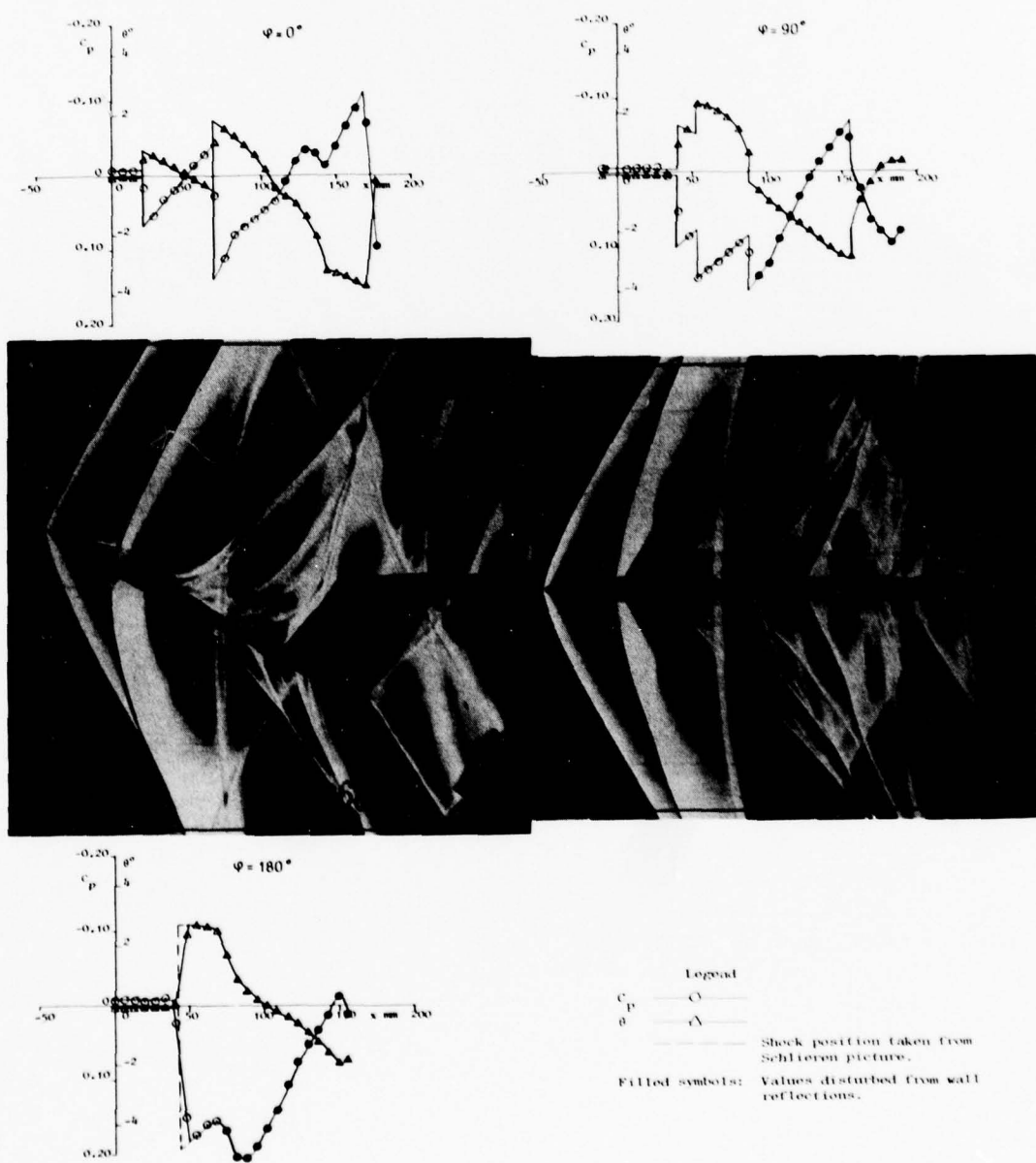


Figure 50. Experimental flow field

$M_\infty = 1.20$, $\alpha = 27.9^\circ$, $r = 153.2$ mm and $\varphi = 0^\circ, 90^\circ, 180^\circ$

Figure 37. Experimental flow field

$M_{\infty} = 1.15$, $\alpha = 5.7^\circ$, $r = 102.6 \text{ mm}$ and $\varphi = 0^\circ, 90^\circ, 180^\circ$

76

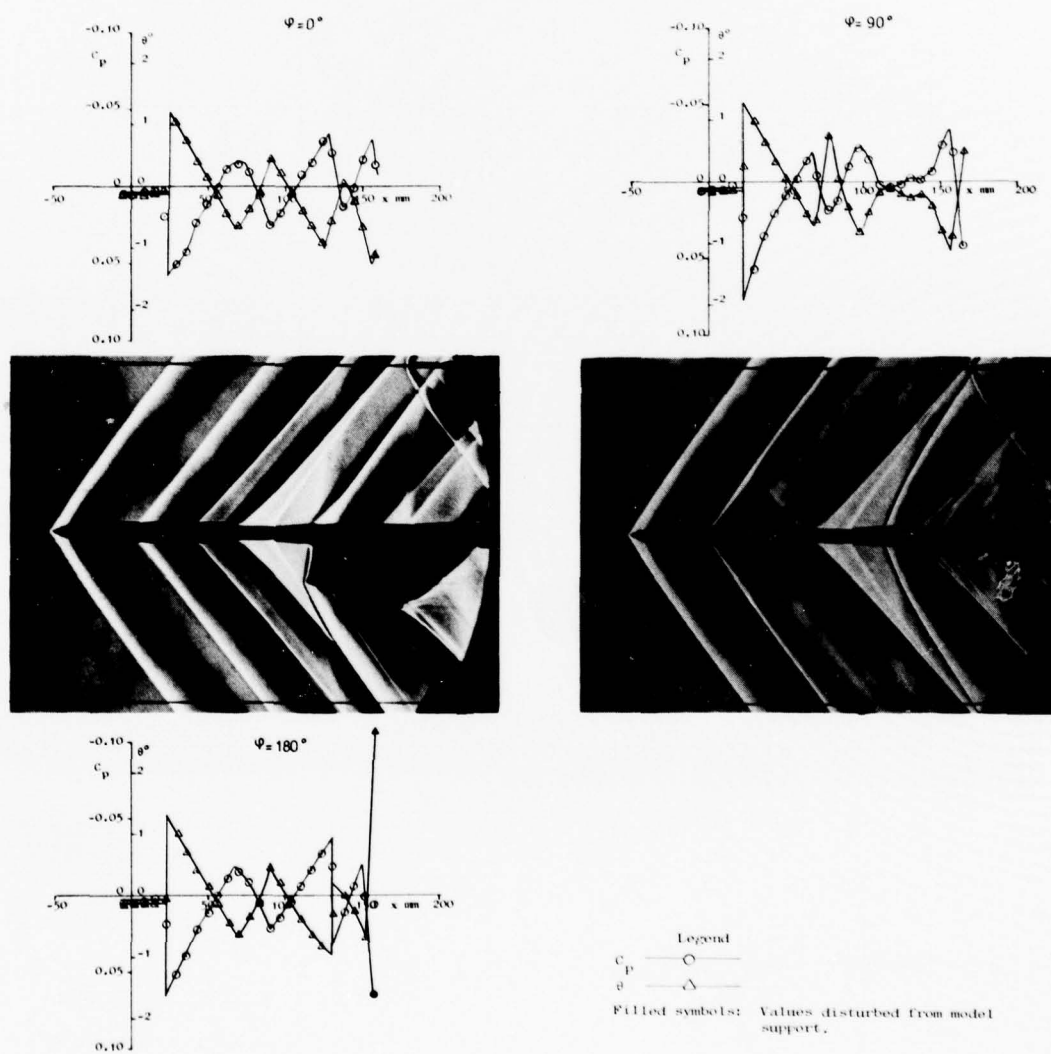


Figure 51. Experimental flow field

$M_{\infty} = 1.30$, $\alpha = 0^\circ$, $r = 105.3 \text{ mm}$ and $\varphi = 0^\circ, 90^\circ, 180^\circ$

Legend
 c_p —○—
 θ —△—
 Filled symbols: Values disturbed from model support.

Figure 50. Experimental flow field

$$M_{\infty} = 1.15, \quad \alpha = 16.8^\circ, \quad r = 102.6 \text{ mm} \quad \text{and} \quad \varphi = 0^\circ, 90^\circ, 180^\circ$$

77

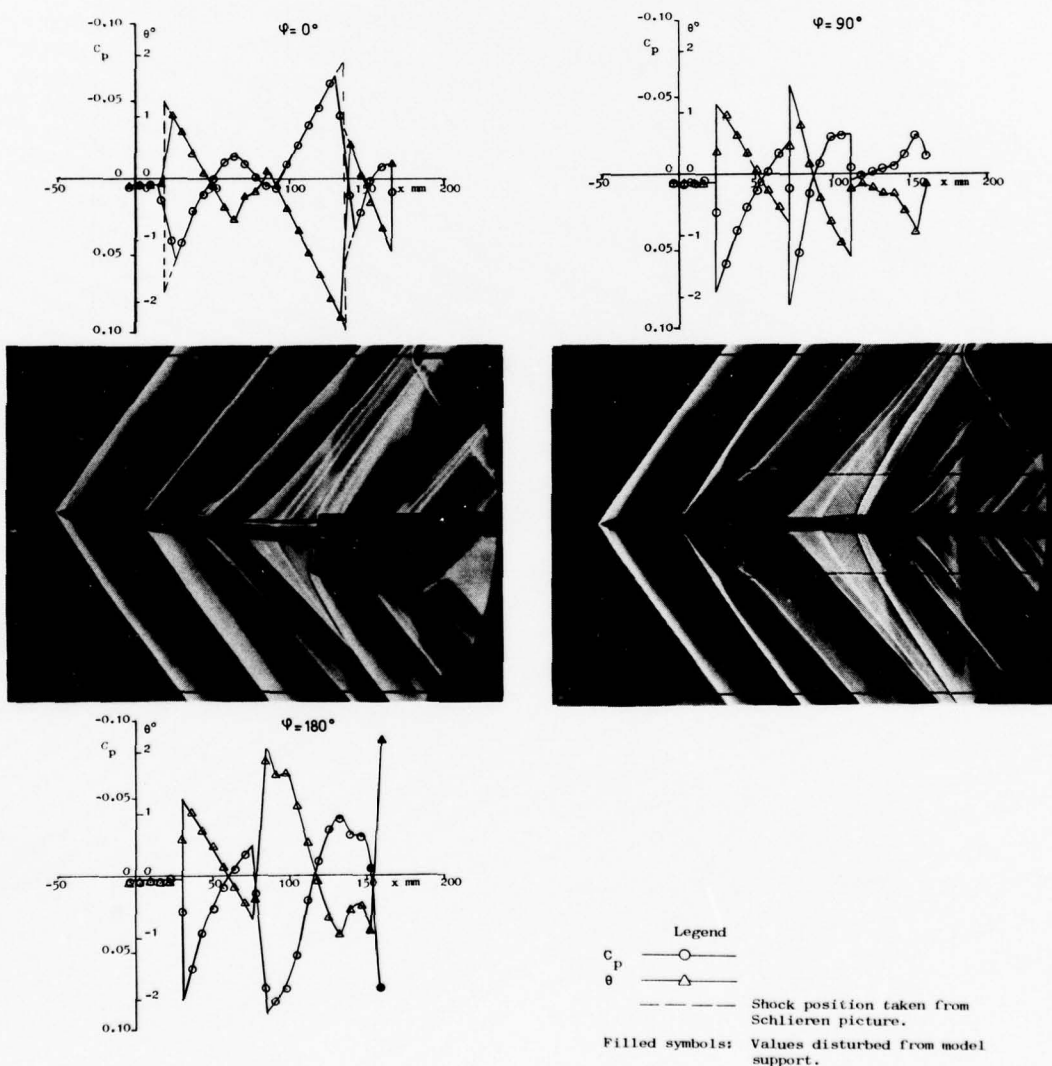


Figure 52. Experimental flow field

$$M_{\infty} = 1.30, \quad \alpha = 5.7^\circ, \quad r = 105.3 \text{ mm} \quad \text{and} \quad \varphi = 0^\circ, 90^\circ, 180^\circ$$

Figure 39. Experimental flow field
 $M_{\infty} = 1.20$, $\alpha = 0^{\circ}$, $r = 73.2 \text{ mm}$ and $\varphi = 0^{\circ}, 90^{\circ}, 180^{\circ}$

78

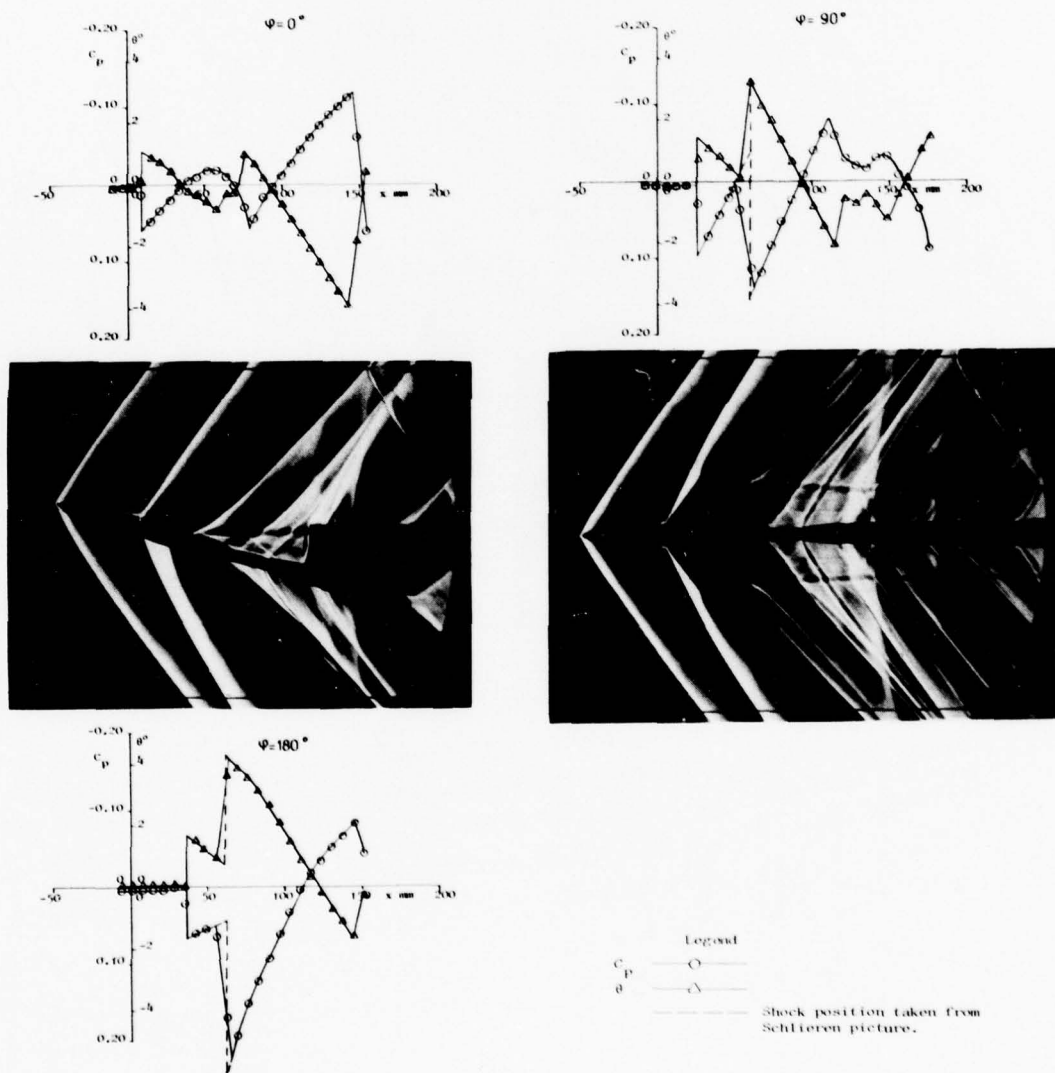


Figure 53. Experimental flow field
 $M_{\infty} = 1.30$, $\alpha = 17.1^{\circ}$, $r = 105.3 \text{ mm}$ and $\varphi = 0^{\circ}, 90^{\circ}, 180^{\circ}$

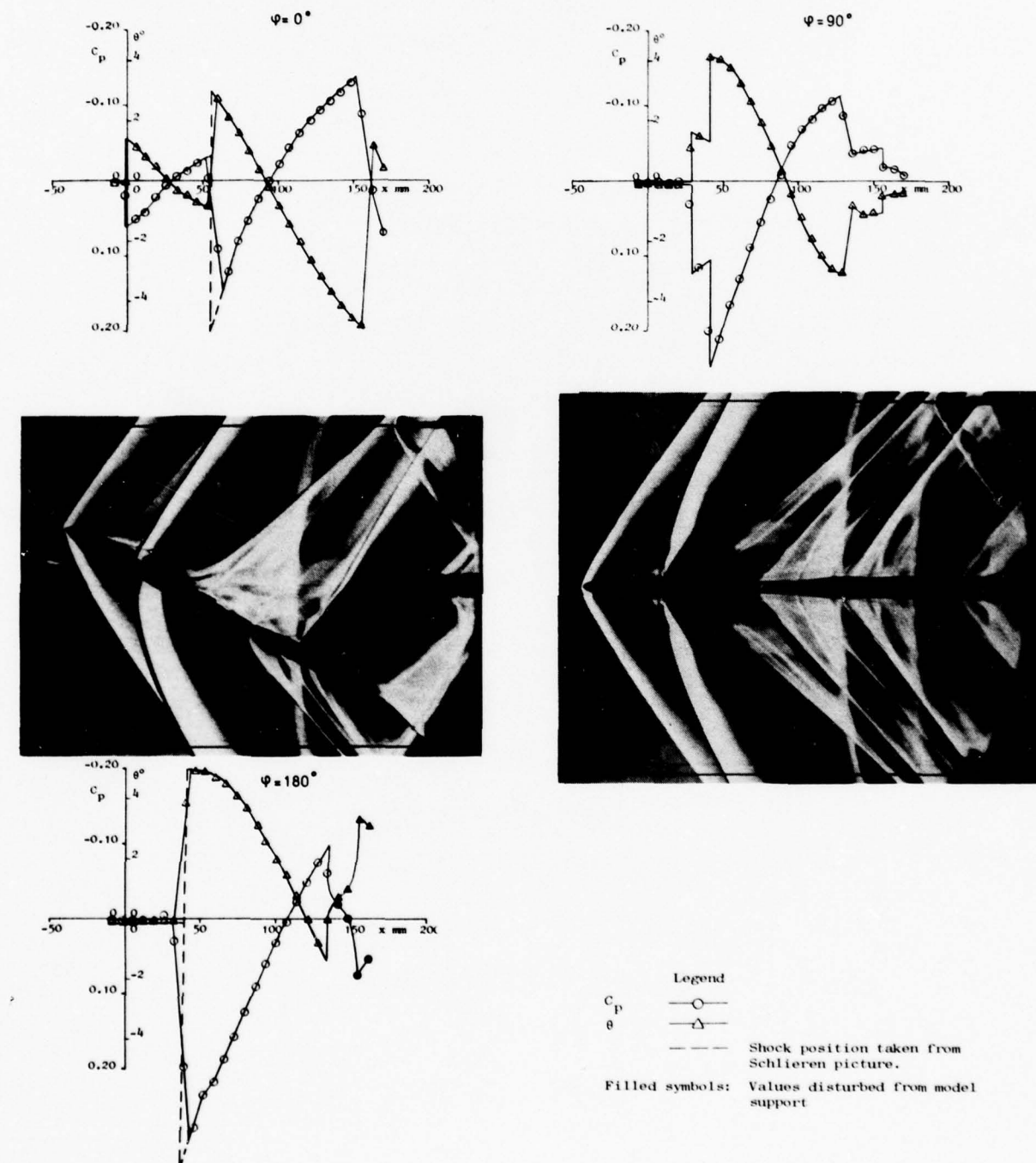


Figure 54. Experimental flow field

$$M_\infty = 1.30, \quad \alpha = 28.3^\circ, \quad r = 105.3 \text{ mm} \quad \text{and} \quad \varphi = 0^\circ, 90^\circ, 180^\circ$$

A P P E N D I X 2

Figures 55 - 73

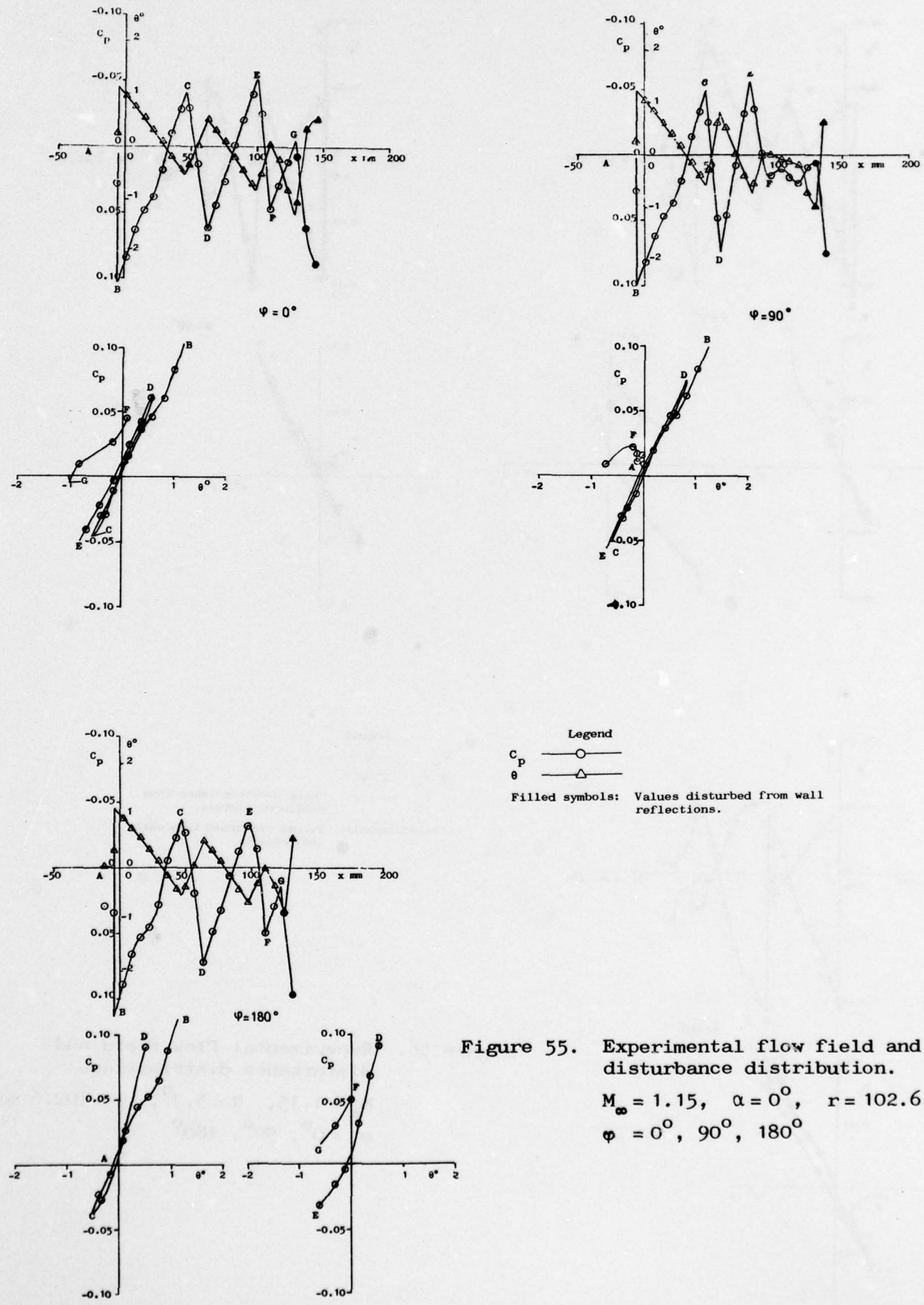


Figure 55. Experimental flow field and disturbance distribution.

$M_\infty = 1.15$, $\alpha = 0^\circ$, $r = 102.6$ mm
 $\psi = 0^\circ, 90^\circ, 180^\circ$

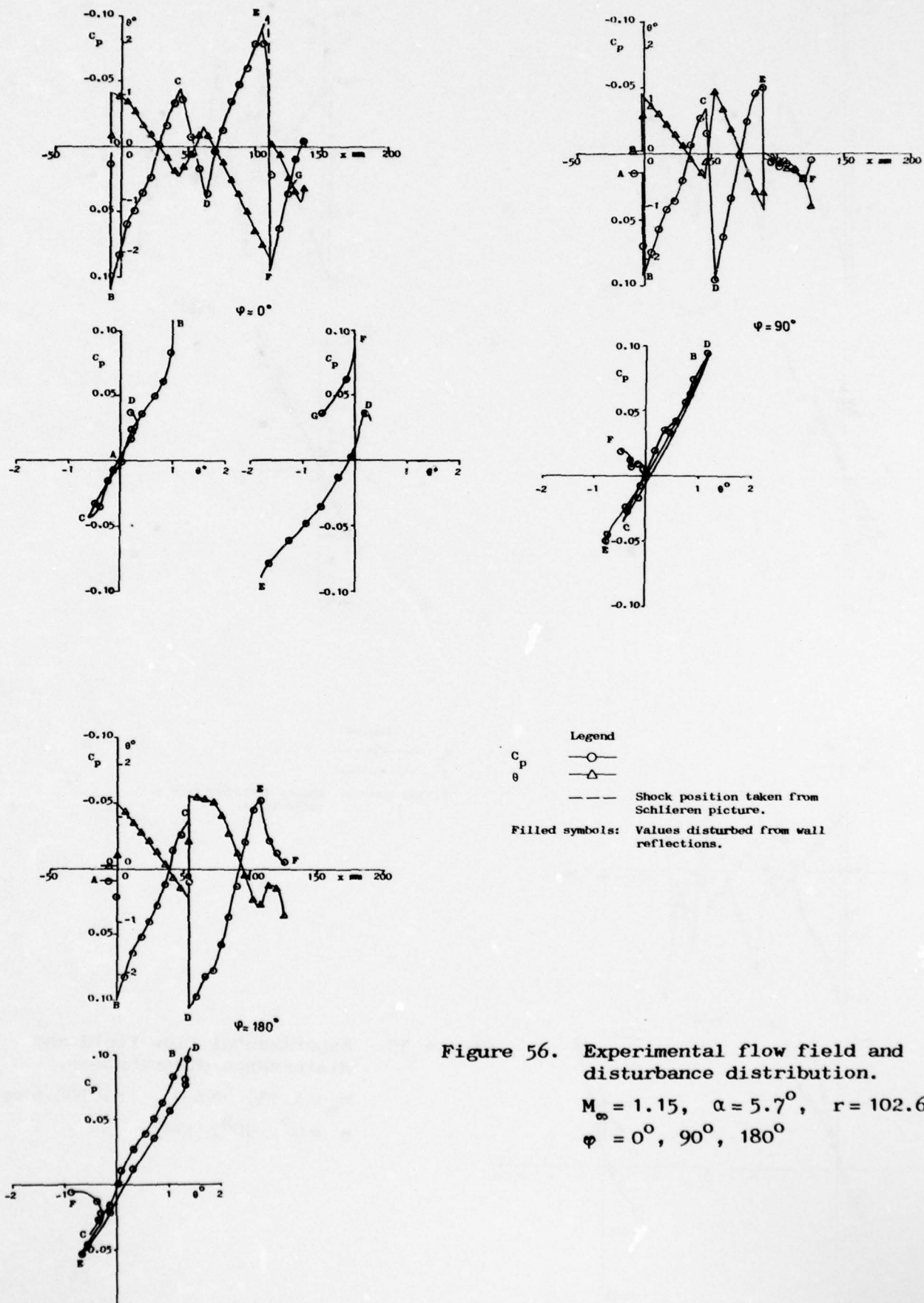


Figure 56. Experimental flow field and disturbance distribution.

$M_\infty = 1.15$, $\alpha = 5.7^\circ$, $r = 102.6 \text{ mm}$
 $\phi = 0^\circ, 90^\circ, 180^\circ$

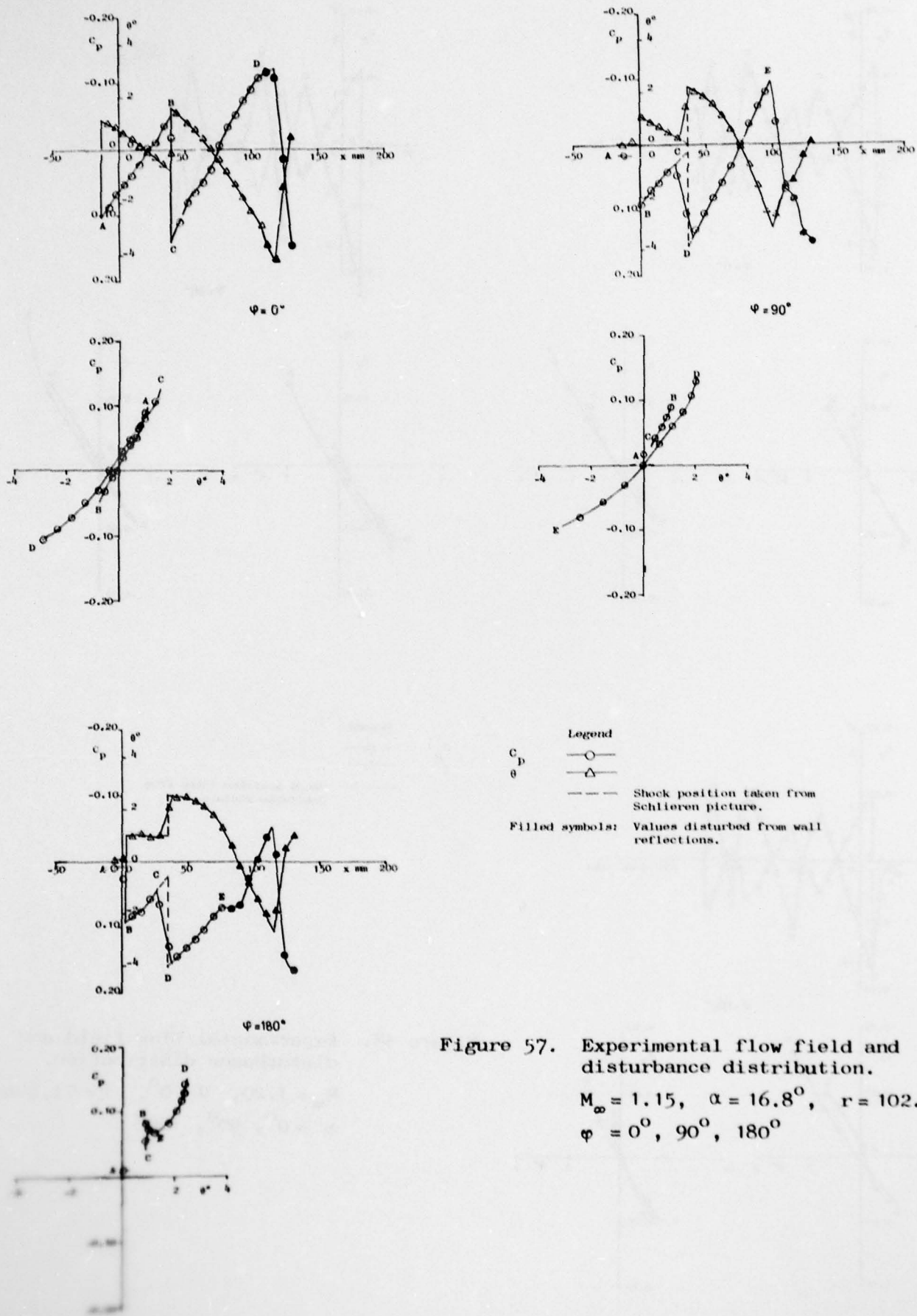


Figure 57. Experimental flow field and disturbance distribution.

$M_\infty = 1.15$, $\alpha = 16.8^\circ$, $r = 102.6$ mm
 $\phi = 0^\circ, 90^\circ, 180^\circ$

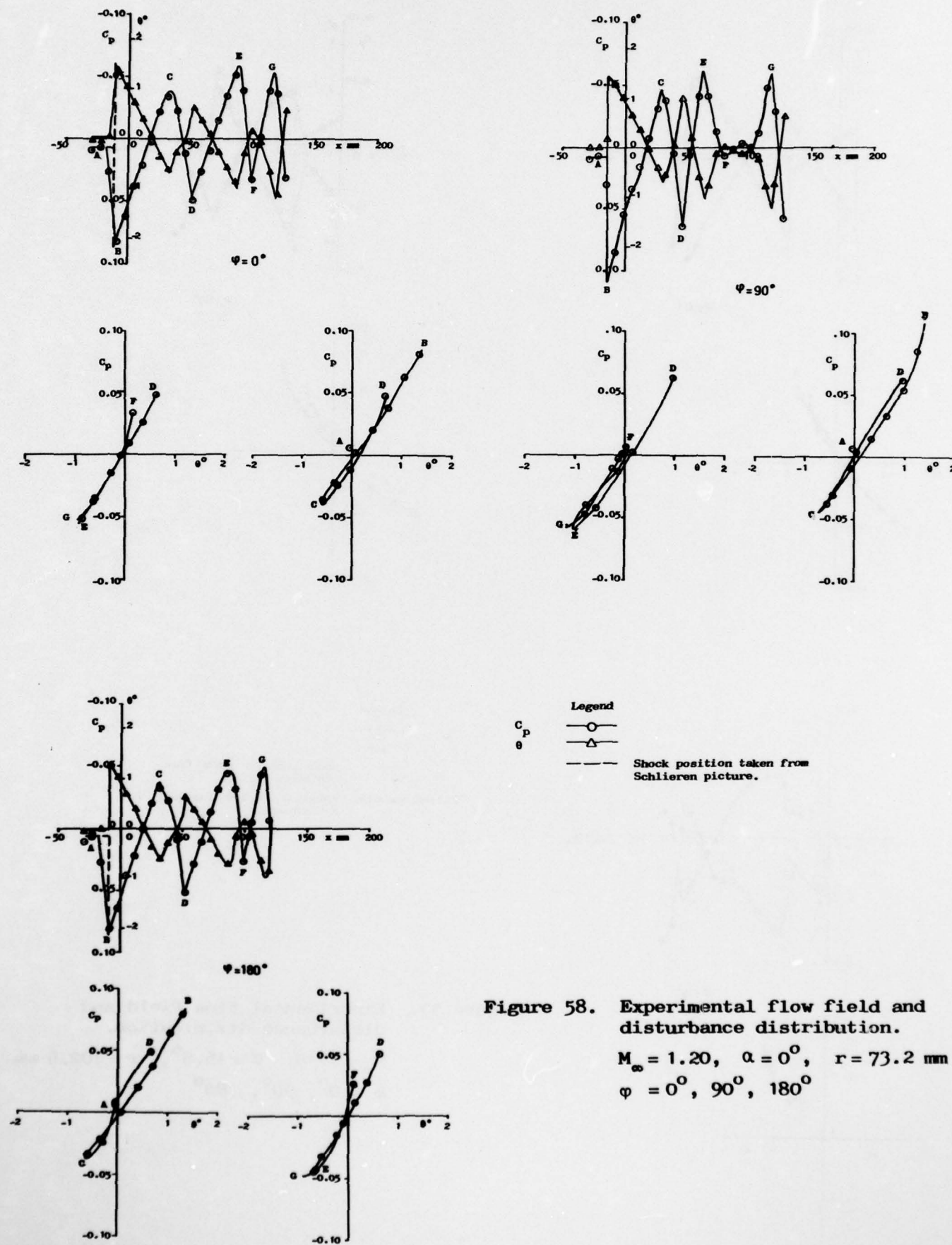
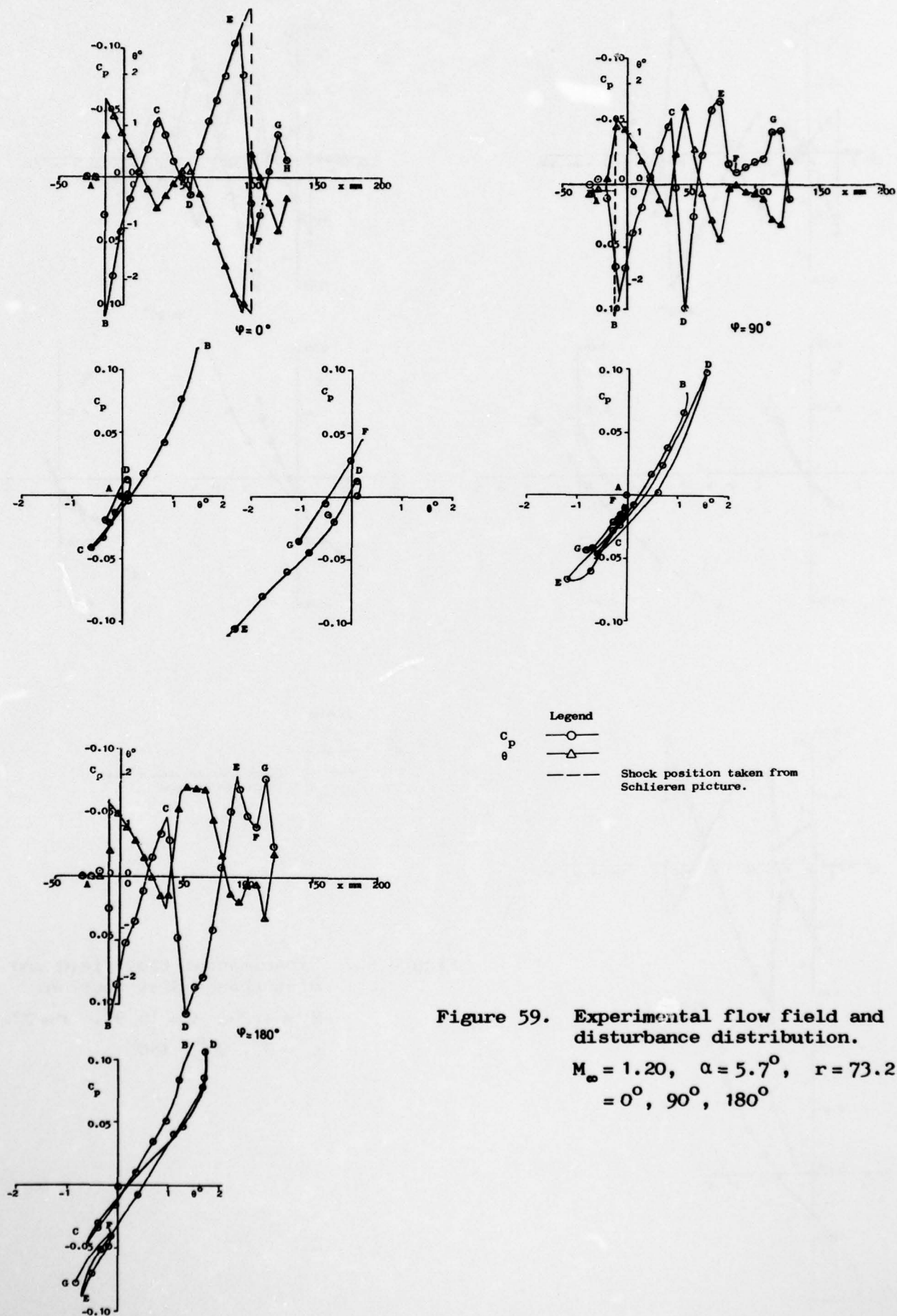
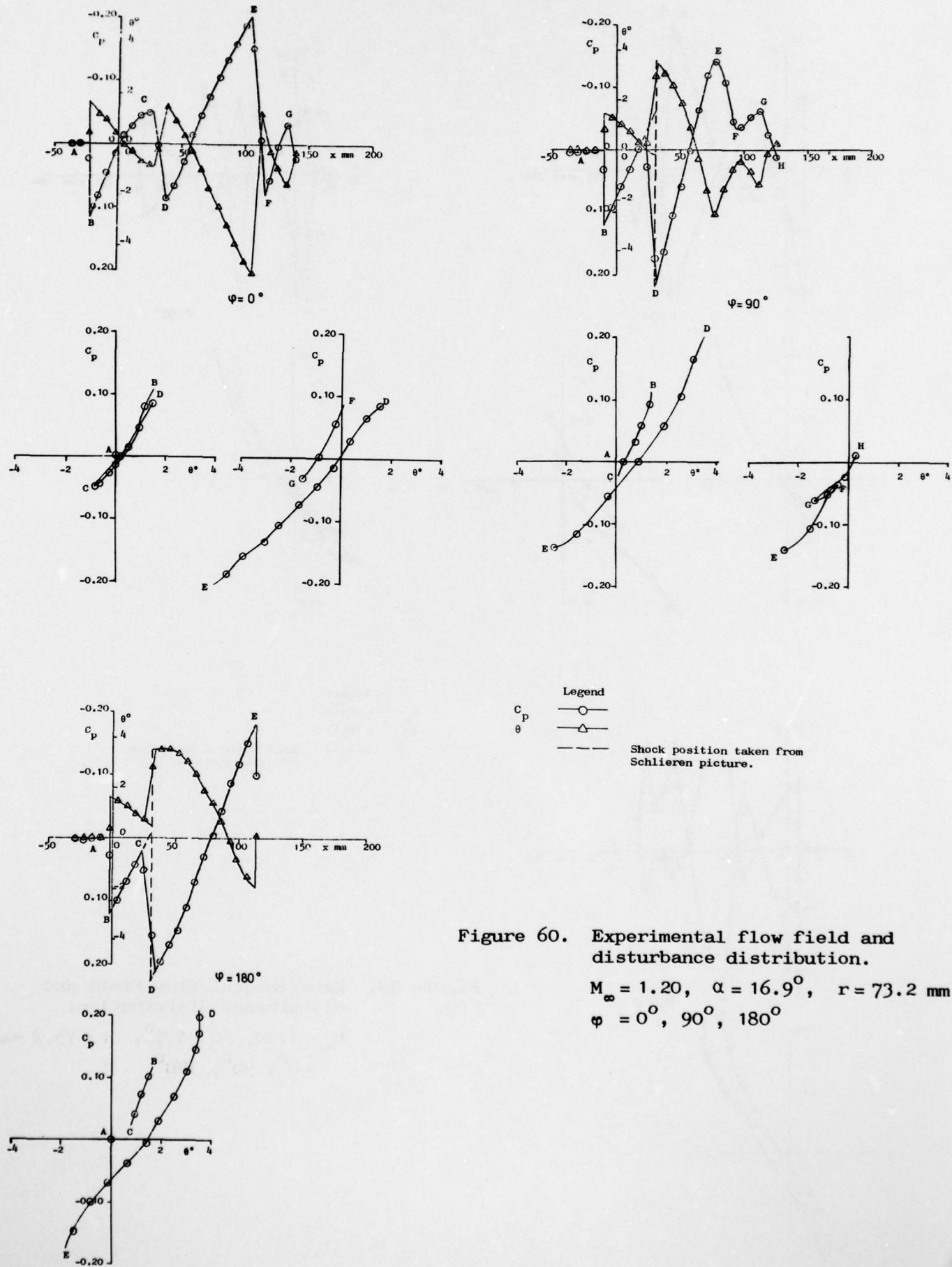


Figure 58. Experimental flow field and disturbance distribution.

$M_\infty = 1.20$, $\alpha = 0^\circ$, $r = 73.2$ mm
 $\varphi = 0^\circ, 90^\circ, 180^\circ$





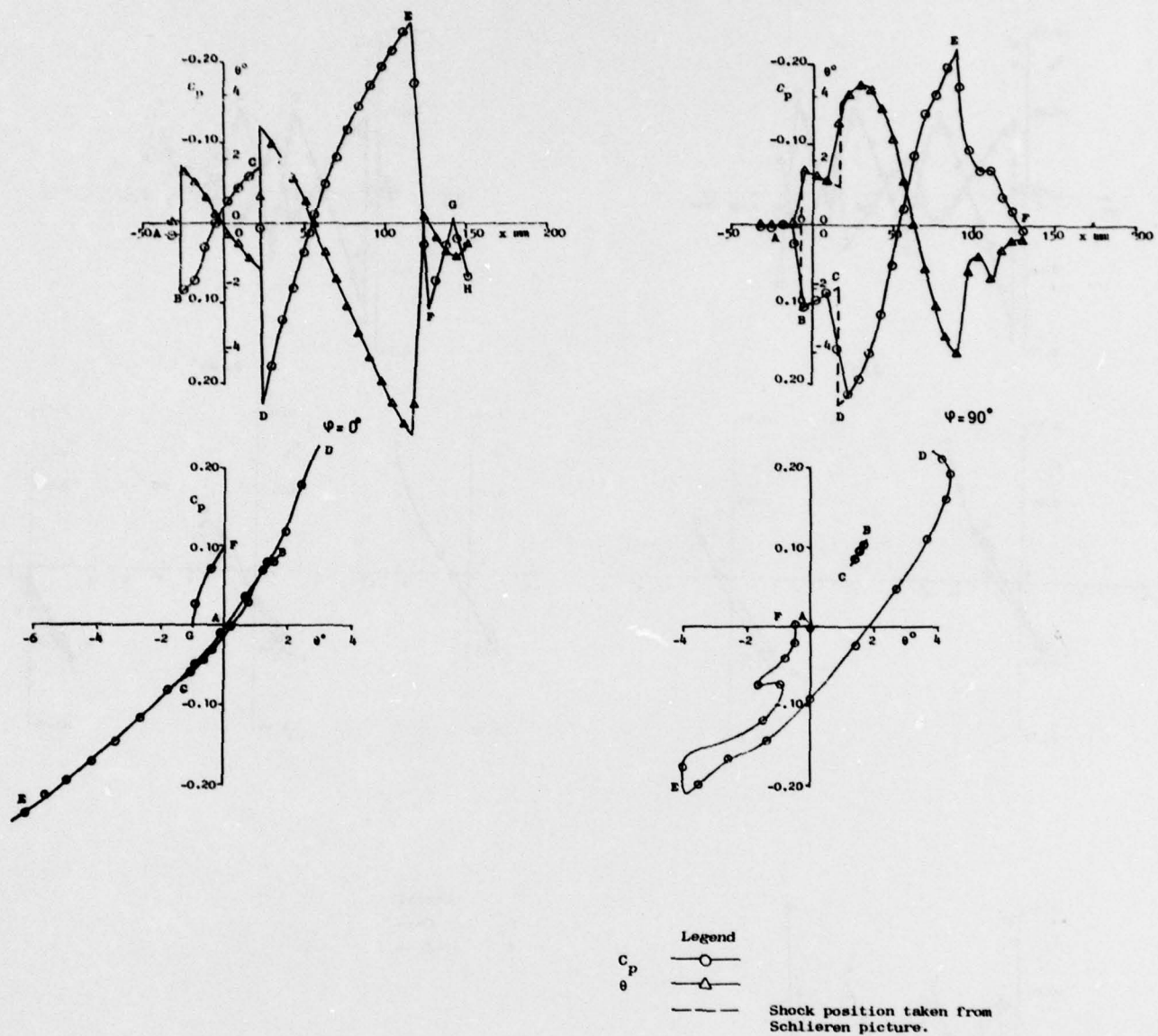


Figure 61. Experimental flow field and disturbance distribution.

$$M_\infty = 1.20, \quad \alpha = 27.9^\circ, \quad r = 73.2 \text{ mm}$$

$$\varphi = 0^\circ, 90^\circ, 180^\circ$$

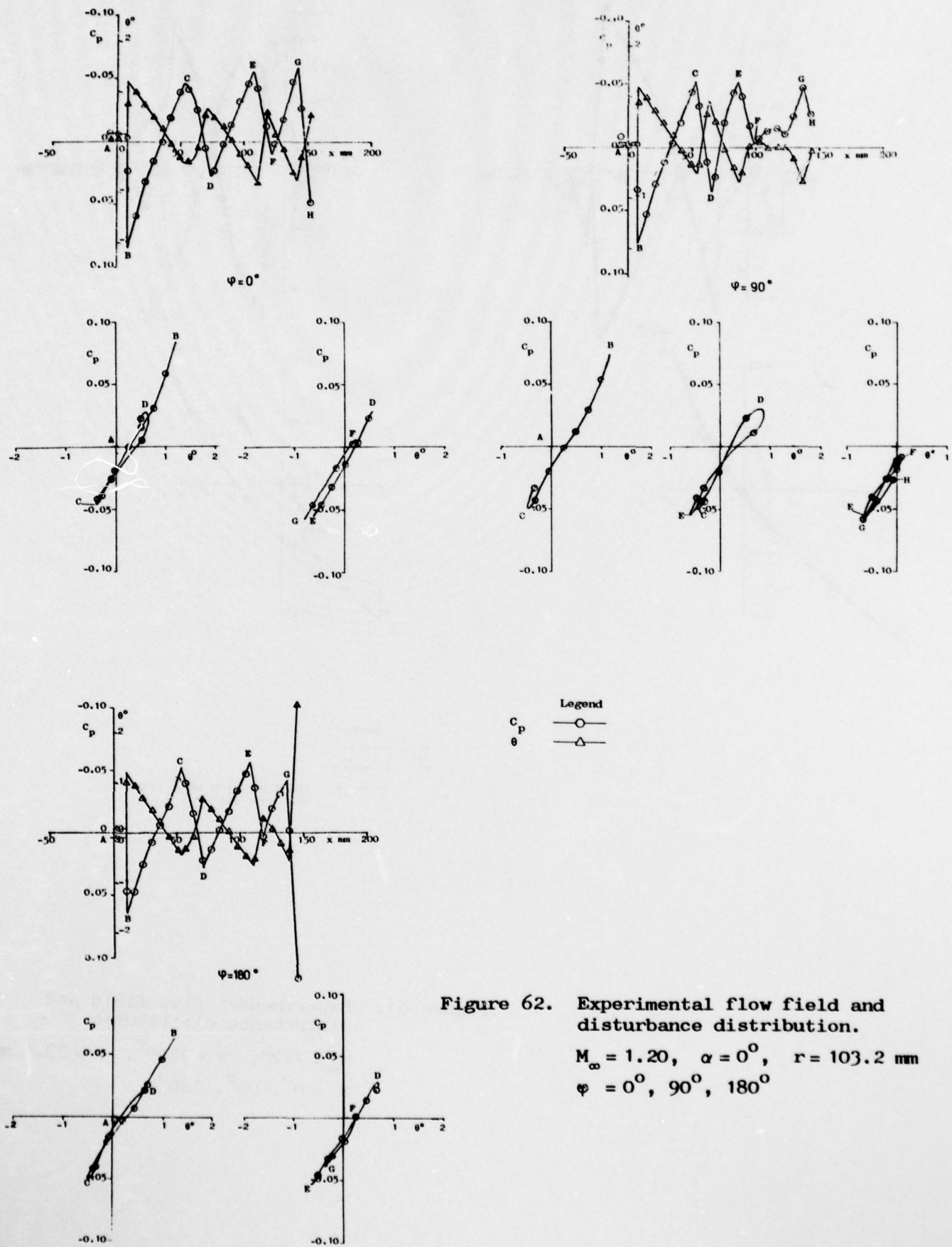


Figure 62. Experimental flow field and disturbance distribution.

$M_\infty = 1.20$, $\alpha = 0^\circ$, $r = 103.2$ mm
 $\phi = 0^\circ, 90^\circ, 180^\circ$

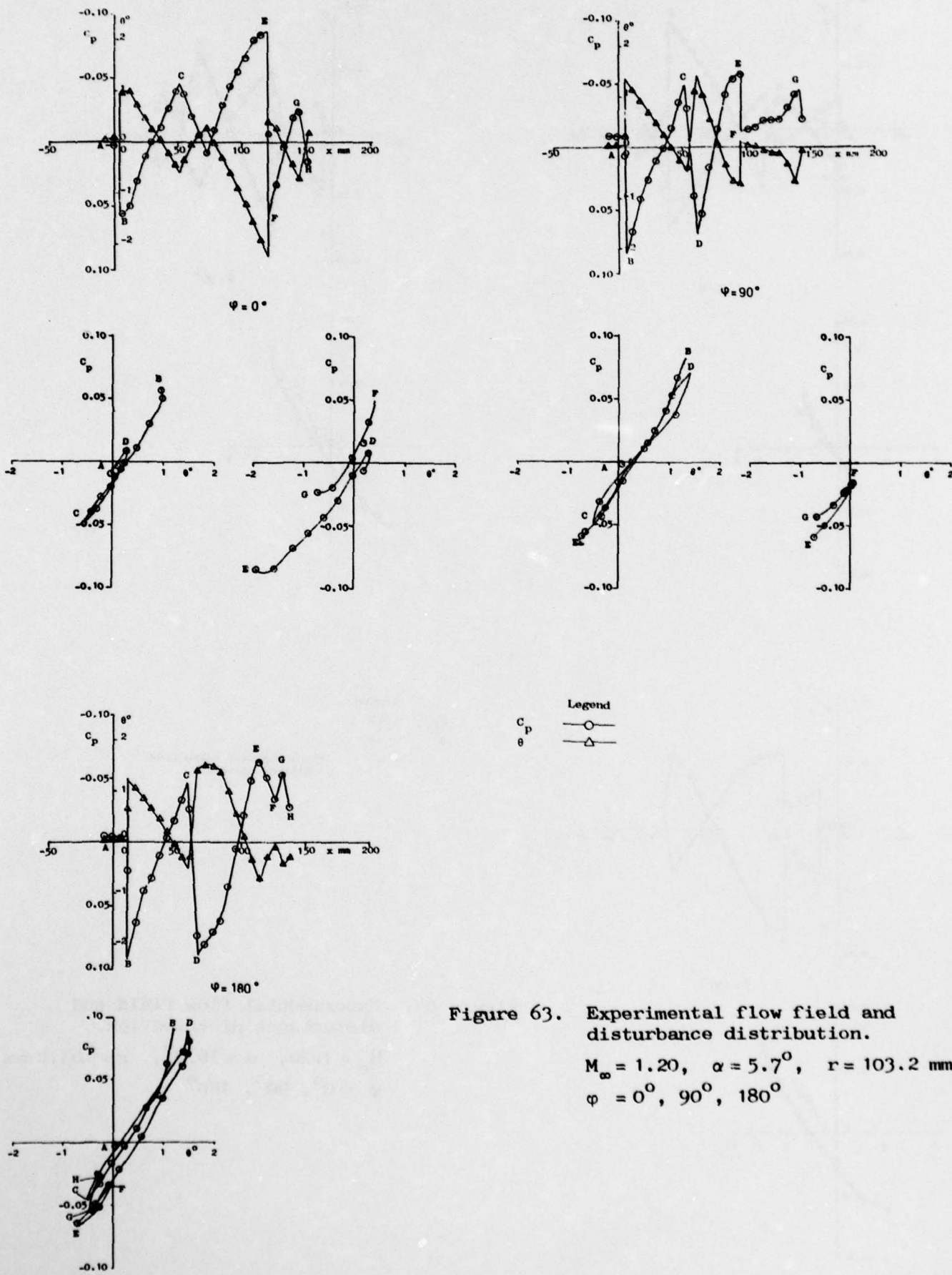


Figure 63. Experimental flow field and disturbance distribution.

$M_\infty = 1.20$, $\alpha = 5.7^\circ$, $r = 103.2 \text{ mm}$
 $\phi = 0^\circ, 90^\circ, 180^\circ$

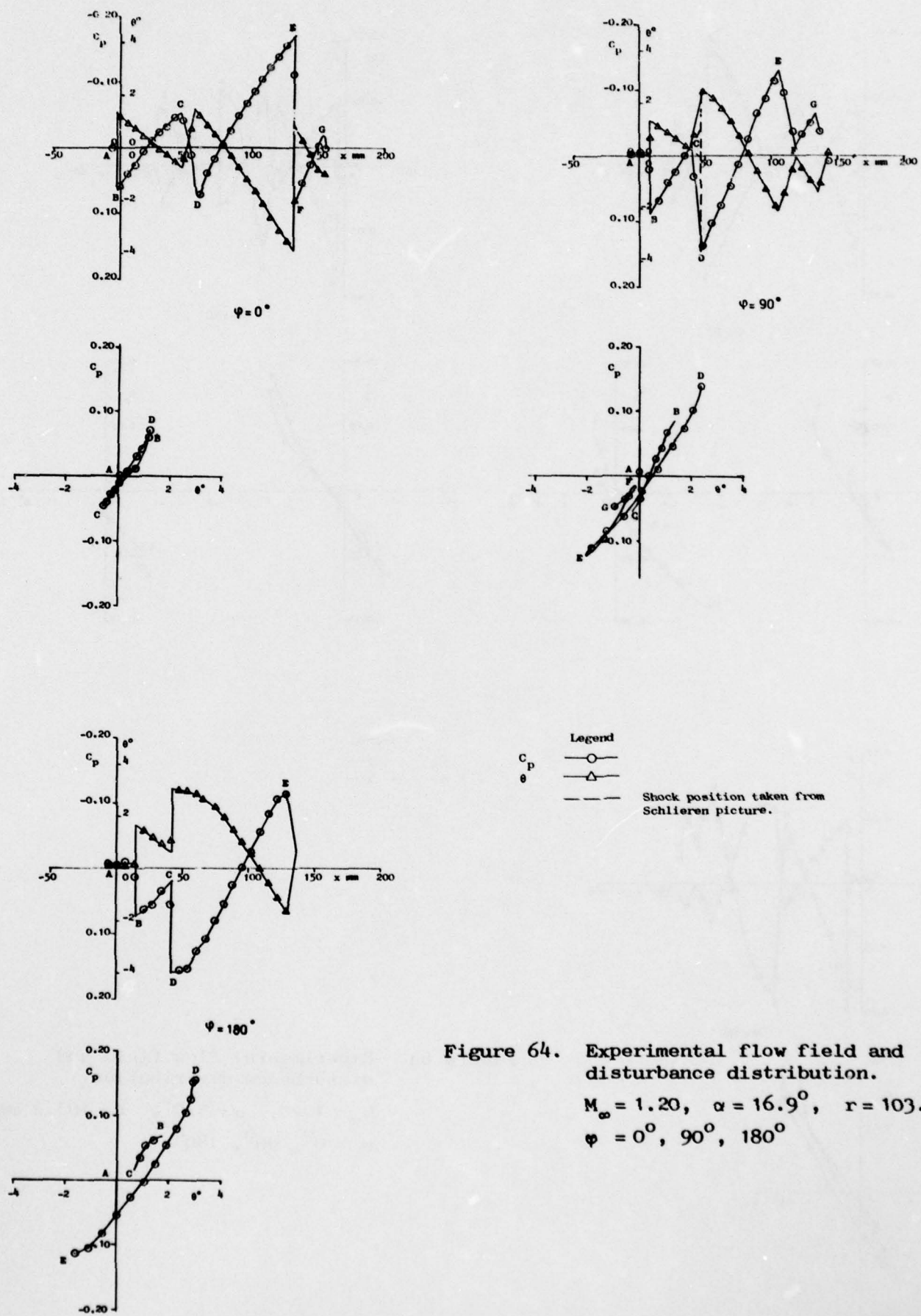


Figure 64. Experimental flow field and disturbance distribution.

$M_\infty = 1.20$, $\alpha = 16.9^\circ$, $r = 103.2$ mm
 $\psi = 0^\circ, 90^\circ, 180^\circ$

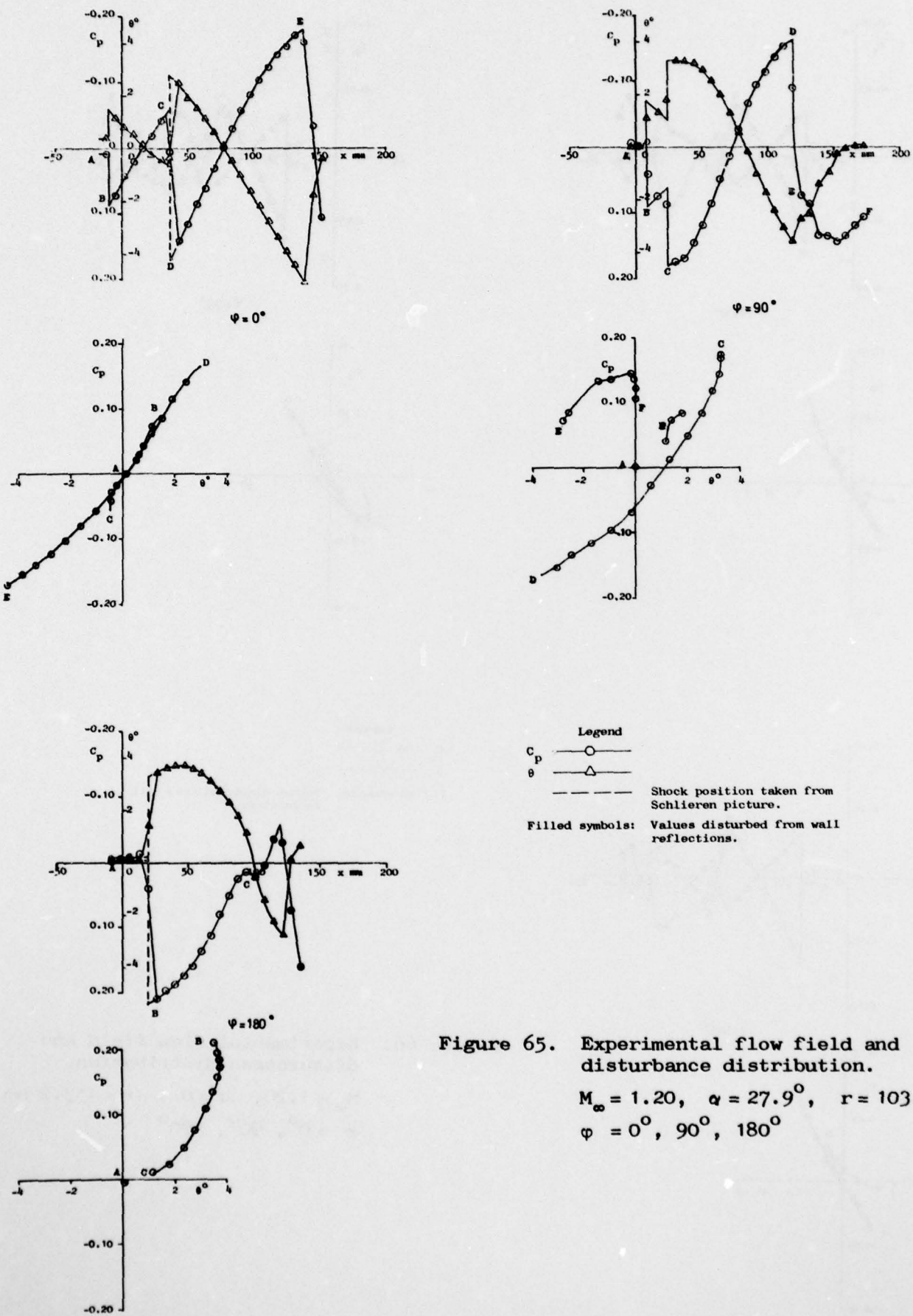


Figure 65. Experimental flow field and disturbance distribution.

$M_\infty = 1.20$, $\alpha = 27.9^\circ$, $r = 103.2 \text{ mm}$
 $\phi = 0^\circ, 90^\circ, 180^\circ$

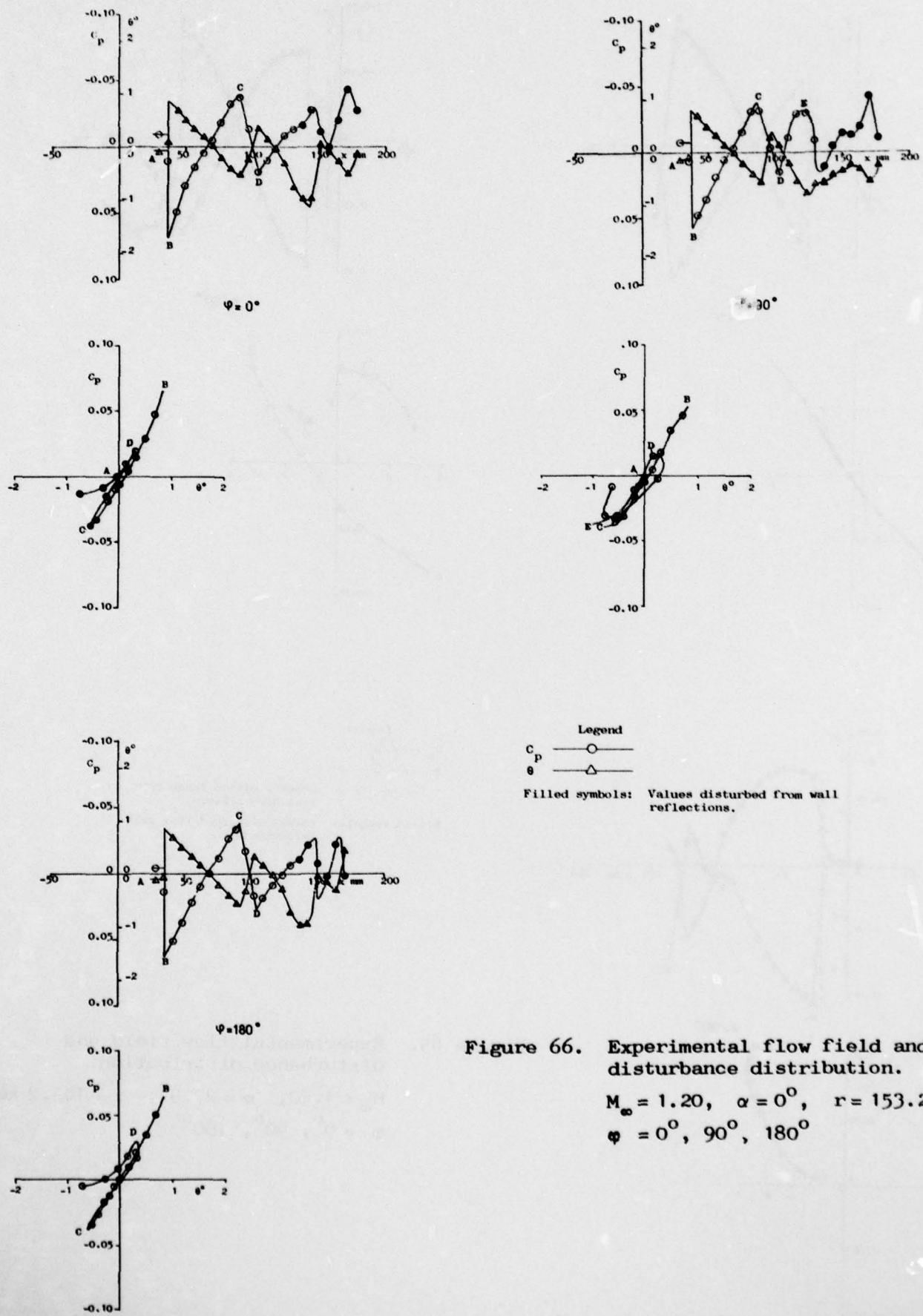


Figure 66. Experimental flow field and disturbance distribution.

$M_\infty = 1.20$, $\alpha = 0^\circ$, $r = 153.2$ mm
 $\varphi = 0^\circ, 90^\circ, 180^\circ$

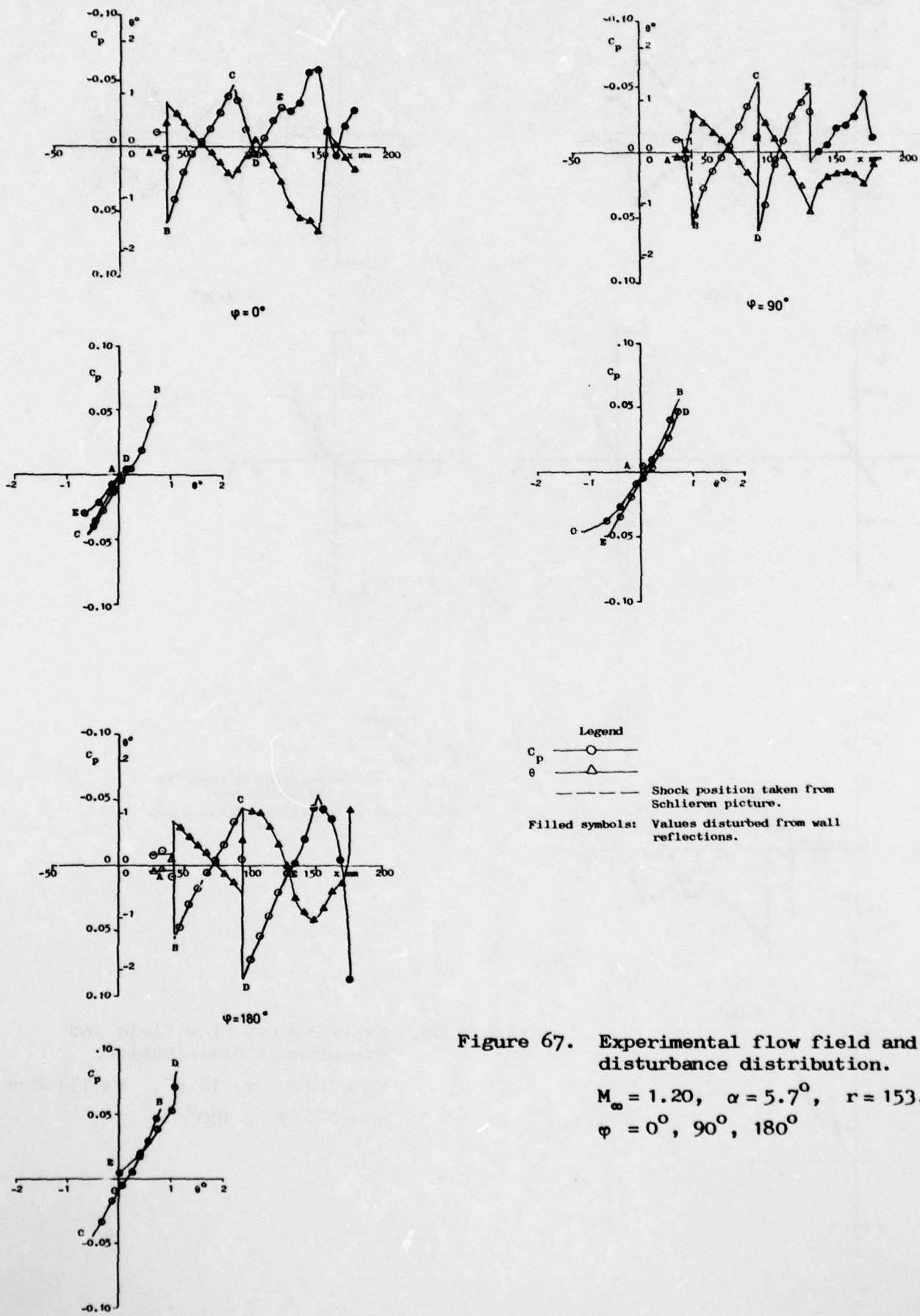


Figure 67. Experimental flow field and disturbance distribution.

$M_\infty = 1.20$, $\alpha = 5.7^\circ$, $r = 153.2$ mm
 $\varphi = 0^\circ, 90^\circ, 180^\circ$

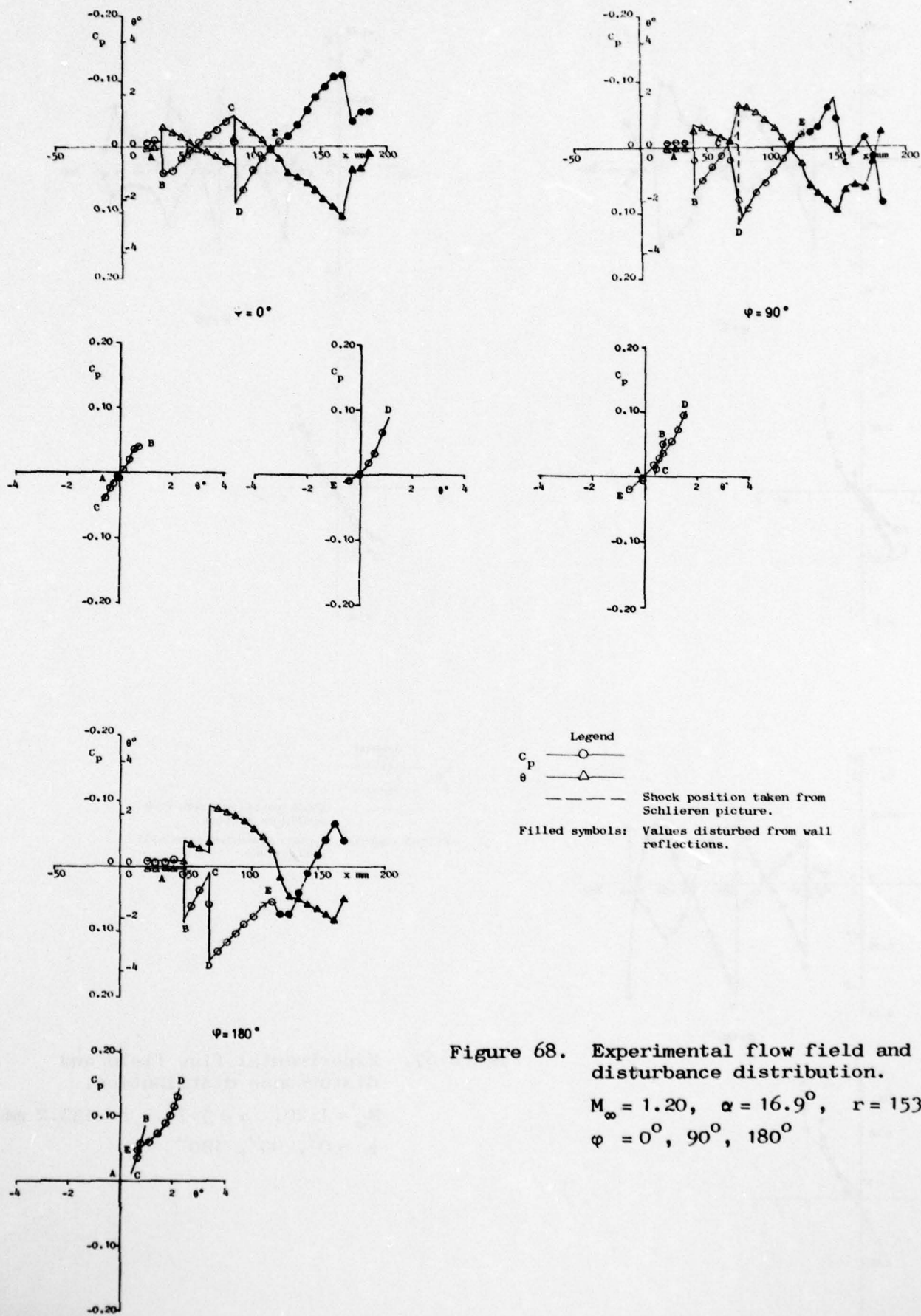


Figure 68. Experimental flow field and disturbance distribution.

$$M_\infty = 1.20, \quad \alpha = 16.9^\circ, \quad r = 153.2 \text{ mm}$$

$$\varphi = 0^\circ, 90^\circ, 180^\circ$$

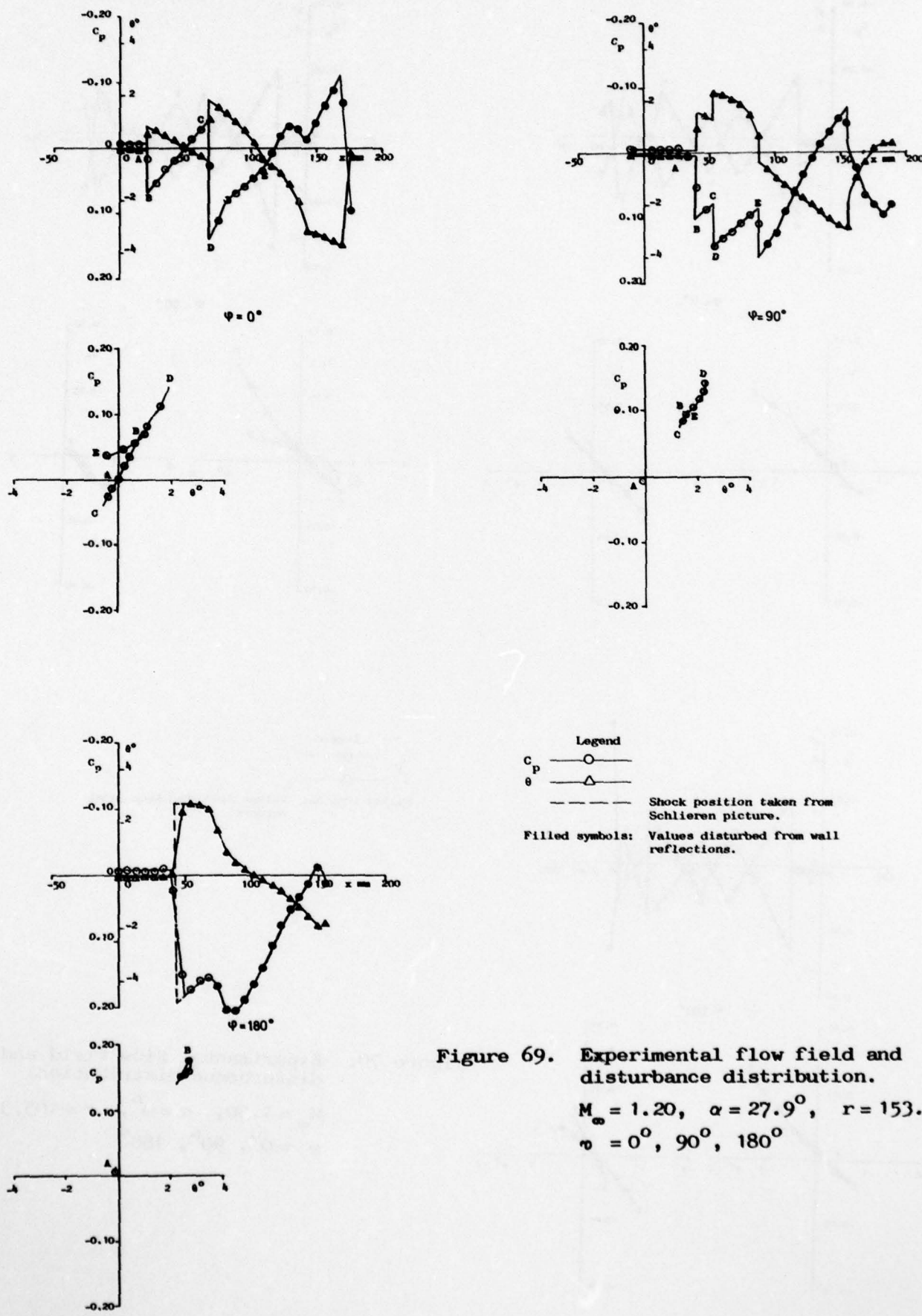
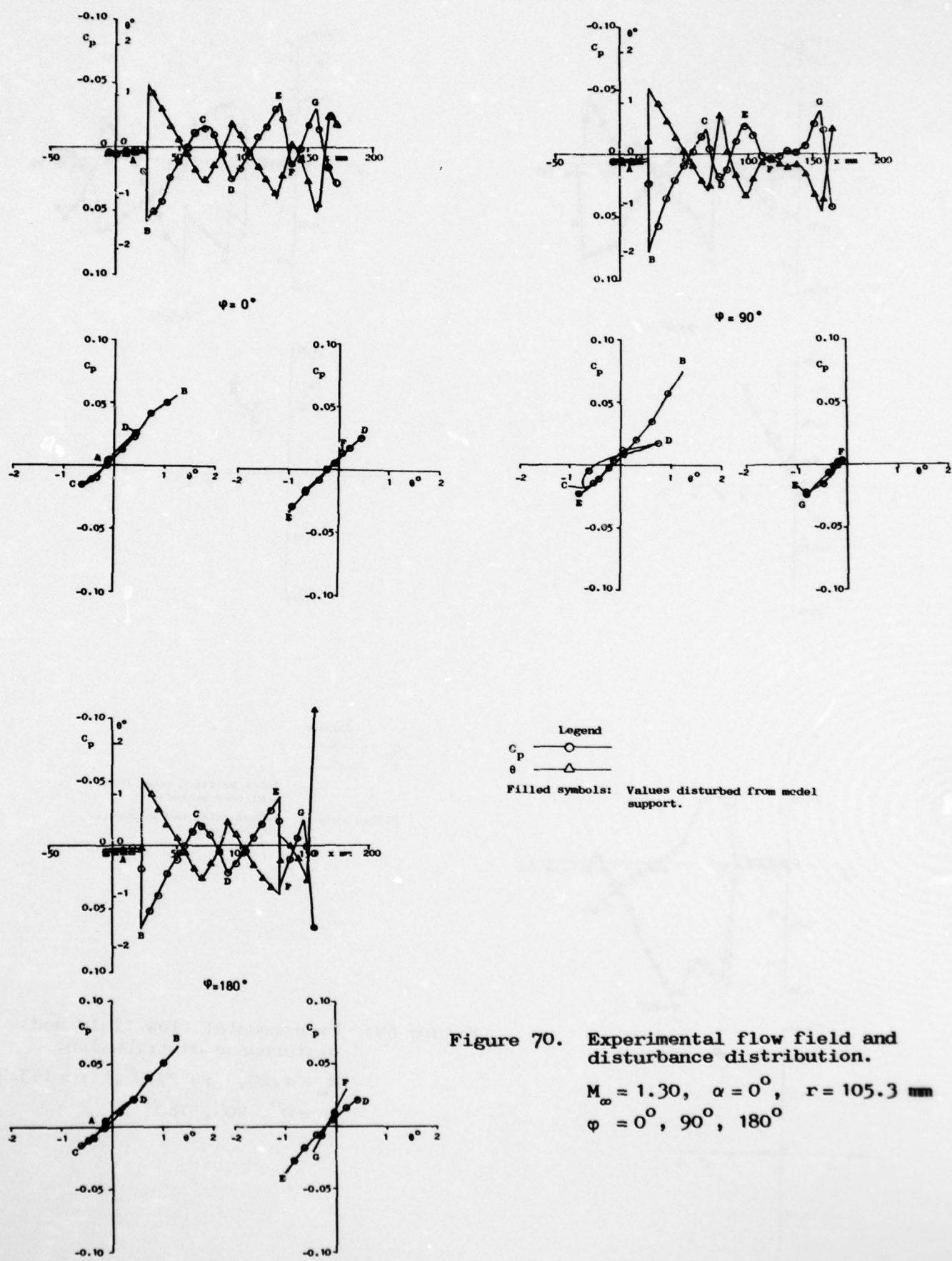


Figure 69. Experimental flow field and disturbance distribution.



AD-A072 098

AERONAUTICAL RESEARCH INST OF SWEDEN STOCKHOLM
INVESTIGATION OF THE BOUNDARY CONDITION AT A WIND TUNNEL TEST S--ETC(U)
MAY 79 S NYBERG, S G HEDMAN, A RIZZI AFOSR-77-3282

F/G 1/3

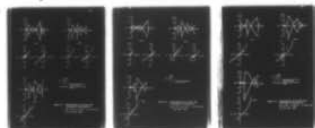
UNCLASSIFIED

AFOSR-TR-79-0868

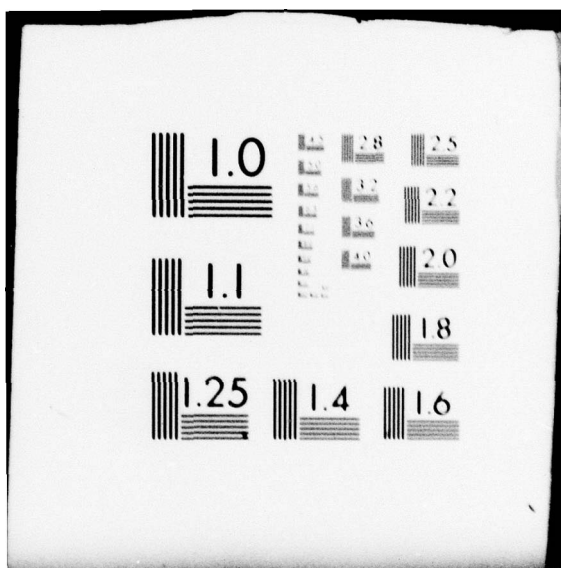
NL

2 OF 2

AD
A072 098



END
DATE
FILED
9-79
DDC



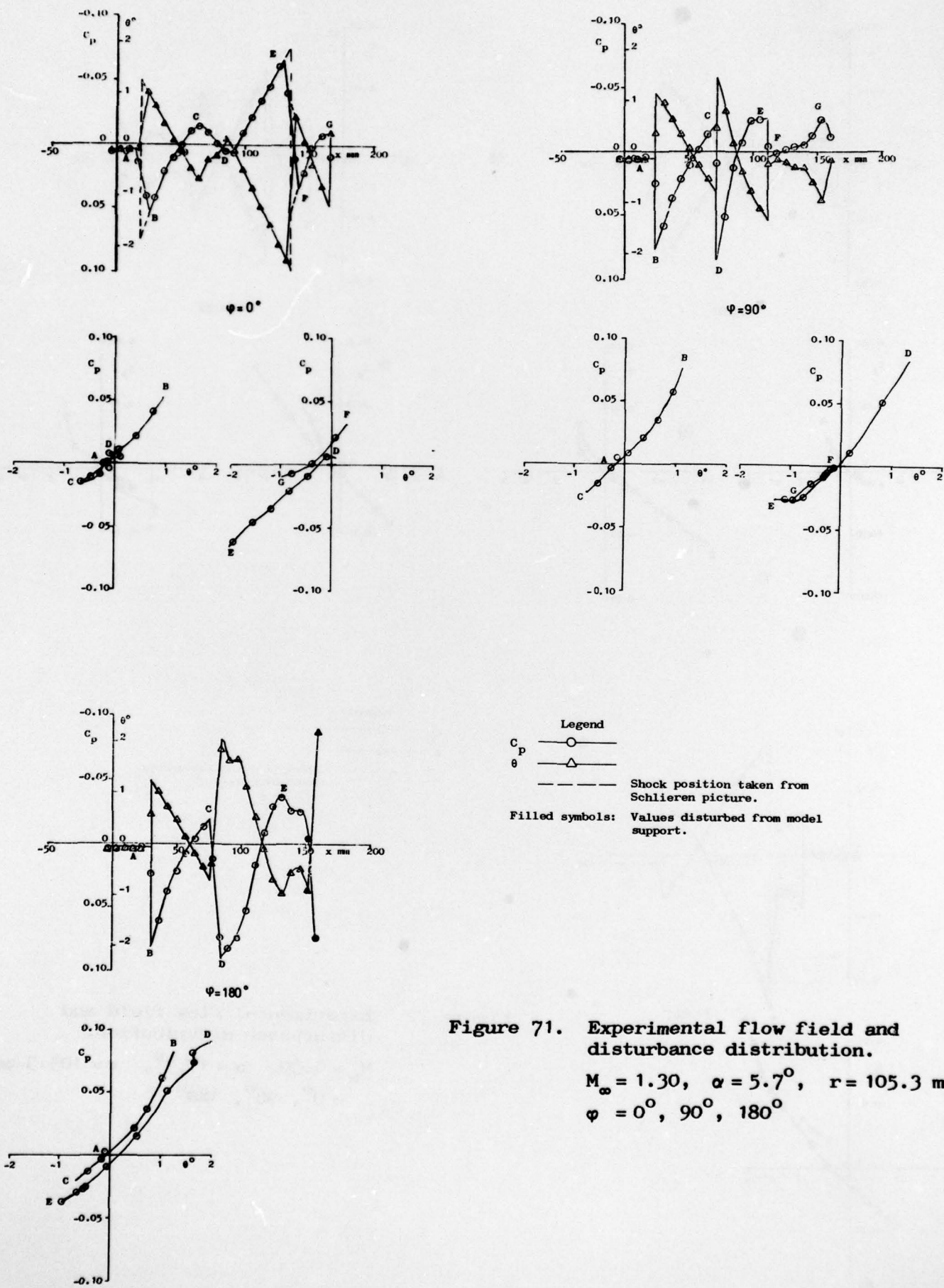


Figure 71. Experimental flow field and disturbance distribution.

$$M_\infty = 1.30, \alpha = 5.7^\circ, r = 105.3 \text{ mm}$$

$$\varphi = 0^\circ, 90^\circ, 180^\circ$$

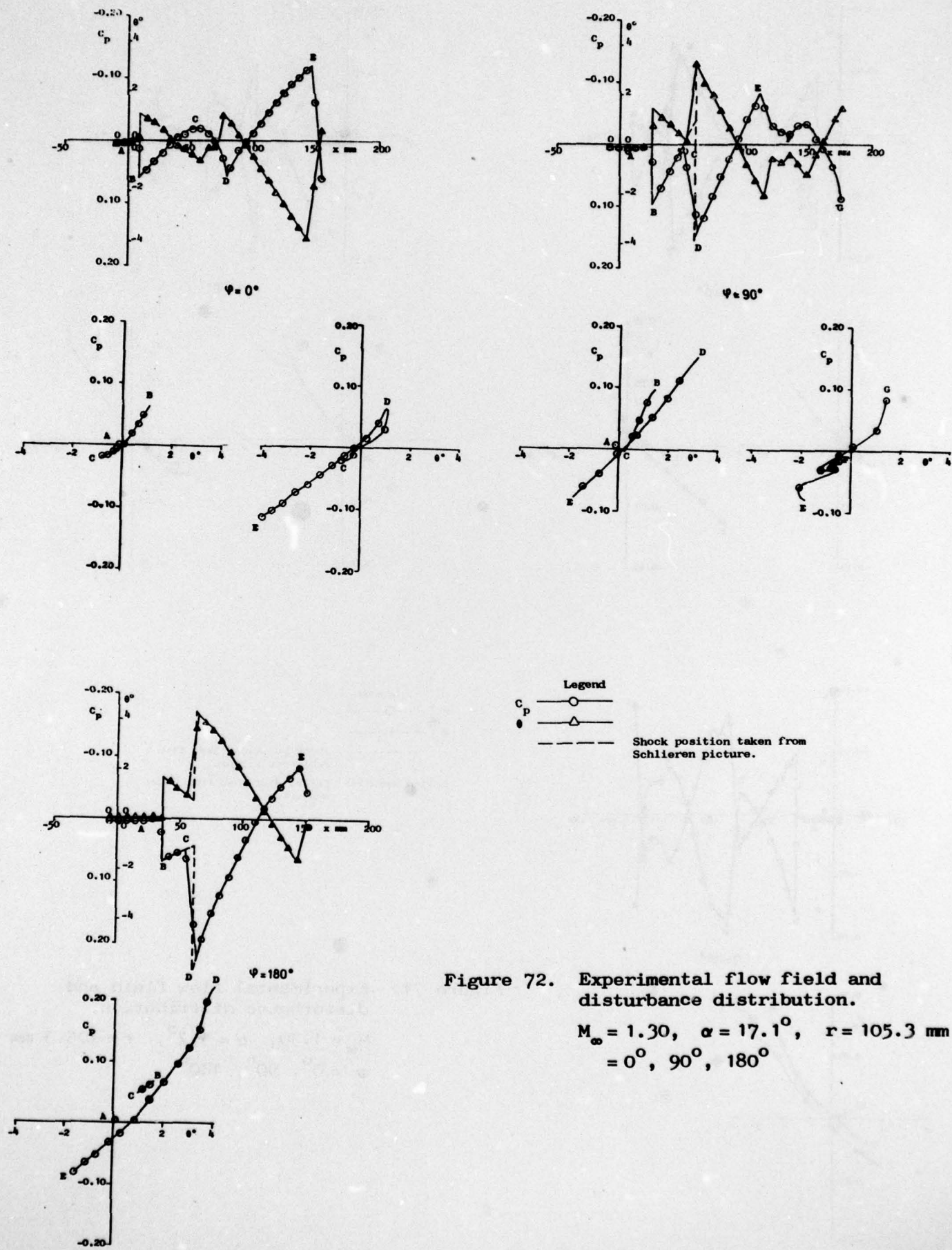


Figure 72. Experimental flow field and disturbance distribution.

$$M_\infty = 1.30, \alpha = 17.1^\circ, r = 105.3 \text{ mm}$$

$$\psi = 0^\circ, 90^\circ, 180^\circ$$

